BOUNDARY LAYER MEASUREMENTS
ON AN
AXISYMMETRIC BODY WITH SPIN AND YAW

Thesis by

H. Carl Thorman

In Partial Fulfillment of the Requirements

For the Degree of

Doctor of Philosophy

California Institute of Technology

Pasadena, California

1958

Dedicated to my wife, Dorothy,

and our children, Carol, Sue, and Tom.

All four of them have endured many hardships

while I indulged in the pursuit of higher learning.

ACKNOWLEDGEMENTS

I wish to express my sincere appreciation to Professors H. J. Stewart, C. B. Millikan, and A. Roshko for the valuable guidance and helpful advice which they have provided throughout the course of this research.

I wish also to acknowledge the contribution made by the late Mrs. Charlotte Willmarth, who performed most of the data reduction and plotted and integrated the many velocity profiles contained in Appendices C and D. Furthermore, I should like to thank all of the many other people who contributed their valuable talents and friendly encouragement. Some of these people were: Dr. George Solomon, who had designed the original model and made preliminary explorations at the time I began this research; the men in Mr. Carroll Bartsch's Aeronautics Machine Shop, each of whom worked on the fabrication of some part of the experimental equipment; Mr. Marvin Jessey, from whom I continuously obtained advice pertaining to the design of the hot-wire electrical circuit and other electrical apparatus; Dr. George Skinner and Professor Lester Lees, whose comments proved to be of great value in the evolution of a satisfactory hot-wire anemometer for these experiments; Dr. William Willmarth, with whom I discussed several troublesome problems on various occasions; Mr. William Bowen and Mr. Ben Williams, who aided in the operation and use of the Merrill Wind Tunnel; Mr. Eben Lapworth and Mr. Peter Brakely, who assisted in the observation and recording of data during the running of the wind-tunnel tests; Mrs. Katherine McColgan and her assistants in the Aeronautics Library, who were very helpful in procuring reference literature; Mrs. Elizabeth Fox, who typed this manuscript and also provided many other secretarial services; Mrs. Alrae Tingley, who typed in all of the equations and drafted the majority of the figures in the text of this paper; Mrs. Betty Wood, who also drafted a significant share of the figures as well as a number of unpublished figures in connection with earlier phases of this research; Mr. Milton Wood, who furnished the photographs; Mrs. Jewel Colbert, who carefully reproduced and assembled the print copies of this report; and the many GALCIT "computresses", who worked on the computations and graphs at various times and also assisted Mrs. Colbert.

Finally, I want to express my gratitude for the financial assistance provided by a Daniel and Florence Guggenheim Jet Propulsion Fellowship during my first year of graduate study, and for the financial support of this research provided by U. S. Army Ordnance (under Contract No. DA-04-495-Ord-481) and by the California Institute of Technology.

ABSTRACT

A directionally-sensitive hot-wire anemometer was developed for measuring the three-dimensional boundary-layer flow on a spinning, axisymmetric body in a low-speed wind tunnel. Boundary-layer velocity profiles at numerous positions around the body are presented for several spin rates at incidence angles of zero and 3 degrees. Displacement thickness distributions, based on integration of the velocity profiles, are also included.

The asymmetries in the azimuthal distribution of the boundary layer around the spinning body at a small angle of incidence (3°) are examined by means of a Fourier analysis of the experimental data. The experimental results are compared with the results of certain theoretical analyses (BRL 870 (Revised), NAVORD 5036) which provide a method for determining Magnus force (and also normal force) due to the displacement effect of the boundary layer.

TABLE OF CONTENTS

TABLE OF CONTENTS (Cont'd)

LIST OF FIGURES

LIST OF TABLES

SYMBOLS

A_n, B_n, C_n, D_n, ($n = 0, 1, 2, \ldots$) coefficients in Fourier Series (see Part IV, eqns. 22, 23)

C_N normal force coefficient

C_p pressure coefficient

C_Y Magnus force coefficient

F_N' normal force per unit length

F_Y' Magnus force per unit length

$f_0, f_1, \ldots f_7$
$g_0, g_1, \ldots g_5$
h_0, h_1, h_2, h_3
velocity profile functions (derivatives with respect to η are indicated by prime marks, e.g. $f_0' = df_0/d\eta$)

I, J integrals related to changes of axial and transverse velocity profiles, respectively, due to spin (defined in Part IV, eqns. 16, 17)

I_w electrical current through hot wire

k number of equal increments of θ used in evaluation of Fourier coefficients (see Part IV, eqns. 24)

L overall length of model

ℓ axial distance from nose of model to measuring station

ℓ_n length of nose section

p pressure

p_∞ pressure far from the body

R free stream Reynolds number based on r_0 (see list of dimensionless quantities below)

R_w, R_1, R_2 hot wire resistances (see Appendix A, fig. A-2)

r radial coordinate

r_0 radius of cylindrical portion of model

T_a tunnel air temperature (absolute)

T_w temperature of hot wire (absolute)

U free stream air speed

u, v, w boundary-layer velocity components corresponding to coordinates x, y, θ, respectively

u_e, v_e, w_e velocity components at outer edge of boundary layer

x longitudinal coordinate

y coordinate normal to surface of body (= $r - r_0$, for circular cylinder)

y_e value of y beyond which $u = u_e$ and $w = w_e$

Greek Letters:

α angle of incidence (attack or yaw)

Δ an increment

Δ* three-dimensional displacement thickness (see Part IV, eqn. 11)

δ_1^* displacement parameter associated with axial velocity profile (defined in Part IV, eqn. 12)

δ_3^* displacement parameter associated with transverse velocity profile (defined in Part IV, eqn. 13)

η similarity parameter (see list of dimensionless quantities below)

θ azimuthal coordinate

ν kinematic viscosity

ρ air density

σ spin rate, ratio of peripheral speed to free stream air speed (see list of dimensionless quantities below)

Φ potential function

φ (or ϕ) perturbation potential

ω rotational speed of model

Other symbols are defined where used in text.

Dimensionless Quantities:

Independent Variables:

$\bar{x} = x/r_0$

$\bar{y} = y/r_0$

$\theta =$ (Radians)

Parameters:

$\alpha =$ (Radians)

$\sigma = \omega r_0/U$

$R = Ur_0/\nu$

$\eta = y\sqrt{U/\nu x} = \bar{y}\sqrt{R/\bar{x}}$

Dependent Variables:

$\bar{u} = u/U$

$\bar{v} = v/U$

$\bar{w} = w/U$

$\bar{p} = p/\rho U^2$

$\bar{\delta}_1^* = \delta_1^*/r_0$

$\bar{\delta}_3^* = \delta_3^*/r_0$

I. INTRODUCTION

1. General

During the past decade several theoretical analyses of problems involving three-dimensional boundary-layer flows have appeared in the literature. Available experimental information, however, is meager, particularly for the case of rotating bodies.

This paper presents the results of an experimental study of some of the intricacies of the steady, incompressible, laminar, three-dimensional boundary-layer flow on a slender body when the body is spinning about its axis of symmetry and the axis is slightly inclined with respect to the direction of a uniform external flow. The limiting case of the non-spinning body at zero incidence, the axially symmetric case of the spinning body at zero incidence, and the case of the non-spinning, slightly inclined body were also included in the study.

For these experiments an accurate and reliable hot wire anemometer was perfected to provide measurements of both direction and speed of the flow in the three-dimensional boundary layer on the cylindrical portion of the spinning body.

2. Review of Literature

Theoretical analyses of boundary layers in which the departure from two-dimensional flow is small may be found in references 1 through 9.* In these analyses small perturbation procedures are used to obtain approximate solutions of the laminar boundary-layer equations.

----

*For a review of three-dimensional boundary-layer literature through 1952, covering various methods of analysis, see references 1(a) or (b).

For incompressible flow, Mager's analysis (ref. 1) covers a fairly wide class of external pressure gradients and body shapes, but it is limited to linear perturbations. Hence, for the inclined, slowly spinning body of revolution, Mager's analysis yields solutions having terms involving angle of attack and spin rate separately but no terms involving the product of these two quantities. For the case of a circular cylinder in incompressible flow with no axial pressure gradient, second order perturbations have been used by Martin (ref. 2) to obtain boundary-layer solutions which include interaction of angle of attack and spin rate. Using the boundary-layer solutions to determine the boundary condition on the potential flow adjacent to the boundary layer he has computed, by means of slender body potential flow theory, the Magnus effect* due to asymmetry of the boundary-layer displacement thickness on the spinning cylinder at small angle of attack. For the same case Kelly (ref. 3) has retained transverse curvature terms in the boundary-layer equations in order to make the analysis applicable to somewhat thicker boundary layers. He has also extended the computation of Magnus effect to include the contribution of the radial pressure gradient through the boundary layer, due to transverse curvature, and the contribution of skin friction, in addition to the displacement thickness effect.

----

*The expression "Magnus effect," in this case refers to a force and moment perpendicular to the axis of the body and lying in a plane perpendicular to the plane in which the angle of attack lies, i.e. a "side force" and a "yawing moment." The dispersion of some types of spinning projectiles is strongly influenced by this effect. Discussions of the contrast between the Magnus effect at small angle of attack and the classical "Magnus force" on a spinning cylinder in cross flow may be found in references 2, 3, 10 and 11.

In order to study non-linear effects of spin, Kelly and Thacker (ref. 4) have considered additional perturbations to obtain solutions which include products of angle of attack, to the first power, times spin rate up to the third power.

Gerber (ref. 5) has indicated that he and Martin have extended the solution for the zero spin case to include third-power terms in angle of attack.

To facilitate interpretation of the data in the present paper the experimental results are compared with theoretical results based on numerical values obtained from references 2, 4, and 5.

II. EQUIPMENT

1. Model and Installation

The model used in this study (fig. 1) was a right circular cylinder with a nose section consisting of half of an ellipsoid. The overall length of the model was 24 inches. The nose section was 7.2 inches long to the point of tangency and was constructed of hardwood. The cylindrical section was 2.4 inches in diameter and consisted of a lucite shell fitted over an aluminum inner body. The surface of the model was finished with several coats of lacquer.

The model was installed in the GALCIT* Merrill Wind Tunnel as shown in figure 2(a). Ball bearings within the aluminum inner body supported the model on a 1 inch diameter hollow sting, through which ran a flexible drive shaft for spinning the model. The truss to which the sting was attached was designed to permit the sting to be pivoted about the forward vertical post of the truss in order to vary the angle of yaw of the model. A machine-divided protractor was provided to measure yaw angle.

A 24 volt, shunt type, d. c. motor was connected through a Metron speed reducer to the flexible drive shaft for spinning the model. Accurate measurement of rotational speed was accomplished by use of a magnetic pickup (Electro Products Model 3010-A) which was excited by a toothed wheel mounted on the motor shaft. Impulses generated by the magnetic pickup were monitored on a Hewlett-Packard Model 522B electronic counter (fig. 2(b)).

----

*Guggenheim Aeronautical Laboratory, California Institute of Technology.

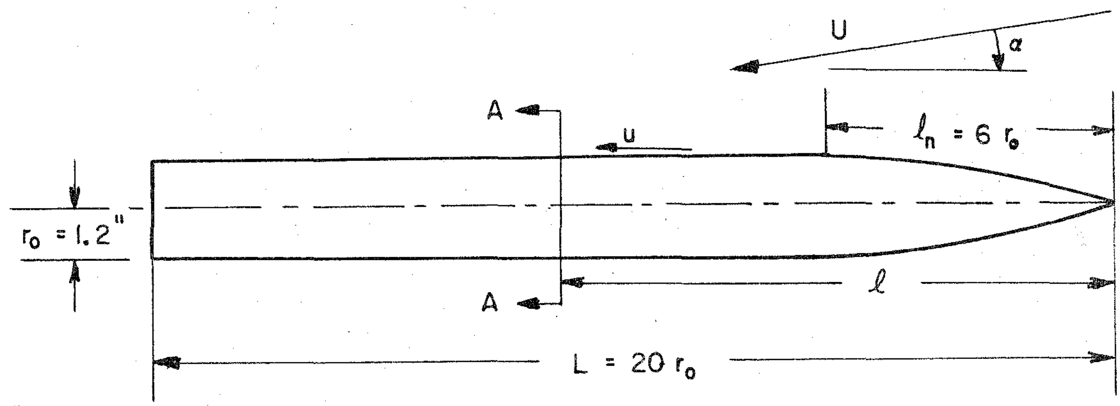

Plan View of Model as Installed in Wind Tunnel

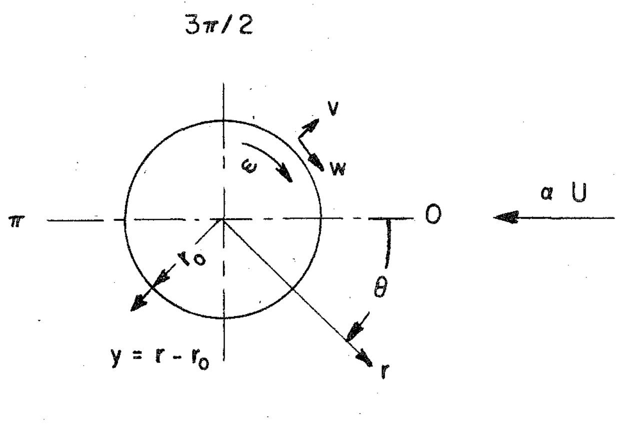

A-A

Front Cross Section View of Model as Installed in Wind Tunnel Showing Coordinate System

FIGURE 1
NOMENCLATURE AND MODEL DIMENSIONS

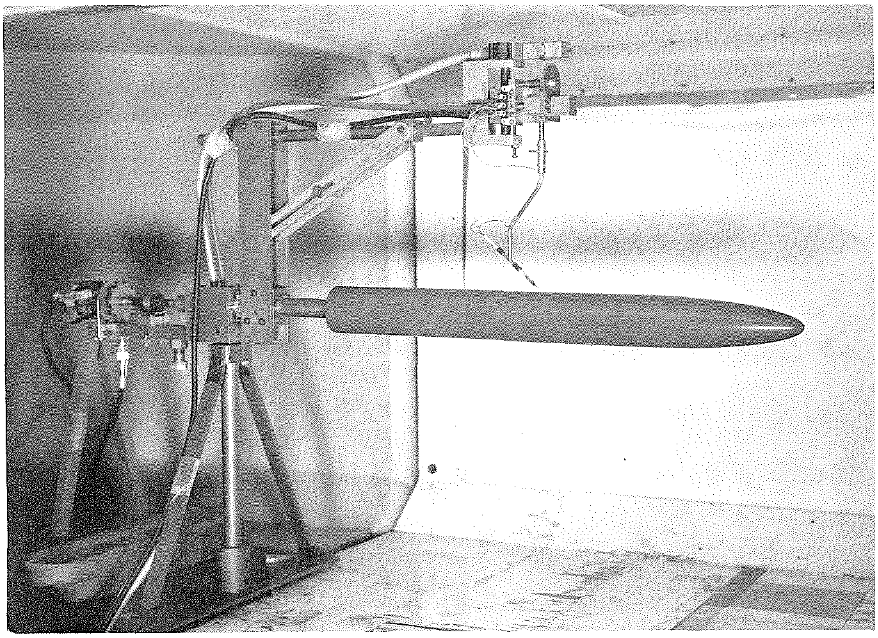

FIGURE 2(a)
MODEL INSTALLED IN MERRILL WIND TUNNEL

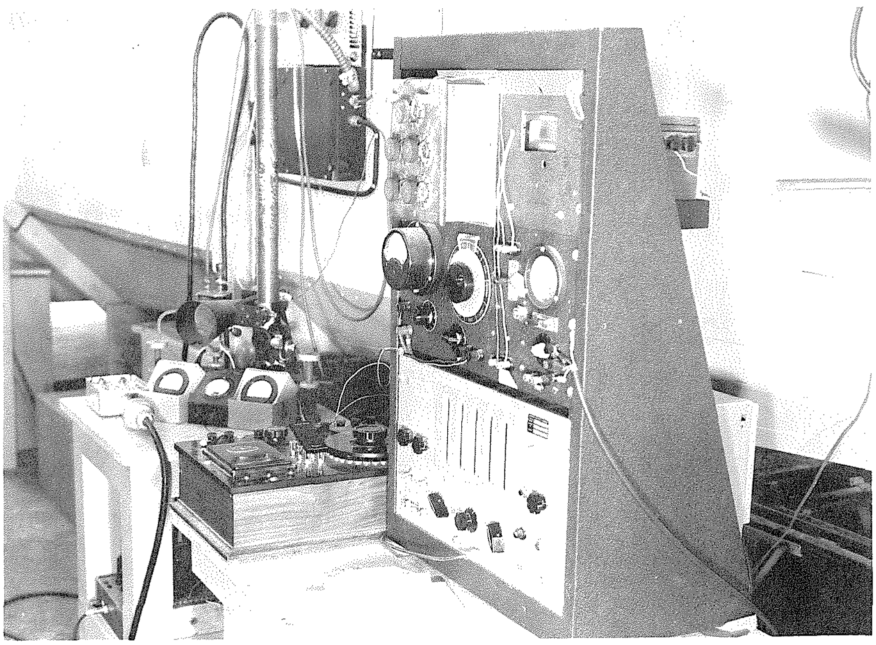

FIGURE 2(b)
INSTRUMENTS AND CONTROLS FOR OPERATION OF HOT WIRE, MODEL, AND TUNNEL

2. Hot Wire Anemometer

The directionally sensitive hot wire anemometer developed for these experiments employed a V-shaped hot wire on a pivoting probe, together with a dual Wheatstone bridge, to incorporate null seeking methods into the operating technique. The electrical circuitry and the operating procedures are explained in Appendix A.

The dimensions of the V-shaped hot wire sensing element, which was made of one-half mil diameter platinum-10% rhodium wire, are given in the following sketch:

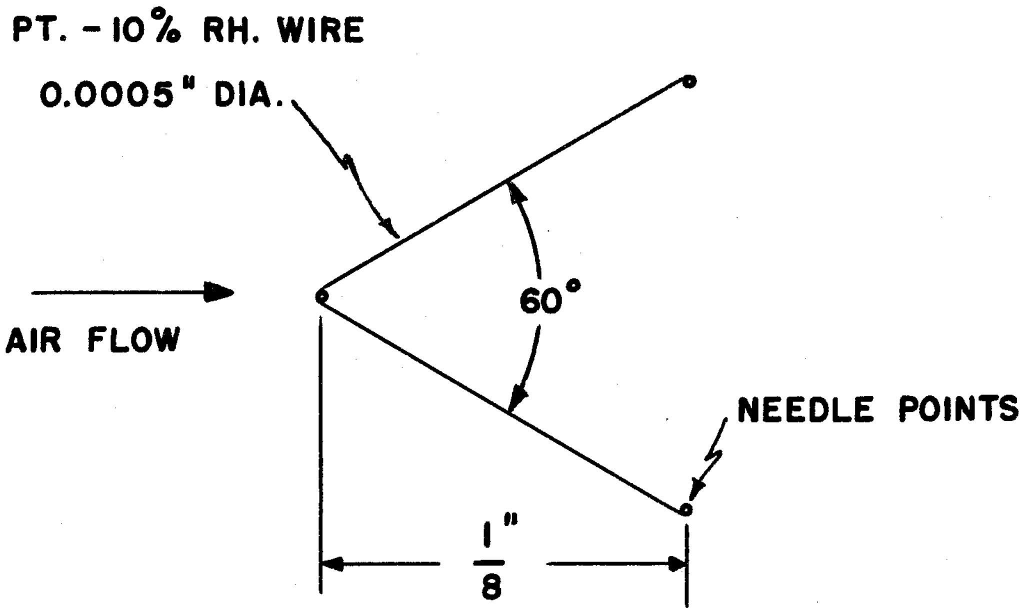

Sketch of V-shaped Hot Wire

The wire was soldered to the tips of three sewing needles at the end of the probe. The plane described by the V was parallel to a plane tangent to the model surface. The axis about which the hot wire was pivoted was approximately through the center of the triangle formed by the three needle points.

The hot wire probe was supported by a holder which was mounted on a probe actuator, or "yaw head," as shown in figure 2(a). The actuator was equipped with a lead screw to provide radial traversing motion and a worm and pinion drive to pivot the probe holder. The radial distance of the hot wire from the model surface and the angular position of the probe were indicated by Veeder counters attached to the actuator. The actuator was supported from the model sting so that the assembly could be rotated to various azimuthal positions around the model. Azimuth was determined by means of a protractor mounted on the sting support and a pointer on the actuator support.

Because of the obstruction presented by the vertical post on the sting support, the probe actuator could not be placed directly under the model ($\theta = \pi/2$), so measurements corresponding to $\theta = \pi/2$ were obtained at the top of the model ($\theta = 3\pi/2$) by spinning the model in the negative direction.

Measurements of flow direction and total pressure in the boundary layer could have been obtained by mounting a small, "claw-type" total head probe on the probe actuator in place of the hot wire probe. To determine flow speed, however, measurements of local static pressures would also be required since the azimuthal pressure distribution is non-uniform when the body is yawed and, furthermore, a radial pressure gradient is produced by spinning of the body.

By using a hot wire for the present boundary-layer velocity measurements the formidable problem of measuring the static pressure distribution on a yawed, rotating body was avoided.*

A set of boundary-layer velocity measurements for the basic case of the non-spinning model at zero yaw was obtained with a simple total head tube mounted on the probe actuator and a small static pressure probe taped to the opposite side of the model as shown in figure 3. These measurements were used to check the hot wire measurements obtained for the same case.

In the original design the hot wire probe was installed perpendicular to the model surface (fig. 4). Due to the excessive interference errors encountered as the probe approached the surface, the measurements obtained with the perpendicular probe were invalid and had to be discarded. The probe interference effects are discussed further in Part III. To minimize such errors a swept back probe configuration (fig. 5) was devised. In this configuration the probe and needles were at an angle of 30° with respect to the model, while the plane of the hot wire was kept parallel to the model.

----

*An investigation of methods for measuring pressures on the surface of a rotating model was conducted by Larsen (ref. 12). His paper includes a description of the construction and preliminary testing of a model which he designed for obtaining such measurements by a pulse sampling technique.

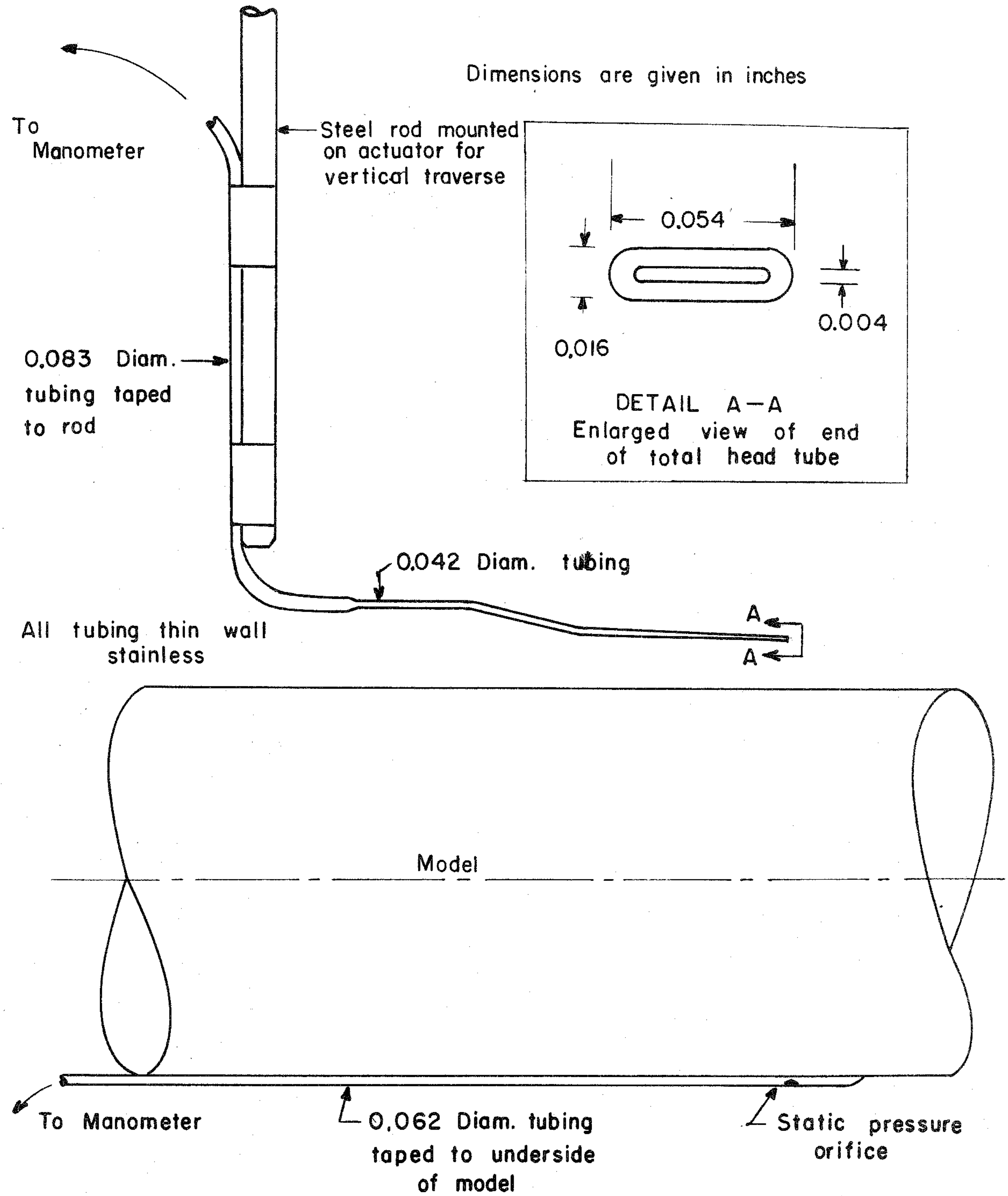

FIGURE 3

SKETCH OF TOTAL AND STATIC PRESSURE INSTRUMENTATION

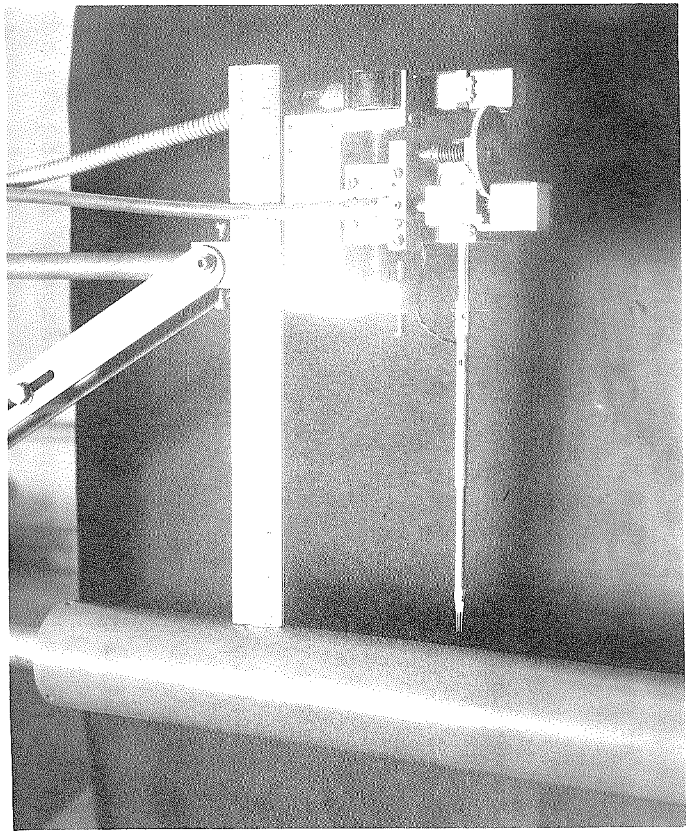

FIGURE 4
PERPENDICULAR PROBE

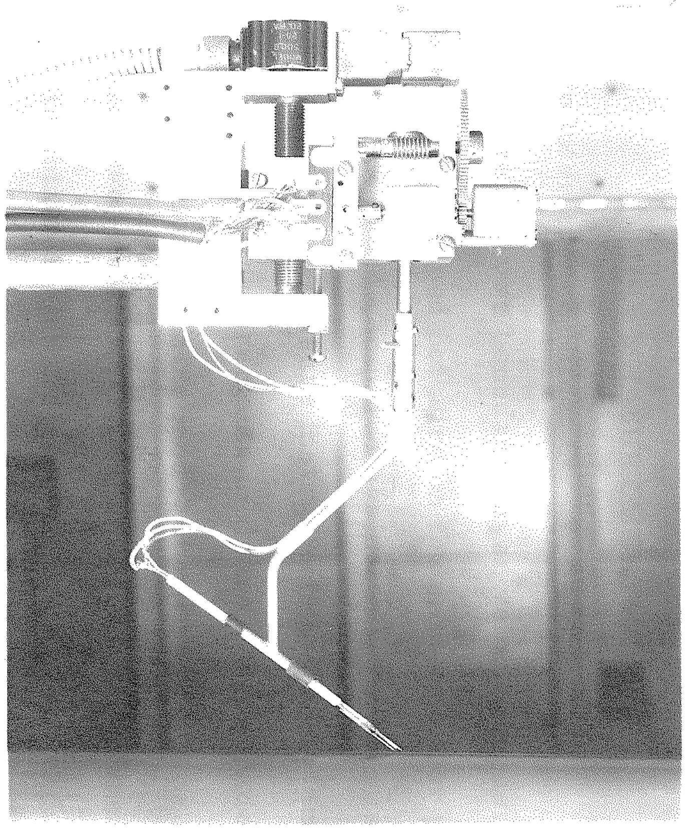

FIGURE 5
SWEPT BACK PROBE

III. MEASUREMENTS

1. Probe Interference Effect

Figure 6 shows boundary-layer velocity measurements obtained with a V-shaped hot wire on the perpendicular probe and on the swept back probe compared against measurements obtained with the total and static pressure instrumentation described in Part II. All three sets of measurements in figure 6 were made at the same position on the non-spinning model at zero yaw. For the spinning model and yawed-model cases examples of the difference between the results obtained with the perpendicular probe and the results obtained with the swept-back probe are given in Appendix B.

In figure 6 it is evident that the perpendicular probe measurements were appreciably in error while the swept-back probe measurements were in good agreement with the pressure measurements. It will be shown in Part V that the swept-back probe measurements for this case ($\alpha = 0$, $\sigma = 0$) were also in good agreement with theoretical predictions.

All of the hot wire measurements to be discussed in the remainder of this report were obtained by using the swept-back probe.

2. Presentation of Data

The measured velocities have been resolved into axial and transverse components (u and w, respectively) and compiled in non-dimensional plots which are presented in Appendices C and D. The fairings of the velocity profiles shown in these plots were used for the graphical integration required in the analysis described in Part IV.

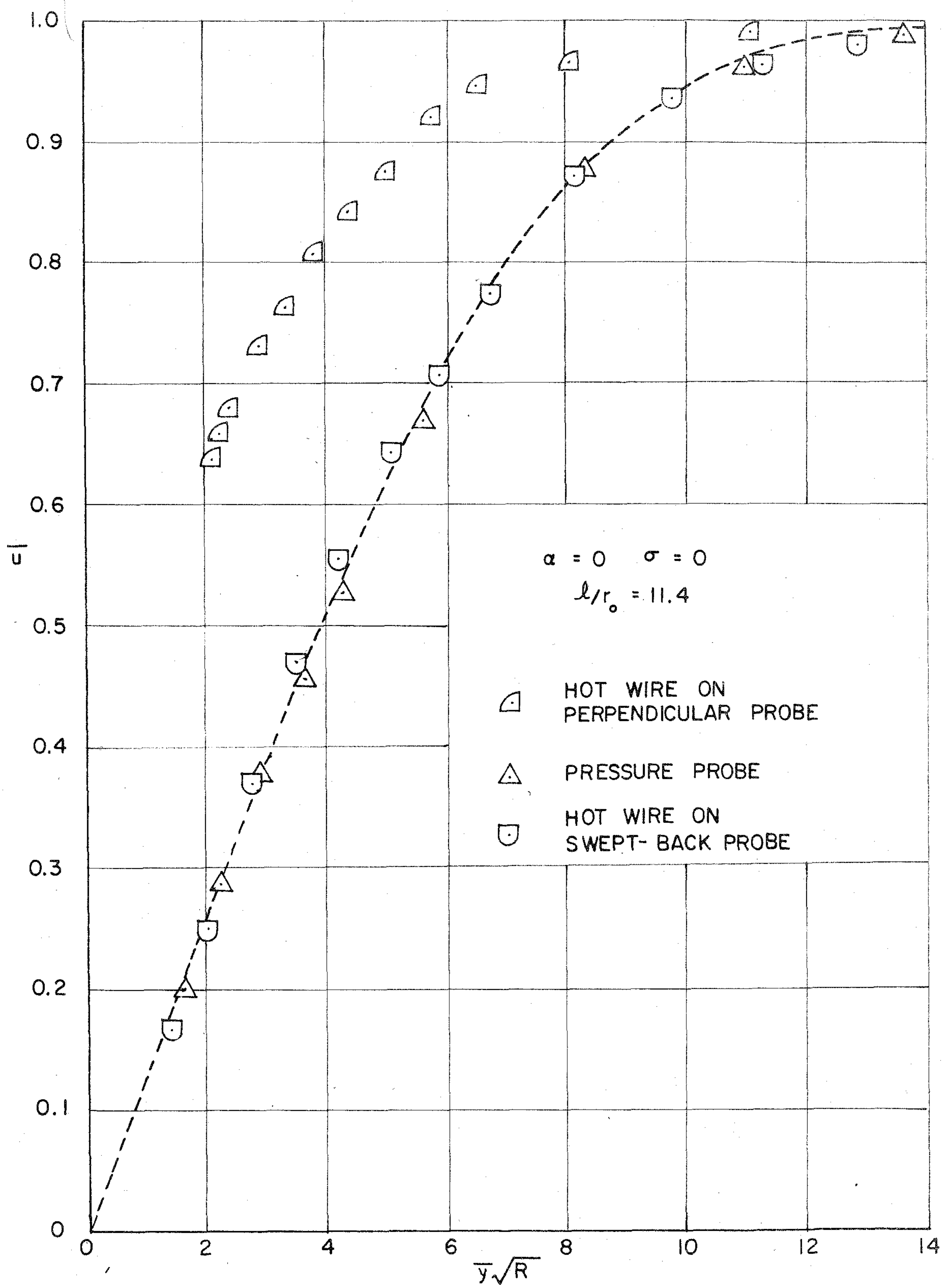

FIGURE 6

INTERFERENCE ERROR EXHIBITED BY PERPENDICULAR PROBE

3. Range of Measurements

Boundary-layer velocity profiles were obtained for 73 different combinations of the various independent variables and parameters, as shown in table I. During the course of the experiment 11 of the profiles were repeated to confirm the reliability of the measurements. A chronological schedule of runs, showing the conditions for each run, appears in Appendix E.

4. Boundary-Layer Transition Due to Spin

For all spin rates from $\sigma = 0$ to $\sigma = \pm 0.44$ the experimental velocity profiles shown in Appendices C and D appear to be of the laminar type. The profiles for $\sigma = \pm 0.6$, on the other hand, have a shape which bears a strong resemblance to the type of profile usually observed in a turbulent boundary layer. The dependence of transition on spin rate was verified by placing a 0.0002 inch (two-tenths mil) diameter straight hot wire in the boundary layer, at $\theta = 3\pi/2$, and observing the fluctuations in the signal displayed on an oscilloscope at various spin rates. Observations were made at two values of tunnel air speed, with both positive and negative spin, for the following cases:

$$\alpha = 0^{\circ}, \qquad \ell/r_0 = 10.2$$
$$\alpha = 0^{\circ}, \qquad \ell/r_0 = 11.4$$
$$\alpha = 3^{\circ}, \qquad \ell/r_0 = 11.4$$

At a tunnel speed of 15 ft./sec. (R = 9,000 based on body radius) small fluctuations began to appear at a model rotational speed of about 7 rev./sec. (dimensionless spin rate $\sigma = 0.3$). As the spin rate increased the fluctuations became larger and more

TABLE I

TEST CONDITIONS FOR MEASUREMENTS WITH HOT WIRE ON SWEPT-BACK PROBE

Yaw Angle α	Axial Station ℓ/r_o	Approximate Reynolds No. Ur_o/ν	Azimuth θ	Nominal Spin Rate σ
0	11.4	9,000	$\pi/2$*	* 0.4, 0.6
0	11.4	9,000	$3\pi/2$	0, 0.1, 0.2, 0.4, 0.6
0	11.4	18,000	0	0, 0.2
0	11.4	18,000	$\pi/2$*	* 0.2
0	11.4	18,000	π	0, 0.2
0	11.4	18,000	$3\pi/2$	0, 0.05, 0.1, 0.2, 0.3
0	11.4	33,000	$3\pi/2$	0
0	10.2	9,000	$\pi/2$*	* 0.2
0	10.2	9,000	$3\pi/2$	0, 0.2, 0.6
3^o	11.4	9,000	0	0, 0.1, 0.2, 0.4
3^o	11.4	9,000	$\pi/4$	0, 0.1, 0.2, 0.4
3^o	11.4	9,000	$\pi/2$*	* 0.1, 0.2, 0.4, 0.6
3^o	11.4	9,000	$3\pi/4$	0, 0.1, 0.2, 0.4
3^o	11.4	9,000	π	0, 0.1, 0.2, 0.4
3^o	11.4	9,000	$5\pi/4$	0, 0.1, 0.2, 0.4
3^o	11.4	9,000	$3\pi/2$	0, 0.1, 0.2, 0.4, 0.6
3^o	11.4	9,000	$7\pi/4$	0, 0.1, 0.2, 0.4
3^o	11.4	19,000	0	0, 0.05, 0.1, 0.2, 0.3
3^o	11.4	19,000	$\pi/2$*	* 0.05
3^o	11.4	19,000	π	0, 0.05, 0.1, 0.2, 0.3
3^o	11.4	19,000	$3\pi/2$	0, 0.05
3^o	10.2	9,000	$\pi/2$*	* 0.2, 0.6
3^o	10.2	9,000	$3\pi/2$	0, 0.2, 0.6

*Measurements corresponding to $\theta = \pi/2$ were obtained at $\theta = 3\pi/2$ by using negative spin.

frequent. Fully developed turbulence, evidenced by completely chaotic fluctuations, was established at about 13 rev./sec. ($\sigma = 0.5$) and remained at all higher spin rates with this tunnel speed. At a tunnel speed of 30 ft./sec. ($R \doteq 18,000$) small fluctuations began to appear at about 10 rev./sec. ($\sigma \doteq 0.2$) and increased with spin up to the maximum model rotational speed of 18 rev./sec. ($\sigma \doteq 0.35$), but fully developed turbulence had not yet become established. Any effects which might have been present due to the aforementioned variations in angle of yaw (α), axial position (ℓ / r_0), or direction of spin, were too small to be readily distinguishable. At the lower tunnel speed, however, there was some evidence that turbulence at the rearward axial position might have become established at a slightly lower spin rate.

The present results agree with those of an earlier investigation of transition on this model, in which Fehrman (ref. 13) found that for rotational speeds below 10 rev./sec. the boundary layer was laminar at all tunnel speeds up to 150 ft./sec.($R \doteq 90,000$ based on body radius). * In connection with these observations it should be pointed out that increasing the air speed decreases the boundary-layer thickness.

The observations described in the foregoing paragraphs suggest that the three-dimensional transition phenomenon associated with spinning of this model may be related to the well known

----

*For this reason it was necessary for Fehrman to use a tripping device to obtain the transition measurements reported in reference 13.

"Taylor instability" (refs. 14, 15) which occurs in the motion of a fluid contained between two concentric cylinders with the inner cylinder totating.

5. External Velocity Gradient

Exploratory measurements of axial velocity outside the boundary layer, on the non-spinning model at zero yaw, were made by traversing a hot wire in the longitudinal direction along the lower side of the model. These measurements indicated no appreciable axial velocity gradient in the neighborhood of the stations at which the boundary-layer measurements were obtained. No measurements were made of the external velocity gradient along the model with spin or yaw, however.

IV. METHODS OF ANALYSIS

Some of the results of the theoretical analyses mentioned in Part I will be interpreted here in terms of quantities which are appropriate for comparison with the present measurements. Methods for computing such quantities from the experimental data will be derived along with methods for computing the corresponding theoretical values from numerical results given in references 2 and 4.

1. Velocity Profiles

The theoretical model used in references 2 and 4 is an open-ended circular cylinder spinning about its axis, which is inclined at a small angle with respect to the direction of the external flow stream. Steady flow of incompressible fluid is assumed, with uniform velocity U far from the body. In the present review we shall consider only the case in which the boundary-layer thickness is small compared to the radius of the cylinder. In this case the equations of motion for a laminar boundary layer on the cylinder may be reduced, by retaining only terms of the highest order of magnitude, to the following:

Continuity,

$$\frac{\partial \bar{u}}{\partial \bar{x}} + \frac{\partial \bar{v}}{\partial \bar{y}} + \frac{\partial \bar{w}}{\partial \theta} = 0 \tag{1}$$

Axial Momentum,

$$\bar{u}\frac{\partial \bar{u}}{\partial \bar{x}} + \bar{v}\frac{\partial \bar{u}}{\partial \bar{y}} + \bar{w}\frac{\partial \bar{u}}{\partial \theta} = \frac{1}{R}\frac{\partial^2 \bar{u}}{\partial \bar{y}^2} \tag{2}$$

Radial Momentum,

$$\bar{w}^2 = \frac{\partial \bar{p}}{\partial \bar{y}} \tag{3}$$

Azimuthal Momentum,

$$\bar{u}\frac{\partial \bar{w}}{\partial \bar{x}} + \bar{v}\frac{\partial \bar{w}}{\partial \bar{y}} + \bar{w}\frac{\partial \bar{w}}{\partial \Theta} = 4\alpha^2 \sin\Theta\cos\Theta + \frac{1}{R}\frac{\partial^2 \bar{w}}{\partial \bar{y}^2} \tag{4}$$

In these equations the variables and parameters have been written in non-dimensional form by referring all lengths to the body radius and referring all velocities to the free stream speed. The coordinates are measured in an orthogonal system which has been used by several authors (e.g. Howarth, Illingworth, Mager) in the analysis of thin boundary layers on bodies of revolution. In this system $\bar{y}$ is measured from and normal to the surface, and thus, in general, the longitudinal coordinate is measured along the surface. For the present case of constant body radius, however, the system is equivalent to a cylindrical coordinate system except that the radial coordinate is measured from the surface.

Mager (ref. 1) and Kelly (refs. 3, 4) have shown that a radial pressure gradient will exist as indicated by equation 3. It can be shown, however, that the effect of the radial pressure gradient upon the pressure gradients in the other two directions is negligible, to the order of approximation involved here. In equation 2, therefore, the pressure gradient term does not appear. In equation 4 the pressure gradient term (4th term) has been evaluated by slender body theory for potential flow over a non-spinning circular cylinder at a small angle of incidence.

The boundary conditions, based on slender body potential flow theory, are assumed to be:

$$\bar{u} = \bar{v} = 0, \quad \text{and} \quad \bar{w} = \sigma, \text{ at } \bar{y} = 0$$

$$\bar{u} = 1 - \frac{\alpha^2}{2}, \text{ and } \bar{w} = 2\alpha \sin\theta, \text{ at } \bar{y} \to \infty$$

In the various references previously mentioned, solutions for the boundary-layer velocity components $\bar{u}$, $\bar{v}$ and $\bar{w}$ are obtained by use of a similarity transformation together with the application of a perturbation procedure. For the thin boundary-layer case the similarity parameter may be written as $\eta = \bar{y}\sqrt{R/\bar{x}}$ in the present nomenclature. The perturbation process is based on the assumption that the velocity components may be expanded in powers of α and σ about $\alpha = \sigma = 0$.

Solutions obtained by Martin (ref. 2), which will be denoted by subscript M, are as follows:

$$\begin{aligned} \bar{u}_M = {} & f_0'(\eta) + \alpha[2\bar{x}f_1(\eta)\cos\theta] + \alpha\sigma[\bar{x}^2 f_2(\eta)\ \sin\theta] \\ & + \alpha^2[\bar{x}^2 f_3(\eta) + \bar{x}^2 f_4(\eta)\cos 2\theta] - \frac{\alpha^2}{2} f_5'(\eta) \end{aligned} \qquad (5)$$

$$\begin{aligned} \bar{v}_M = {} & \frac{1}{\sqrt{R\bar{x}}}\Big\{ \tfrac{1}{2}[\eta f_0'(\eta) - f_0(\eta)] + \alpha[\bar{x}g_0(\eta)\cos\theta] + \alpha\sigma[\bar{x}^2 g_1(\eta)\sin\theta \\ & + \alpha^2[\bar{x}^2 g_2(\eta) + \bar{x}^2 g_3(\eta)\cos 2\theta] - \frac{\alpha^2}{4}[\eta f_5'(\eta) - f_5(\eta)]\Big\} \end{aligned} \qquad (6)$$

$$\begin{aligned} \bar{w}_M = {} & \sigma[1 - f_0'(\eta)] + \alpha[2f_0'(\eta)\sin\theta] + \alpha\sigma[\bar{x}h_0(\eta)\cos\theta] \\ & + \alpha^2[\bar{x}h_1(\eta)\sin\theta\cos\theta] \end{aligned} \qquad (7)$$

Numerical solutions of the various profile functions $f_o(\eta)$, $f_o'(\eta)$, $f_1(\eta)$, etc., satisfying the given boundary conditions, are tabulated in reference 2.

For the case of $\alpha = \sigma = 0$, equations 1 through 4 and the boundary conditions are satisfied by the flat plate solution. Thus, $f_o(\eta)$ is the well-known Blasius function.

Kelly and Thacker (ref. 4) have considered higher-order perturbations in spin rate to obtain solutions (denoted by subscript K) which, for the present case, may be represented as extensions of Martin's solutions:

$$\bar{u}_K = \bar{u}_M + \alpha\sigma^2[\bar{x}^3 f_6(\eta)\cos\theta] + \alpha\sigma^3[\bar{x}^4 f_7(\eta)\sin\theta] \tag{8}$$

$$\bar{v}_K = \bar{v}_M + \frac{1}{\sqrt{R\bar{x}}}\{\alpha\sigma^2[\bar{x}^3 g_4(\eta)\cos\theta] + \alpha\sigma^3[\bar{x}^4 g_5(\eta)\sin\theta]\} \tag{9}$$

$$\bar{w}_K = \bar{w}_M + \alpha\sigma^2[\bar{x}^2 h_2(\eta)\sin\theta] + \alpha\sigma^3[\bar{x}^3 h_3(\eta)\cos\theta] \tag{10}$$

Although the profile functions shown here are not identical to the functions given in reference 4, the numerical values can be determined from the tables of reference 4 by relating the similarity parameters as follows:

$$\eta_K = \frac{r^2 - r_0^2}{4r_0}\sqrt{\frac{U}{vx}} = \left(\frac{r + r_0}{4r_0}\right)\eta$$

thus, for the thin boundary layer case ($r \to r_o$),

$$\eta_K \doteq \frac{1}{2}\eta$$

Although the experimental model had a nose section which would influence the boundary-layer growth, it could be expected that the boundary layer far enough back on the cylindrical section might exhibit the similarity predicted by the open cylinder theory, at least for the case of $\alpha = \sigma = 0$. The distance $\bar{x}$ from the origin of similarity to a given station, however, could not be determined by direct experimental methods, independent of theoretical considerations. The experimental boundary-layer velocity profiles, therefore, are presented in terms of $\overline{y}\sqrt{R}$ instead of η.

The method used for determining an empirical value of $\overline{x}$ for use in the theoretical computations is explained in Part V.

2. Displacement Parameters

In references 2 and 4 the displacement thickness of the three-dimensional boundary layer (refs. 16, 17) is defined as the distance from the body surface to a "displacement surface" corresponding to the inviscid flow deflection required to simulate the apparent outflow, or mass-flow defect, due to the boundary layer. For the incompressible, thin boundary layer we may write this relation, in the nomenclature of the present paper, as follows:

$$\frac{\partial}{\partial x}(u_e \Delta^*) + \frac{1}{r_0}\frac{\partial}{\partial \theta}(w_e \Delta^*) = \lim_{y \to y_e} \left(v - y\frac{\partial v}{\partial y}\right) \tag{11}$$

Expressing the right-hand side of equation 11 in terms of u and w (by continuity) gives the expression used in reference 2:

$$\frac{\partial}{\partial x}(u_e \Delta^*) + \frac{1}{r_0}\frac{\partial}{\partial \theta}(w_e \Delta^*) = \frac{\partial}{\partial x}\int_0^{y_e}(u_e - u)\,dy + \frac{1}{r_0}\frac{\partial}{\partial \theta}\int_0^{y_e}(w_e - w)\,dy \tag{11a}$$

where Δ^* represents the displacement thickness. The right-hand side of equation 11 corresponds to the apparent outflow velocity at the surface, from the viewpoint of an observer outside the boundary layer. It should be noted that, for the yawed, circular cylinder in uniform flow, $\partial u_e/\partial x$ is zero but $\partial w_e/\partial \theta$ is not zero.

In the present paper we shall not attempt to compute experimental values of Δ^*. For our comparisons of experimental and theoretical results we shall use the integrals appearing in equation 11a, since these can be computed from the profiles of u and w individually. We shall define each of two characteristic lengths,

δ_1^* and δ_3^*, in a manner analogous to the relationship between the displacement thickness and the velocity profile of a two-dimensional boundary layer:

$$u_e \delta_1^* = \int_0^{y_e} (u_e - u)\,dy \tag{12}$$

$$(w_e - \omega r_0)\delta_3^* = \int_0^{y_e} [(w_e - \omega r_0) - (w - \omega r_0)]\,dy = \int_0^{y_e} (w_e - w)\,dy \tag{13}$$

Velocities relative to the body surface have been used in these definitions so that δ_1^* and δ_3^* will have meaning (and will be positive) for all values of σ and α, including the case of the spinning body at zero angle of incidence. In the terminology of references 2 and 4 the term "displacement thickness" is reserved for the quantity Δ^*. In the present analysis, therefore, we shall refer to δ_1^* and δ_3^* merely as "displacement parameters".

The methods for computing the displacement parameters in dimensionless form are as follows:

$$\overline{\delta_1^*}\sqrt{R} = \frac{\int_0^{\bar{y}_e\sqrt{R}} (\bar{u}_e - \bar{u})\, d\bar{y}\sqrt{R}}{\bar{u}_e} \qquad \text{(experimental)} \tag{14}$$

$$= \sqrt{\bar{x}} \int_0^{\infty} \left(1 - \frac{\bar{u}}{1 - \frac{\alpha^2}{2}}\right) d\eta \qquad \text{(theoretical)} \tag{14a}$$

$$\overline{\delta_3^*}\sqrt{R} = \frac{\int_0^{\bar{y}_e\sqrt{R}} (\bar{w}_e - \bar{w})\ d\bar{y}\sqrt{R}}{(\bar{w}_e - \sigma)} \qquad \text{(experimental)} \quad (15)$$

$$= \sqrt{\bar{x}} \int_0^{\infty} \left(\frac{2\alpha \sin\theta - \bar{w}}{2\alpha \sin\theta - \sigma} \right) d\eta \qquad \text{(theoretical)} \quad (15a)$$

The experimental values presented in Part V are based on graphical integration of the measured velocity profiles. For the computation of the corresponding theoretical values the appropriate numerical values of the integrated profile functions were obtained from references 2 and 4.

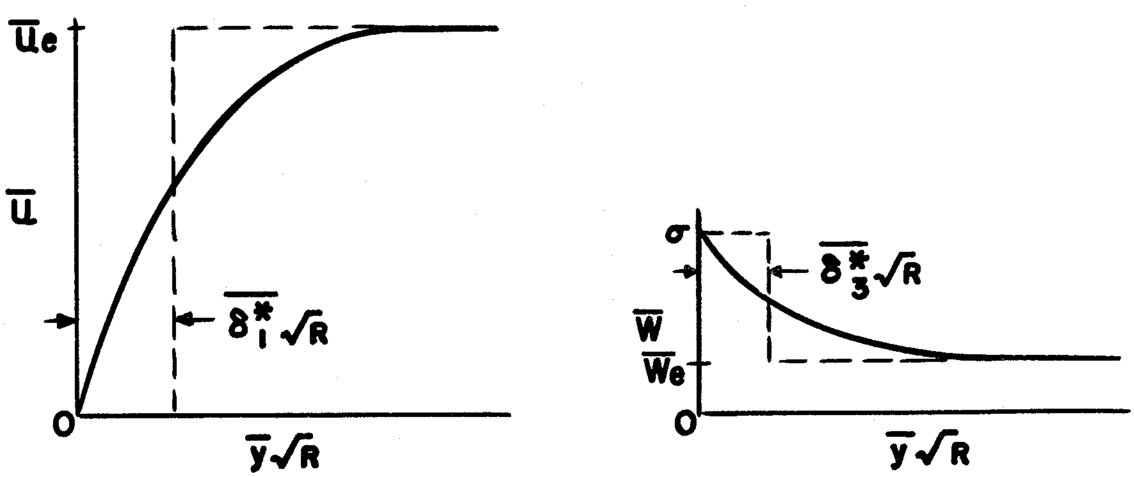

Graphical Representation of Displacement Parameters.

3. Effect of Spin

To examine the changes which occur in the boundary-layer distribution due to spinning the model at a given angle of incidence, we shall define the following quantities:

$$I\,(\bar{x},\theta;\ \alpha,\sigma) = -\int_0^{\bar{y}_e\sqrt{R}} \Delta\bar{u}\ d\bar{y}\sqrt{R} \qquad \text{(experiment)} \qquad (16)$$

$$= -\sqrt{\bar{x}}\int_0^{\infty} \Delta\bar{u}\ d\eta \qquad \text{(theory)} \qquad (16a)$$

where $\Delta\bar{u} = \bar{u}(\bar{y}\sqrt{R};\ \alpha,\sigma) - \bar{u}(\bar{y}\sqrt{R};\ \alpha,0)$

$$J\,(\bar{x},\theta;\ \alpha,\sigma) = -\int_0^{\bar{y}_e\sqrt{R}} \Delta\bar{w}\ d\bar{y}\sqrt{R} \qquad \text{(experiment)} \qquad (17)$$

$$= -\sqrt{\bar{x}}\int_0^{\infty} \Delta\bar{w}\ d\eta \qquad \text{(theory)} \qquad (17a)$$

where $\Delta\bar{w} = \bar{w}(\bar{y}\sqrt{R};\ \alpha,\sigma) - \bar{w}(\bar{y}\sqrt{R};\ \alpha,0)$

The existence of the integrals will be assured if we assume that $\bar{u}_e$ and $\bar{w}_e$ are unaffected by spin. The sign convention is such that positive numerical values of I and J correspond (algebraically) to increases in the quantities $[\bar{u}_e\overline{\delta_1^*}\sqrt{R}]$ and $[(\bar{w}_e-\sigma)\overline{\delta_3^*}\sqrt{R}]$, respectively.

The experimental values of I and J presented in Part V were obtained by measuring appropriate areas (see sketch below) on the velocity profile plots contained in Appendix D.

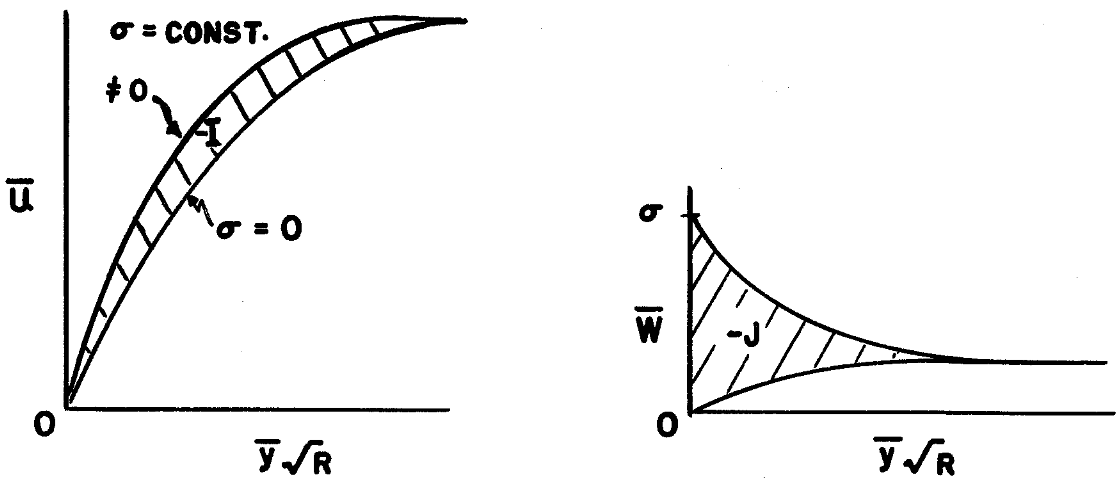

Graphical Representation of I and J

The theoretical values corresponding to integration of Martin's profiles (eqs. 5 and 7), are:

$$I_M = - \left[\alpha\sigma\bar{x}^{-5/2} \int_0^\infty f_2 \, d\eta\right] \sin\theta$$

$$= - 1.526\, \alpha\sigma\bar{x}^{-5/2} \sin\theta \tag{18}$$

$$J_M = - \left[\sigma\bar{x}^{-1/2} \int_0^\infty (1 - f_0') \, d\eta\right] - \left[\alpha\sigma\bar{x}^{-3/2} \int_0^\infty h_0 d\eta\right] \cos\theta$$

$$= - 1.721\, \sigma\bar{x}^{-1/2} + 2.760\, \alpha\sigma\bar{x}^{-3/2} \cos\theta \tag{19}$$

The numerical coefficients shown in equations 18 and 19 have been excerpted from equations 22 of reference 2. When the profiles obtained by Kelly and Thacker (eqs. 8 and 10) are integrated, the following values are obtained:

$$I_K = [1.047\ \alpha\sigma^2\bar{x}^{-7/2}]\cos\theta$$

$$- [1.524\ \alpha\sigma\bar{x}^{-5/2} - 0.615\ \alpha\sigma^3\bar{x}^{-9/2}]\sin\theta \qquad (20)$$

$$J_K = -[1.720\ \sigma\bar{x}^{-1/2}] + [2.756\ \alpha\sigma\bar{x}^{-3/2} - 1.096\ \alpha\sigma^3\bar{x}^{-7/2}]\cos\theta$$

$$+ [1.753\ \alpha\sigma^2\bar{x}^{-5/2}]\sin\theta \qquad (21)$$

The numerical coefficients in equations 20 and 21 are based on the values of the integrated profile functions given in the tables of reference 4.

4. Fourier Series Representation

The expressions obtained for the theoretical approximations of I and J in the previous section suggest that the complete solutions may be expressed as a pair of Fourier Series:

$$I = A_0(\bar{x};\alpha,\sigma) + \sum_{n=1}^{\infty} A_n(\bar{x};\alpha,\sigma)\cos n\theta + \sum_{n=1}^{\infty} B_n(\bar{x};\alpha,\sigma)\sin n\theta \qquad (22)$$

$$J = C_0(\bar{x};\alpha,\sigma) + \sum_{n=1}^{\infty} C_n(\bar{x};\alpha,\sigma)\cos n\theta + \sum_{n=1}^{\infty} D_n(\bar{x};\alpha,\sigma)\sin n\theta \qquad (23)$$

From experimental values of I and J obtained at several values of θ we shall be able to construct Fourier series representations of the experimental distributions of those two quantities. These will allow us to analyze the effects of spin in further detail by examining individual Fourier coefficients. Using measurements at k values of θ, where k is an even number and the values of θ are equally spaced around the body beginning from $\theta = 0$, the Fourier coefficients may be evaluated as follows:

Let

$$I_i = (\bar{x},\theta_i;\alpha,\sigma)$$
$$J_i = J(\bar{x},\theta_i;\alpha,\sigma)$$

where

$$\theta_i = \frac{2}{k}(i-1)\pi;\; i = 1,2,3,\ldots,k \text{ (even)}$$

then

$$A_0 = \frac{1}{k}\sum_{i=1}^{k} I_i$$

$$A_n = \frac{2}{k}\sum_{i=1}^{k} I_i \cos n\theta_i;\; n = 1,2,\ldots,\frac{k}{2}-1.$$

$$A_{\frac{k}{2}} = \frac{1}{k}\sum_{i=1}^{k} I_i \cos (i-1)\pi$$

$$B_n = \frac{2}{k}\sum_{i=1}^{k} I_i \sin n\theta_i;\; n = 1,2,\ldots\frac{k}{2}-1.$$

$$C_0 = \frac{1}{k}\sum_{i=1}^{k} J_i \tag{24}$$

$$C_n = \frac{2}{k}\sum_{i=1}^{k} J_i \cos n\theta_i;\; n = 1,2,\ldots,\frac{k}{2}-1.$$

$$C_{\frac{k}{2}} = \frac{1}{k}\sum_{i=1}^{k} J_i \cos (i-1)\pi$$

$$D_n = \frac{2}{k}\sum_{i=1}^{k} J_i \sin n\pi;\; n = 1,2,\ldots,\frac{k}{2}-1.$$

Thus, the experimental evaluation of each coefficient is independent of all other coefficients.

In Part V the experimental values of the Fourier coefficients are compared with theoretical values based on the coefficients of equations 18 through 21, as follows:

From Martin's results,

$$
\begin{aligned}
A_0 &= 0 \\
B_1 &= -1.526\,\alpha\sigma x^{-5/2} \\
C_0 &= -1.721\,\sigma x^{-1/2} \\
C_1 &= 2.760\,\alpha\sigma x^{-3/2}
\end{aligned}
\qquad (25)
$$

From the results of Kelly and Thacker,

$$
\begin{aligned}
A_0 &= 0 \\
A_1 &= 1.047\,\alpha\sigma^2 x^{-7/2} \\
B_1 &= -1.524\,\alpha\sigma x^{-5/2} + 0.615\,\alpha\sigma^3 x^{-9/2} \\
C_0 &= -1.720\,\sigma x^{-1/2} \\
C_1 &= 2.756\,\alpha\sigma x^{-3/2} - 1.096\,\alpha\sigma^3 x^{-7/2} \\
D_1 &= 1.753\,\alpha\sigma^2 x^{-5/2}
\end{aligned}
\qquad (26)
$$

5. Forces Due to Displacement Effect

In references 2, 3, and 4 the Magnus force due to the "displacement thickness effect" of the boundary layer is determined by means of slender body potential flow theory. We shall present here a somewhat revised version of that Magnus force analysis and we shall also include the determination of normal force. We shall then proceed to show how the Fourier coefficients discussed in the previous section can be usefully applied to such an analysis.

The velocity potential for the outer flow may be written as

$$\Phi = (1 - \frac{\alpha^2}{2})Ux - \alpha U(r + \frac{r_0^2}{r})\cos\theta + \varphi$$

where $\varphi(x,r,\theta;\alpha,\sigma,R)$ is the perturbation potential due to the boundary-layer flow. Since it is assumed that $\partial^2\varphi/\partial x^2$ is small, φ is required to satisfy only the two-dimensional Laplace equation (and specified boundary conditions) in the cross plane. The boundary conditions are:

$$\left(\frac{\partial\varphi}{\partial r}\right)_{r\to\infty} = 0$$

$$\left(\frac{\partial\varphi}{\partial r}\right)_{r=r_0} = \text{apparent outflow velocity*} = v_e - y_e\frac{\partial v_e}{\partial y}$$

The pressure coefficient, evaluated at the body surface is

$$C_p = \left(\frac{p - p_\infty}{\frac{1}{2}\rho U^2}\right)_{r_0} = -\frac{2}{U}\left(\frac{\partial\varphi}{\partial x}\right)_{r_0} + O(\alpha^2) \tag{27}$$

The standard sign conventions for defining the directions of the forces on the spinning body are shown by the accompanying sketch:

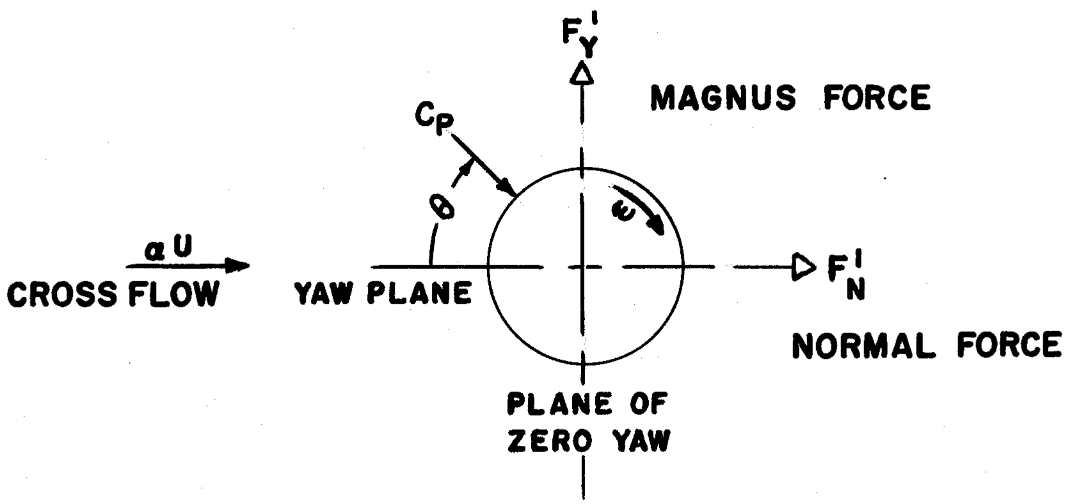

---

*In references 2, 3, and 4, the boundary value of $\partial\phi/\partial r$ at the surface was obtained by first computing Δ^* (by eqn. 11a) and then evaluating $U\partial\Delta^*/\partial x$. That procedure, however, is unnecessary, since the equating of $(\partial\phi/\partial r)_{r=r_0}$ to the apparent outflow velocity is, in fact, the basis for the derivation of Δ^* (refs. 16, 17).

The Magnus force per unit length may be computed as

$$F'_Y = -\frac{1}{2}\rho U^2 \int_0^{2\pi} C_p r_0 \sin\theta \, d\theta \tag{28}$$

The Magnus force coefficient, over the length from the origin of the boundary layer to a given axial station, may be expressed, in the terminology of aerodynamics, as

$$C_Y = \frac{\int_0^x F'_Y \, dx}{\frac{1}{2}\rho U^2 \pi r_0^2} \tag{29}$$

The normal force per unit length may be computed as

$$F'_N = \frac{1}{2}\rho U^2 \int_0^{2\pi} C_p r_0 \cos\theta \, d\theta \tag{30}$$

and the normal force coefficient may be expressed as

$$C_N = \frac{\int_0^x F'_N \, dx}{\frac{1}{2}\rho U^2 \pi r_0^2} \tag{31}$$

Substitution of equation 27 into equation 28 will show that the only disturbances which produce a Magnus force are those which vary with x and are not symmetric about the yaw plane. Substitution of equation 27 into equation 30 will show that the only disturbances which produce a normal force are those which vary with x and are not symmetric about the plane of zero yaw.

Under perfect conditions, the boundary layer on the non-spinning cylinder at a small angle of incidence should be symmetric about the yaw plane but non-symmetric about the plane of zero yaw.

Hence, with zero spin, the Magnus force is zero, and the normal force can be computed by the procedure outlined. In the analysis which follows, however, we shall consider only the changes associated with spinning of the body (at a small angle of incidence).

The increment of outflow velocity due to spin may be computed from the experimental velocity profiles (as well as from the theoretical profiles) by integrating the continuity equation across the boundary layer. For a given combination of $\bar{x}$, θ we let

$$\Delta\bar{v} = \bar{v}(\bar{y}\sqrt{R};\alpha,\sigma) - \bar{v}(\bar{y}\sqrt{R};\alpha,0)$$

and define $\Delta\bar{u}$ and $\Delta\bar{w}$ in a similar manner, as before (in eqns. 16, 17).

Then

$$\Delta\bar{v}_e\sqrt{R} = \lim_{\bar{y}\to\bar{y}_e} \Delta\bar{v}\sqrt{R}$$

$$= -\int_0^{\bar{y}_e\sqrt{R}} \frac{\partial\Delta\bar{u}}{\partial\bar{x}}\, d\bar{y}\sqrt{R} - \int_0^{\bar{y}_e\sqrt{R}} \frac{\partial\Delta\bar{w}}{\partial\theta}\, d\bar{y}\sqrt{R} \qquad (32)^*$$

Introducing I and J from equations 16 and 17 into equation 32

$$\Delta\bar{v}_e\sqrt{R} = \frac{\partial I}{\partial\bar{x}} + \frac{\partial J}{\partial\theta} \qquad (32a)$$

----

*The theoretical values of Δv_e could be determined directly foom the limiting values of the profile functions in the expressions for v given by equations 6 and 9. For example, from Martin's result (eqn. 6), $\Delta\bar{v}_e R = \alpha\sigma\bar{x}^2 g_1(\infty) \sin\theta$; and from the tables of reference 2 we find $g_1(\infty) = -6.575$.

Substitution of the Fourier series (equations 22 and 23) into equation 32a gives

$$\Delta\bar{v}_e\sqrt{R} = \frac{\partial A_0}{\partial \bar{x}} + \sum_{n=1}^{\infty} \left(\frac{\partial A_n}{\partial \bar{x}} + nD_n \right) \cos n\theta + \sum_{n=1}^{\infty} \left(\frac{\partial B_n}{\partial \bar{x}} - nC_n \right) \sin n\theta \quad (32b)$$

Thus, from equation 32b, we may write

$$\left(\frac{\partial \varphi_Y}{\partial r} \right)_{r_0} = \frac{U}{\sqrt{R}} \left(\frac{\partial B_1}{\partial \bar{x}} - C_1 \right) \sin \theta \quad (33)$$

$$\left(\frac{\partial \varphi_N}{\partial r} \right)_{r_0} = \frac{U}{\sqrt{R}} \left(\frac{\partial A_1}{\partial \bar{x}} + D_1 \right) \cos \theta \quad (34)$$

where ϕ_Y and ϕ_N are the portions of ϕ which contribute respectively to the Magnus force and to the normal force increment due to spin.

Far from the body $\frac{\partial \varphi_Y}{\partial r}$ and $\frac{\partial \varphi_N}{\partial r}$ must vanish. The solutions, therefore, are

$$\varphi_Y = - \frac{r_0^2}{r} \frac{U}{\sqrt{R}} \left(\frac{\partial B_1}{\partial \bar{x}} - C_1 \right) \sin \theta \quad (35)$$

$$\varphi_N = - \frac{r_0^2}{r} \frac{U}{\sqrt{R}} \left(\frac{\partial A_1}{\partial \bar{x}} + D_1 \right) \cos \theta \quad (36)$$

The dependence of the Magnus force coefficient C_Y upon the Fourier coefficients B_1 and C_1 may be derived by substituting equation 35 into equation 27 and proceeding to equations 28 and 29, as follows:

$$(\Delta C_p)_Y = \frac{2r_0}{\sqrt{R}} \frac{\partial}{\partial \bar{x}} \left(\frac{\partial B_1}{\partial \bar{x}} - C_1 \right) \sin \theta \quad (37)$$

$$F_Y' = -\frac{\rho U^2 \pi r_0^2}{\sqrt{R}} \frac{\partial}{\partial x}\left(\frac{\partial B_1}{\partial \bar{x}} - C_1\right) \tag{38}$$

$$C_Y = \frac{2}{\sqrt{R}}\left[C_1(\bar{x};\alpha,\sigma) - \frac{\partial}{\partial \bar{x}} B_1(\bar{x};\alpha,\sigma) \right] \tag{39}$$

The relation between the incremental normal force coefficient ΔC_N and the Fourier coefficients A_1 and D_1 may be obtained by substituting equation 36 into equation 27 and proceeding to equations 30 and 31, as follows:

$$(\Delta C_p)_N = \frac{2r_0}{\sqrt{R}} \frac{\partial}{\partial x}\left(\frac{\partial A_1}{\partial \bar{x}} + D_1\right) \cos\theta \tag{40}$$

$$\Delta F_N' = \frac{\rho U^2 \pi r_0^2}{\sqrt{R}} \frac{\partial}{\partial x}\left(\frac{\partial A_1}{\partial \bar{x}} + D_1\right) \tag{41}$$

$$\Delta C_N = \frac{2}{\sqrt{R}}\left[\frac{\partial}{\partial \bar{x}} A_1(\bar{x};\alpha,\sigma) + D_1(\bar{x};\alpha,\sigma) \right] \tag{42}$$

An analysis of the nature of the variation of Magnus force with spin, based on experimental values of B_1 and C_1 obtained at several spin rates, is presented in Part V. A similar analysis of the effect of spin on normal force, based on the corresponding values of A_1 and D_1, is also presented in Part V. Those analyses are necessarily qualitative because nearly all of the measurements involved were obtained at only one axial station and, therefore, do not provide the data required for evaluating the derivatives $\frac{\partial B_1}{\partial \bar{x}}$ and $\frac{\partial A_1}{\partial \bar{x}}$, which appear in the equations for the Magnus force coefficient (eqn. 39) and the normal force coefficient (eqn. 42), respectively.

For reference purposes we shall list here the theoretical values of the Magnus force and incremental normal force coefficients which are obtained by the present method of analysis when the boundary-layer solutions of Martin (ref. 2) and of Kelly and Thacker (ref. 4) are used. Substitution of B_1 and C_1 from equations 25 (based on ref. 2) into equation 39 gives, for the predicted Magnus force coefficient,

$$C_Y = 13.15 \frac{\alpha\sigma x^{-3/2}}{\sqrt{R}} \tag{43}$$

The values of B_1 and C_1 from the approximations of higher order in σ given by equations 26 (based on ref. 4), when substituted into equation 39, predict the Magnus force coefficient to be

$$C_Y = 13.13 \frac{\alpha\sigma x^{-3/2}}{\sqrt{R}} - 7.728 \frac{\alpha\sigma^3 x^{-7/2}}{\sqrt{R}} \tag{44}$$

The predicted incremental normal force coefficient due to spin, obtained by substituting A_1 and D_1 from equations 26 (based on ref. 4) into equation 42, is

$$\Delta C_N = 10.84 \frac{\alpha\sigma^2 x^{-5/2}}{\sqrt{R}} \tag{45}$$

These values, of course, represent only the forces due to displacement effect and do not include the radial pressure gradient and skin friction effects considered in references 3 and 4.

V. RESULTS

All of the symbols and nomenclature used in discussing the results are defined either in the list of symbols preceding Part I or in figure 1. The following items, however, warrant particular mention for the sake of clarity:

a) All barred symbols (such as $\overline{u}$, $\overline{y}$, etc.) are dimensionless scalar quantities.

b) The dimensionless boundary-layer velocity components $\overline{u}$ and $\overline{w}$ are both referred to the absolute velocity U at the outer edge of the boundary layer, i.e., $\overline{u} = u/U$ and $\overline{w} = w/U$.

c) The radius r_0 of the cylindrical section of the body provides the standard unit of measure for the dimensionless lengths $\overline{x}$, $\overline{y}$, $\overline{\delta_1^*}$, $\overline{\delta_3^*}$ (and also θ), e.g. $\overline{x} = x/r_0$, $\overline{y} = y/r_0$, etc.

d) Angle of yaw α is synonymous to angle of attack or angle of incidence since the body is axially symmetric and the origin of the coordinate θ is defined by the plane in which α lies ("yaw plane").

e) The dimensionless spin rate σ is the ratio of the peripheral speed of the cylindrical section of the body to the air speed at the outer edge of the boundary layer, i.e. $\sigma = \omega r_0/U$.

f) The radius r_0 is used as the characteristic length in the Reynolds number R, i.e. $R = Ur_0/\nu$.

1. Non-spinning Body at Zero Yaw

<u>Velocity Profiles</u>: Axial velocity profiles measured in the boundary layer at one position ($\ell/r_0 = 11.4$, $\theta = 3\pi/2$) on the

non-spinning model at zero yaw are summarized in figure 7 for several Reynolds numbers from R ≙ 9,000 to R ≙ 33,000 (based on r_0). Similarity of the profiles in terms of $\sqrt{R}$ is verified by the close agreement of the data over the range of R. Measurements at other positions on the body for this case ($\alpha = \sigma = 0$) are included in Appendix C. The data shown (for $\sigma = 0$) in figure C3* indicate agreement among the axial velocity profiles for three different θ positions ($0, \frac{3\pi}{2}, \pi$) at one axial station ($\ell/r_0 = 11.4$) with zero yaw. The axial velocity profile measured at the forward axial station ($\ell/r_0 = 10.2$) with zero yaw and zero spin appears in figure C5.

Determination of Effective Origin of $\overline{x}$: In order to compare the similarity boundary-layer solutions for a theoretical, open-ended cylinder (refs. 1 through 5) against the boundary-layer measurements obtained at a given axial station on the cylindrical section of the experimental model, it is necessary to determine an empirical value for the length $\overline{x}$ which appears in the theoretical equations (Part IV). This was accomplished by choosing the value of $\overline{x}$ which would best fit a Blasius velocity profile (using $\overline{y}\sqrt{R} = \eta\sqrt{\overline{x}}$) to the boundary-layer velocity measurements for the basic case of zero spin at zero yaw. The values which were chosen by this fitting process are as follows (where ℓ is measured from the nose of the model as shown in figure 1):

at $\ell/r_0 = 11.4$, $\overline{x} = 6.5$ (fig. 7)

----

*Figures numbered with a letter prefix will be found in the Appendix designated by the letter.

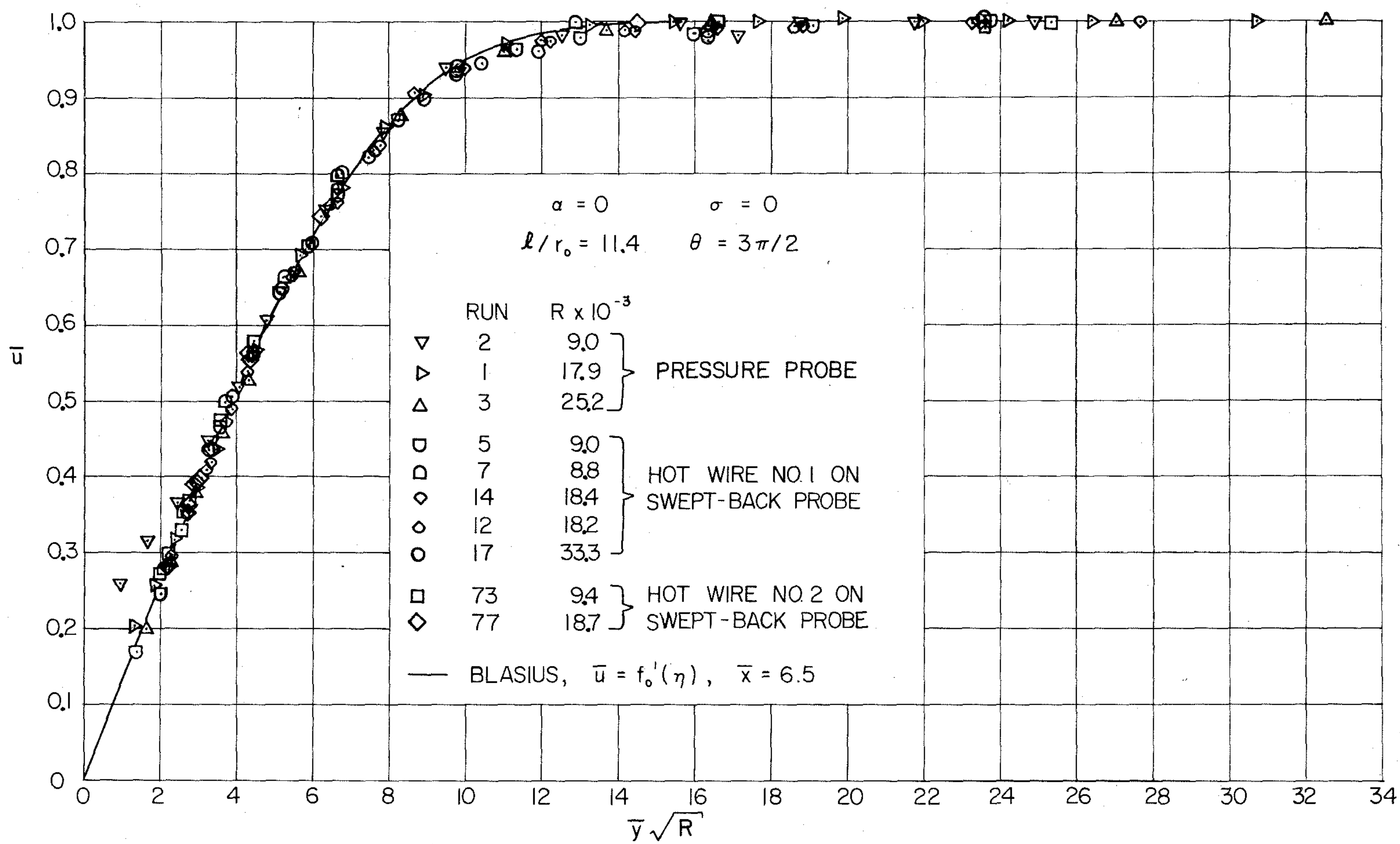

FIGURE 7

BOUNDARY LAYER VELOCITY PROFILES ON MODEL AT ZERO YAW WITH NO SPIN at $\ell/r_0 = 10.2$, $\bar{x} = 5.3$ (fig. C5)

From each of the two cases we may infer that the origin of $\bar{x}$ is at $\ell/r_0 = 4.9$. These results, therefore, indicate boundary-layer similarity in $\sqrt{R/\bar{x}}$ (where $R = Ur_0/\nu$ and $\bar{x} = \ell/r_0 - 4.9$) over the region of measurement.

Transverse Velocity Measurements: Under ideal conditions the boundary-layer flow on the model at $\alpha = \sigma = 0$ should be entirely in the axial direction. Measurements of the transverse component ($\bar{w}$) of the boundary-layer velocity indicated by the directionally-sensitive hot wire are included in Appendix C to show the extent of idealization accomplished in the experiments on the non-spinning model at zero yaw. It should be observed that in figures C2 and C4 the data are plotted on an expanded scale. Deviations in the measurements on top of the model ($\theta = 3\pi/2$, figs. C2, C4, C6) were extremely small and randomly distributed about $\bar{w} = 0$. On the sides of the model ($\theta = 0, \pi$, fig. C4) indications of a boundary-layer flow deflection of as much as 4 degrees were observed near the surface of the model. Measurements of the direction of flow at the outer edge of the boundary layer in these cases ($\theta = 0, \pi$), however, indicate that the model was not pitched with respect to the outer flow. In view of the fact that the V-shaped hot wire was in a vertical plane for the measurements on the sides of the model, it is possible that the observed deviations represent some sort of convection error rather than actual flow deflections. Since the axial component $\bar{u}$ involves the cosine of the measured flow deflection angle, the effect of these deviations is negligible in the axial velocity profiles (fig. C3). Also, in the determination of the transverse component on the spinning body, the effect of a given error in direction will diminish as the spin rate increases.

2. Spinning Body at Zero Yaw

Typical measurements of axial and transverse velocity profiles, respectively, for various spin rates at zero incidence are shown in figs. 8 and 9. Additional data, including the turbulent profiles encountered at $\sigma = \pm 0.6$, are presented in Appendix C.

In the theoretical results (refs. 2, 4) the axial velocity profile at a given $\bar{x}$ is not affected by spin at $\alpha = 0$ (see Part IV, eqns. 5, 8). The experimental results, on the other hand, show a shifting of the axial profiles (at a given station) toward lower velocity, i.e. increasing displacement thickness, with increasing spin. It has been shown, for the non-spinning body, that an empirical choice of the similarity length $\bar{x}$ is required in order to relate the theoretical profile to the experimental data. There is a possibility, therefore, that the shifting of the experimental velocity profiles on the spinning body might be empirically described as a shifting of the origin of similarity. To examine this possibility, theoretical profiles for several values of $\sqrt{\bar{x}}$ have been superimposed on the experimental data for both the axial and the transverse components. In the case of the axial velocity profiles (fig. 8), a value of $\sqrt{\bar{x}}$ for each spin rate has been shown for which the Blasius function fits the experimental data reasonably well near the middle of the boundary-layer profile (though not so well

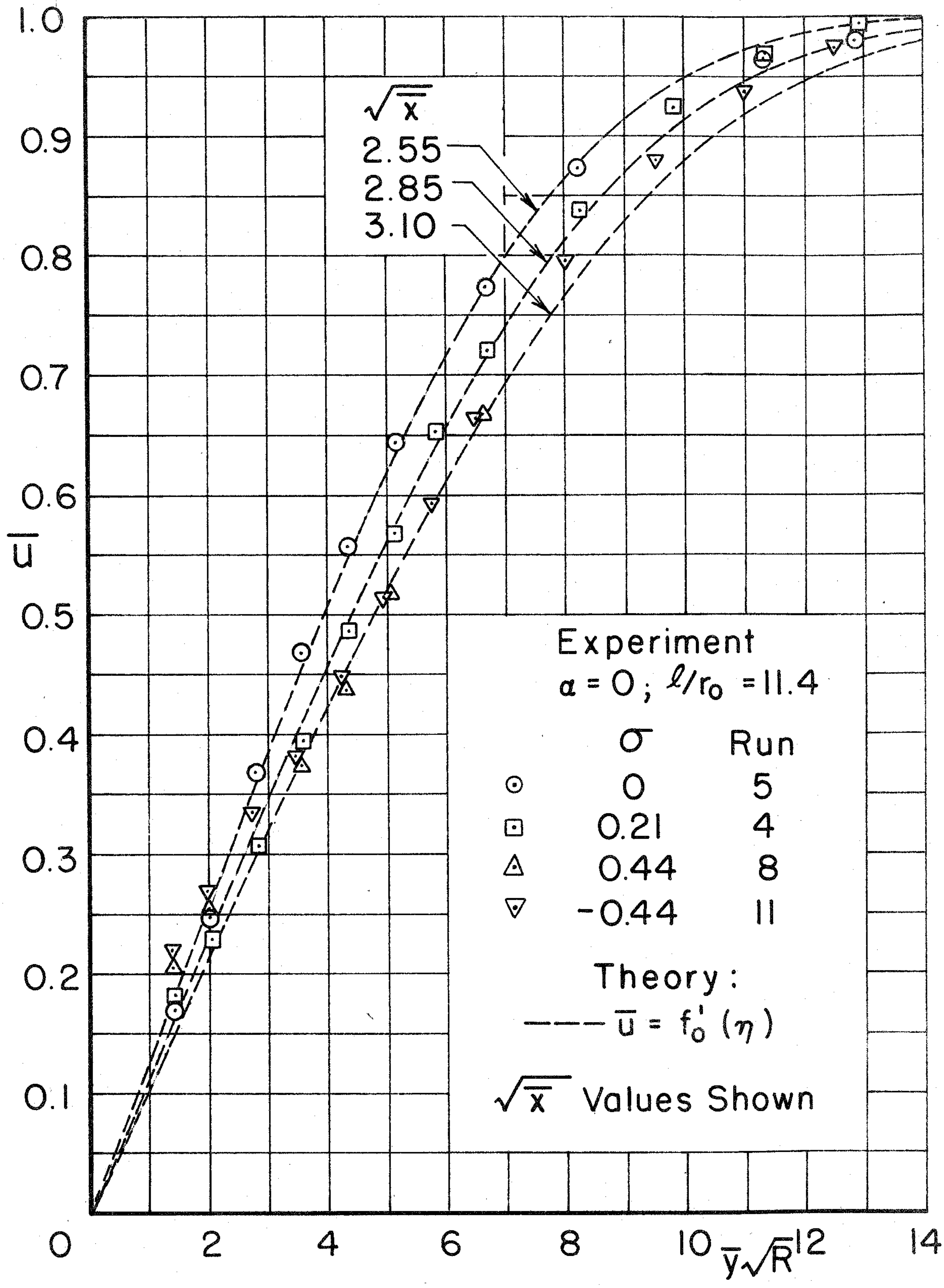

FIGURE 8
AXIAL VELOCITY PROFILES ON SPINNING MODEL AT ZERO YAW

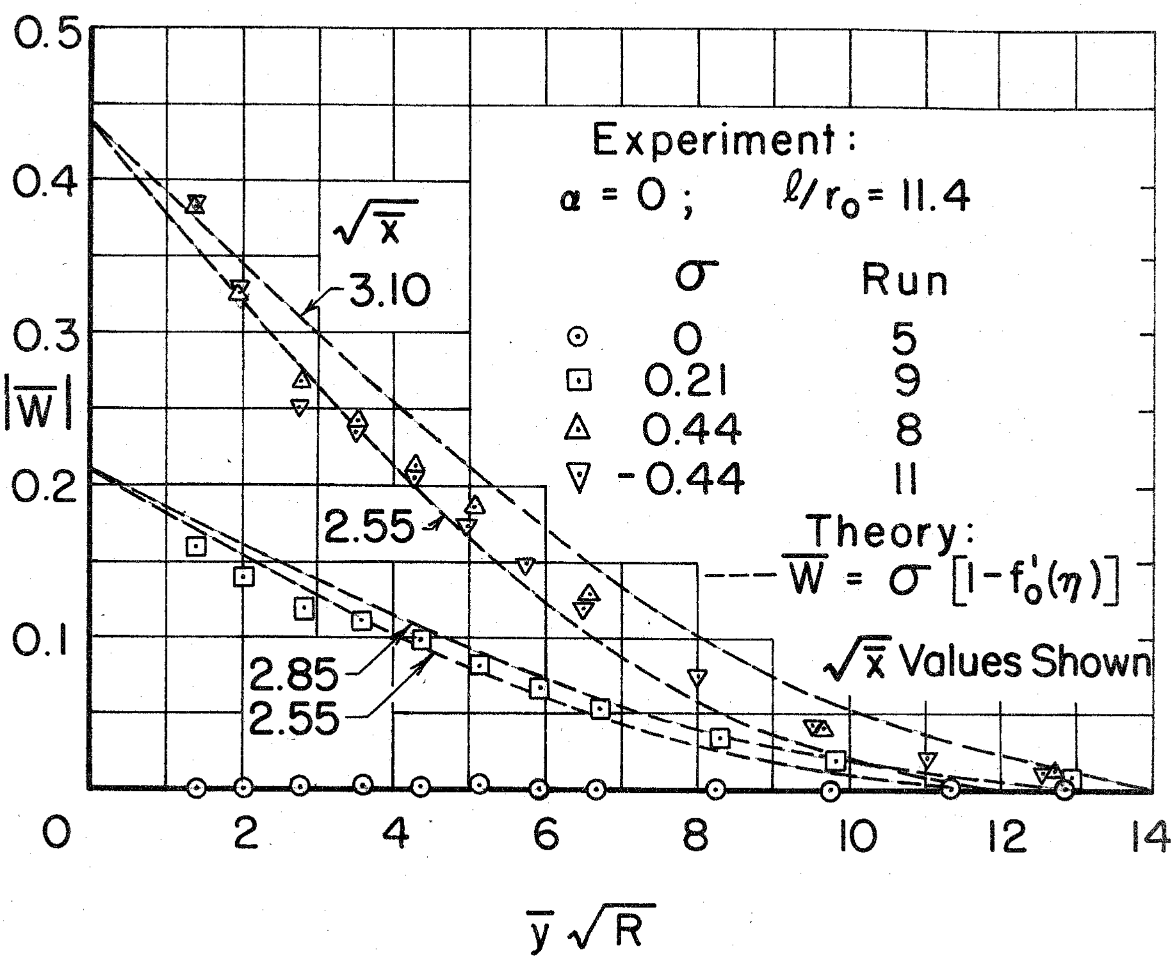

FIGURE 9
TRANSVERSE VELOCITY PROFILES ON SPINNING MODEL AT ZERO YAW

toward the ends). In the case of the transverse velocity profiles (fig. 9), however, the value $\sqrt{\bar{x}} = 3.10$, which fits the experimental axial profile for $\sigma = \pm 0.44$ does not fit the corresponding transverse velocity measurements. The value $\sqrt{\bar{x}} = 2.55$, based on the zero spin measurements, appears to give a fairly good fit to all the transverse velocity data for $|\sigma| \leq 0.44$ (also see Appendix C).

A more comprehensive evaluation of the effect of spin at zero yaw is provided in figure 10, where all of the measurements obtained for this case are summarized in terms of the axial and transverse displacement parameters.

If it is assumed that the effective origin of similarity of the boundary-layer changes with spin, then the ordinates of the data in figure 10 may be regarded as representing values of $\sqrt{\bar{x}}$: From the numerical results of references 2 or 4 and from the definitions given in Part IV (eqns. 14a, 15a), the theoretical displacement parameters are:

$$\overline{\delta_1^*}\sqrt{R} = \overline{\delta_3^*}\sqrt{R} = 1.72\sqrt{\bar{x}}$$

thus,
$$\sqrt{\bar{x}} = \frac{\overline{\delta_1^*}\sqrt{R}}{1.72} = \frac{\overline{\delta_3^*}\sqrt{R}}{1.72}$$

The dilemma presented by the data in figure 10 is that, for the higher spin rates ($\sigma \geq 0.2$), the experimental values of $\overline{\delta_1^*}$ and $\overline{\delta_3^*}$ for a given spin rate are not equal; the net change from the zero spin value is approximately twice as large for the axial parameter ($\overline{\delta_1^*}$) as for the transverse parameter ($\overline{\delta_3^*}$).

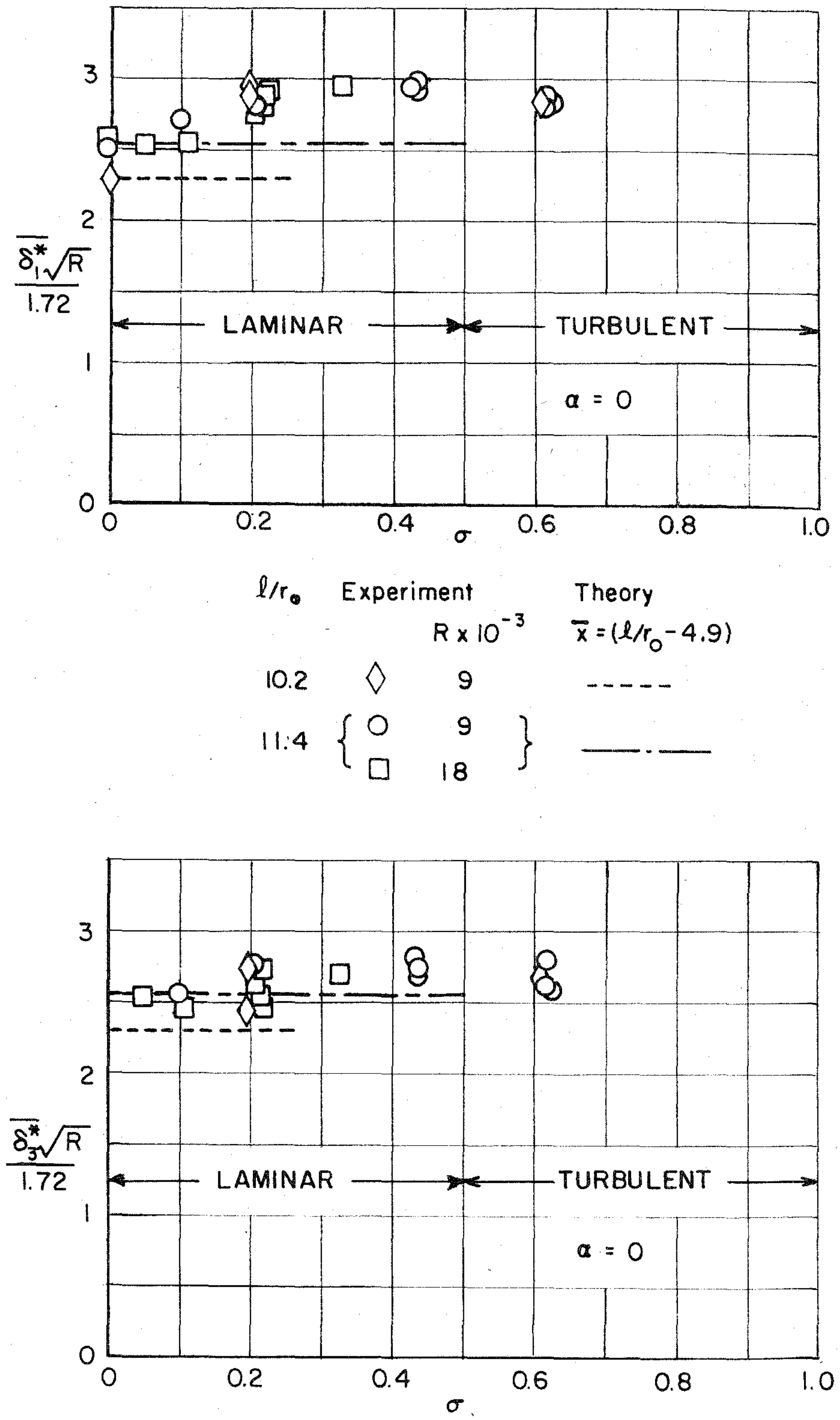

FIGURE 10

EFFECT OF SPIN ON DISPLACEMENT PARAMETERS AT ZERO YAW

A different method for representing the effects of spin at zero yaw is provided by assuming that the complete solutions for the velocity components contain terms involving powers of σ (while retaining the required symmetry at $\alpha = 0$):

$$\bar{u} = f_0' + \sigma^2 f_{02} + \sigma^4 f_{04} + \cdots \qquad (46)$$

$$\bar{w} = \sigma(1 - f_0') + \sigma^3 f_{03} + \sigma^5 f_{05} + \cdots \qquad (47)$$

The leading term on the right-hand side in each of the above equations is the same as the corresponding term in equations 5 and 8, respectively. To match the experimental profiles, the sum of the additional terms, in each equation, must be negative. Under this representation, then, the displacement parameters (for $\alpha = 0$) become:

$$\overline{\delta_1^*} \sqrt{R} = \sqrt{\bar{x}}\ (1.72 + \sigma^2 F_{02} + \sigma^4 F_{04} + \cdots) \qquad (48)$$

$$\overline{\delta_3^*} \sqrt{R} = \sqrt{\bar{x}}\ (1.72 + \sigma^2 F_{03} + \sigma^4 F_{05} + \cdots) \qquad (49)$$

where $$F_{0i} = -\int_0^\infty f_{oi}\, d\eta$$

and the sum of the added terms (involving powers of σ) is positive in each equation.

In the theoretical computations used in the analyses of the incremental effects of combined spin and yaw given elsewhere in this paper, it is assumed, for the sake of simplicity, that $\bar{x}$ is unaffected by spin. Thus, in effect, the representation of $\bar{u}$ and $\bar{w}$ given by equations 46 and 47 has been adopted in those analyses.

It should be mentioned that the simplified equations of motion, and boundary conditions, given in Part IV are satisfied by $f_{03} = f_{02}$, $f_{05} = f_{04}$, etc. (see eqns. 46, 47), and, therefore, the dilemma of the experimental values of $\overline{\delta_1^*}$ and $\overline{\delta_3^*}$ is not resolved unless the boundary conditions and/or the pressure gradient terms are altered. Kelly and Thacker (ref. 4, pp. 32-33) have concluded, further, that the given equations and boundary conditions are satisfied only by the trivial solutions f_{01}, etc. = 0.

3. Non-spinning Body Yawed 3 Degrees

Hot-wire measurements presented in figure 11 show the axial velocity profile in the boundary layer at $\theta = 0$ and $\ell/r_0 = 11.4$ on the yawed ($\alpha = 3^{\circ}$) model with zero spin. The effect of yaw on the velocity profile at this position is indicated by comparison with the theoretical (Blasius) profile for $\overline{x} = 6.5$ (which has previously been shown to agree with the experimental data obtained at $\alpha = 0^{\circ}$). The measurements are also compared with theoretical profiles for $\alpha = 3^{\circ}$, $\theta = 0$, predicted by approximations to various order in α, using $\overline{x} = 6.5$. It should be emphasized that many of the terms which appear in the theoretical approximations (e.g. Part IV, eqn. 5) involve powers of the product $\alpha\overline{x}$, which, in this case, has the relatively large value of 0.34. The results shown in figure 11 indicate that, over the inner portion ($\overline{y}\sqrt{R} < 6$) of the profile, the first order approximation and the third order* approximation agree reasonably well

----

*Computations for the α^3 approximation for this case were contributed by Mr. Nathan Gerber of BRL.

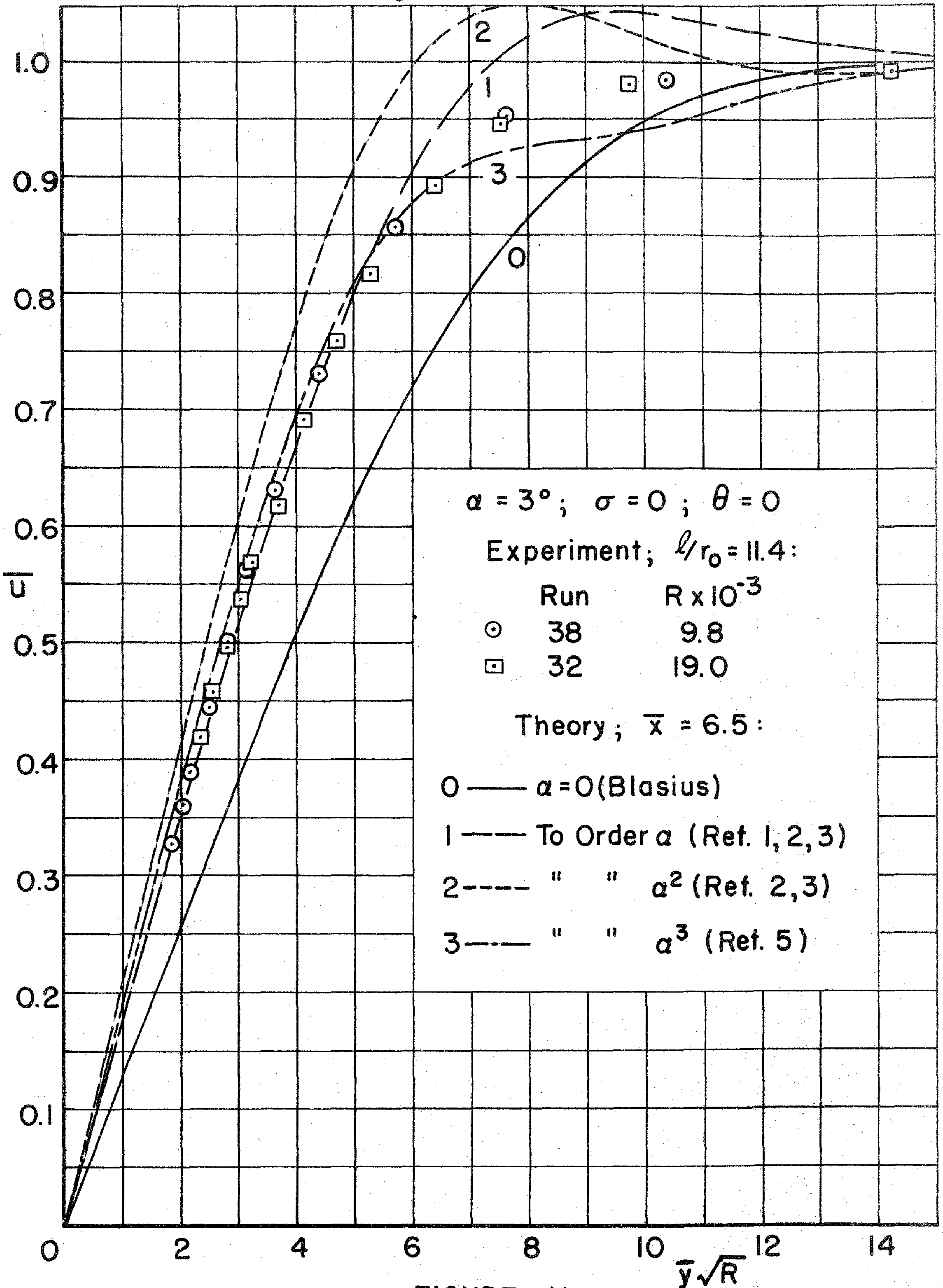

FIGURE 11

EXPERIMENTAL VELOCITY PROFILE AT $\theta = 0$ ON YAWED NON-SPINNING MODEL COMPARED WITH VARIOUS THEORETICAL APPROXIMATIONS with the measurements, while the second order approximation tends to overestimate the effect of yaw. Near the outer portion of the boundary layer, the theoretical profiles based on the first and second order approximations (for $\alpha\bar{x} = 0.34$, $\theta = 0$) have an over-shoot past $\bar{u} = 1$ (also see fig. 5 in ref. 2). When the theoretical approximation is extended to include terms of order α^3, the over-shoot is replaced by an inflection which under-shoots the physical profile. Presumably, one or two further perturbations would provide an approximation that would fit the experimental data of figure 11 over the entire profile.

Although theoretical axial and transverse velocity profiles (based on second order approximations of ref. 2 and ref. 4) for other values of θ (and other values of σ) were computed and plotted for use in the preliminary examination of the experimental data, those theoretical profiles have not been included in the present report because the appropriate comparisons between theory and experiment can be shown more succinctly by other methods of presentation. Theoretical velocity profiles for $\sigma = 0$ and $\theta = 0$, $\pi/2$, π, $3\pi/2$ which are comparable to the present case ($\alpha = 3^\circ$ $\bar{x} = 6.5$) may be found in figure 5 of reference 2 ($\alpha = 1^\circ$, $\bar{x} = 20$).

Hot-wire measurements presented in figures D1 and D2 show, respectively, the axial and the transverse velocity profiles for seven different azimuthal (θ) positions at one axial station ($\ell/r_0 = 11.4$) on the non-spinning model, with $\alpha = 3^\circ$.

In figure D2, the deviations from $\overline{w} = 0$ at $\theta = 0$ and $\theta = \pi$ are of about the same order as for the unyawed case (fig. C4) previously discussed. On the windward side ($\pi/2 > \theta > 3\pi/2$) of the model, both the axial and the transverse profiles appear to have a reasonable pattern of symmetry. On the lee side ($\pi/2 < \theta < 3\pi/2$), however, the profiles at $\theta = 3\pi/4$ and at $\theta = 5\pi/4$ show considerable disagreement with each other, in both the axial and the transverse components. It is of interest to note that, for this case ($\sigma = 0$, $\alpha = 3^{\circ}$, $\overline{x} = 6.5$), equation 7 (second order approximation based on ref. 2) predicts an inflection in the theoretical $\overline{w}$ profiles (not shown) at $\theta = 3\pi/4$ and $\theta = 5\pi/4$ much like the inflection shown in the experimental $\overline{w}$ profile at $\theta = 5\pi/4$ (Δ's, fig. D2).

The boundary-layer pattern encountered at $\ell/r_0 = 11.4$ on the experimental model, with a yaw angle of 3 degrees and zero spin, is summarized in figure 12, where the azimuthal distributions of $\overline{u}_e\overline{\delta_1^*}\sqrt{R}$ and $\overline{w}_e\overline{\delta_3^*}\sqrt{R}$ (see Part IV) based on graphical integration of the velocity profiles (figs. D1, D2) are compared with the theoretical distributions (for $\overline{x} = 6.5$) based on approximations to order α (i.e. $\alpha\overline{x}$) and to order α^2 (i.e., $\alpha^2\overline{x}^2$), using tables of ref. 2. Although the theoretical approximations may not necessarily give an accurate prediction of the boundary-layer distribution at this value of $\alpha\overline{x}$, it is certain that under favorable test conditions the experimental boundary layer ought to be symmetrical about the plane of yaw. The departure from symmetry in the experimental data shown in figure 12 is too great to be explained

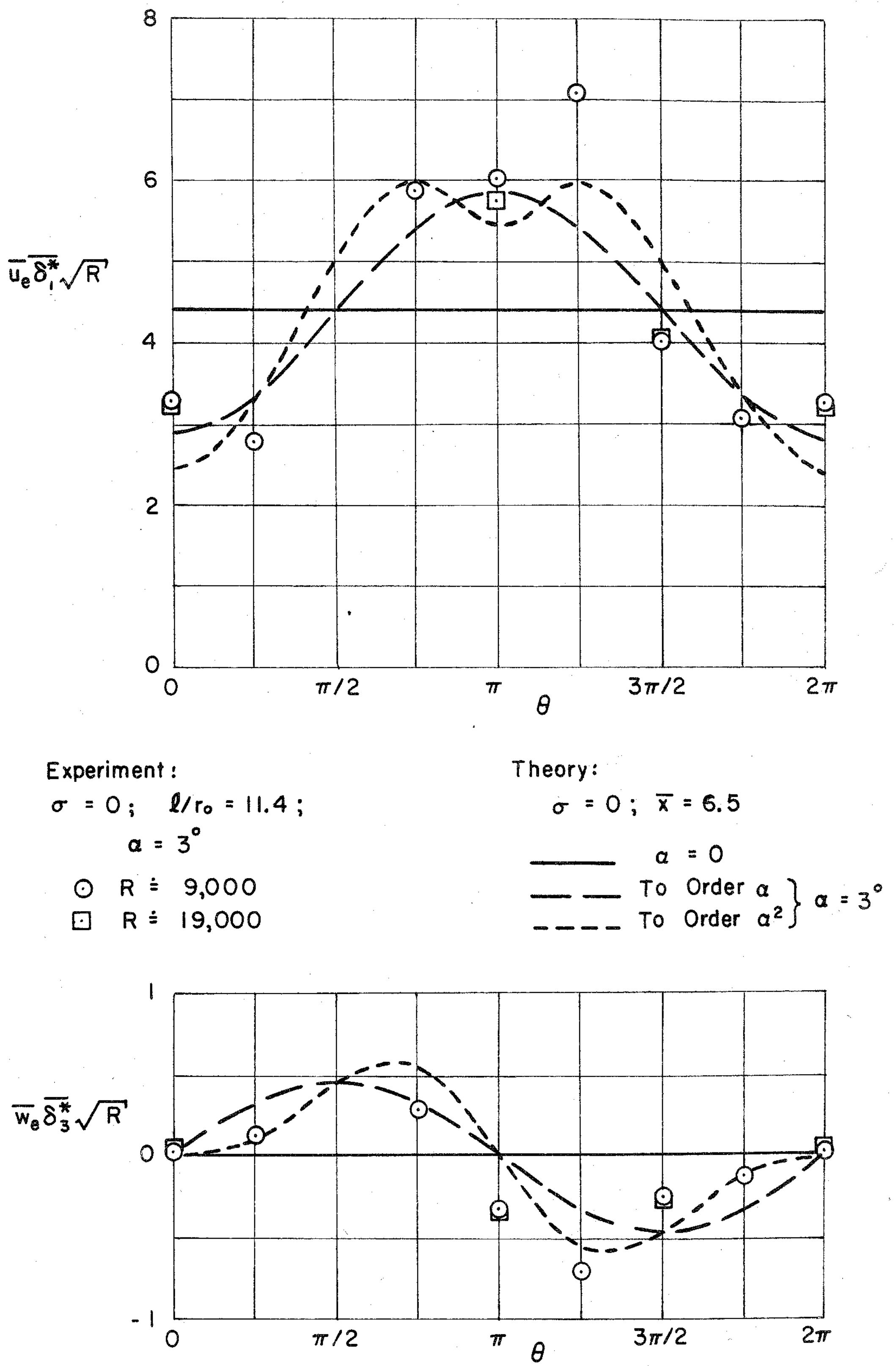

FIGURE 12

AZIMUTHAL DISTRIBUTION OF BOUNDARY LAYER ON SLIGHTLY YAWED BODY WITH NO SPIN by any of the small errors which may have been involved in the positioning of the probe to the correct value of θ or in setting the pitch and yaw angles of the model. It is supposed, therefore, that the lack of symmetry on the lee side ($\pi/2 < \theta < 3\pi/2$) resulted from imperfect test conditions such as flow disturbances caused by the structures supporting the model and the probe actuator. In the following analysis of the effects of spin, it is assumed that these same conditions were present when the model was spinning.

4. Spinning Body Yawed 3 Degrees

Boundary-layer measurements shown in figures D3 through D28 describe the velocity profiles, for various spin rates (up to $\sigma \doteq 0.6$), at each of several positions (of ℓ/r_0 and θ) on the spinning model, with a yaw angle of 3°.

To evaluate the effects of spin the profiles measured at zero spin were used as "tare readings," in the graphical integration of the increments represented by the quantities I and J (Part IV, eqns. 16, 17). The justification for this method lies in the procedure by which the measurements were obtained: with the probe actuator set-up at a given position of ℓ/r_0 and θ, measurements were made both with spin and with no spin, without disturbing the set-up. Repeatability of the zero spin measurements (see figs. D1, D2) with different set-ups, furthermore, was very good.

The azimuthal distributions of the experimental values of I and J at $\ell/r_0 = 11.4$ for three spin rates are shown in figures 13, 14, and 15. Also shown, in these figures, are the theoretical distributions of I and J predicted by equations 18, 19 (based on ref. 2) and equations 20, 21 (based on ref. 4) assuming $\overline{x} = 6.5$

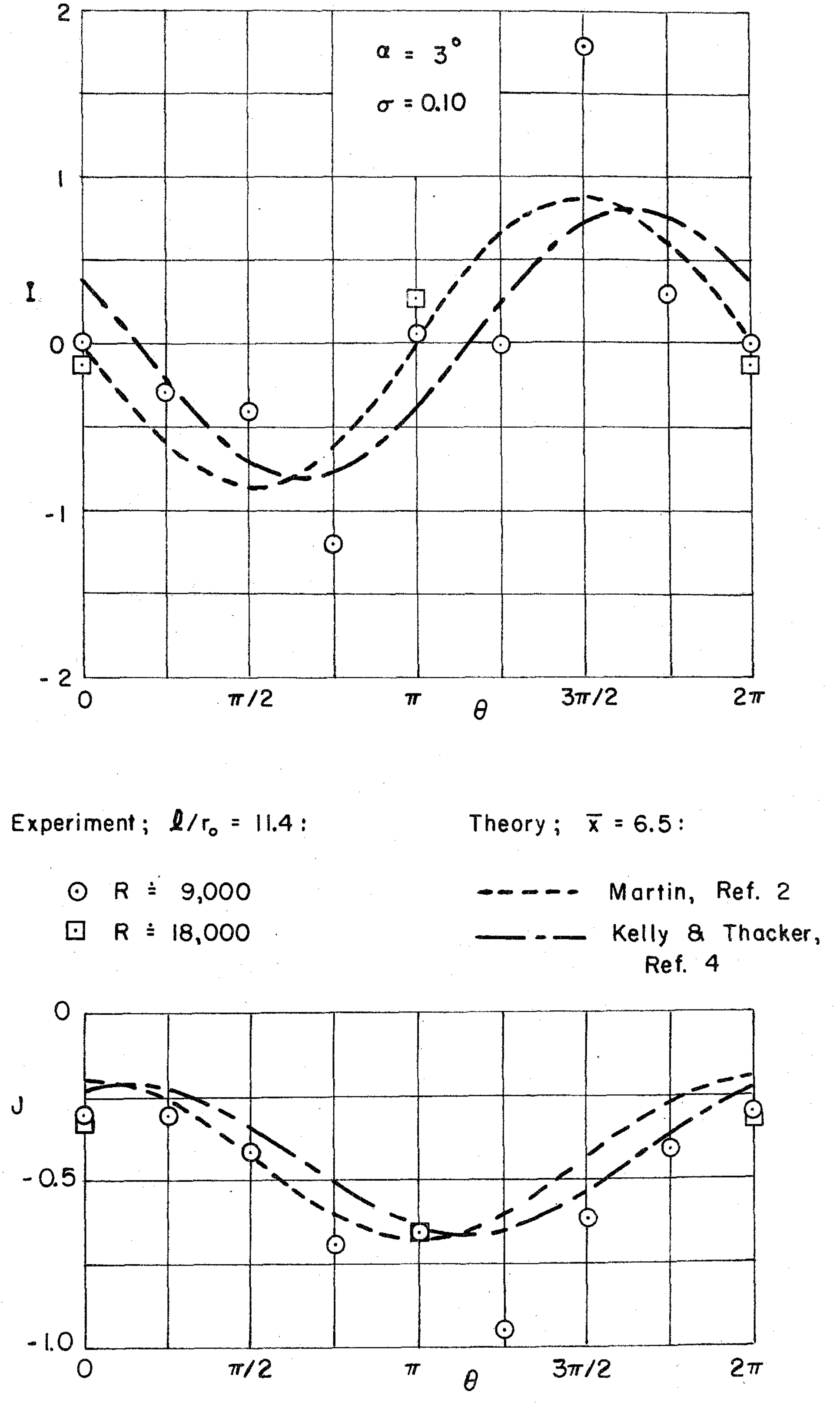

FIGURE 13

EXPERIMENTAL DISTRIBUTIONS OF I AND J AT $\sigma = 0.10$ COMPARED WITH THEORETICAL APPROXIMATIONS

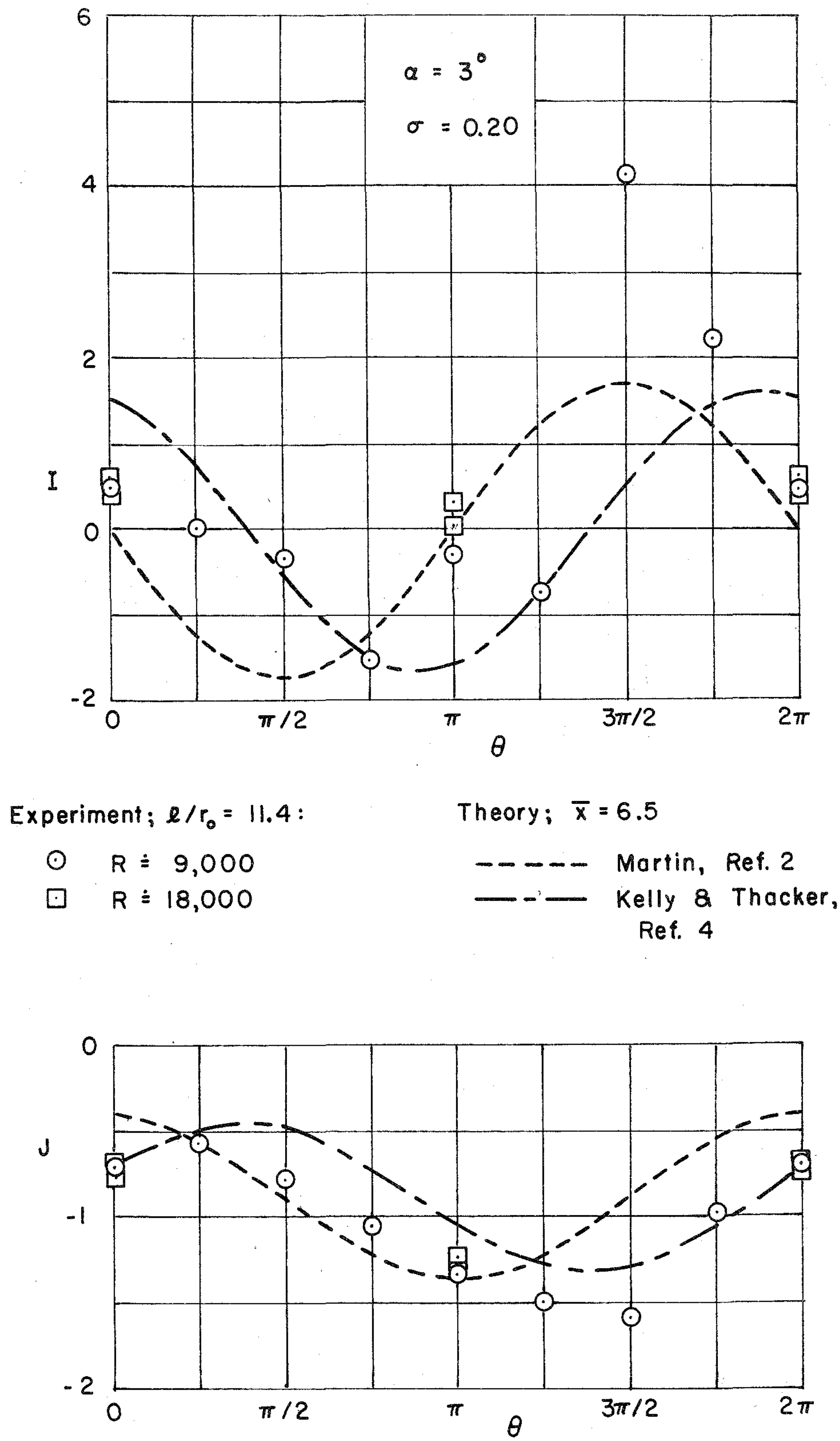

FIGURE 14

EXPERIMENTAL DISTRIBUTIONS OF I AND J AT $\sigma = 0.20$ COMPARED WITH THEORETICAL APPROXIMATIONS

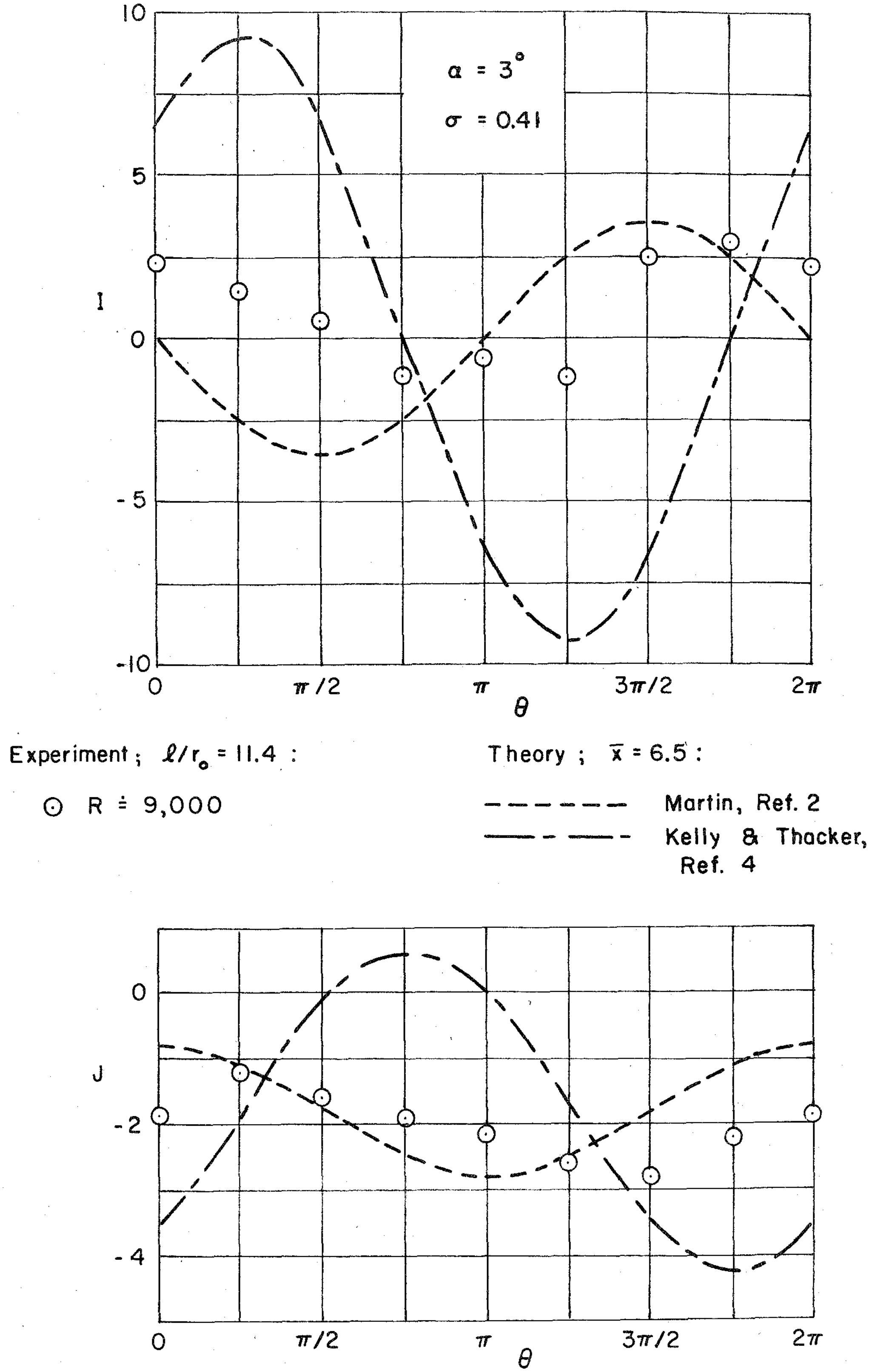

FIGURE 15

EXPERIMENTAL DISTRIBUTIONS OF I AND J AT $\sigma = 0.41$ COMPARED WITH THEORETICAL APPROXIMATIONS

TABLE II. FOURIER COEFFICIENTS

Experimental values (a) from equations 24, using measurements at $\ell / r_o = 11.4$

Theoretical values (b) and (c) respectively from equations 25 and equations 26, using $\overline{x} = 6.5$

	COEFFICIENTS FOR I						COEFFICIENTS FOR J					
	$\alpha = 0^o$	$\alpha = 3^o$					$\alpha = 0^o$	$\alpha = 3^o$				
	A_0	A_0	A_1	B_1	A_2	B_2	C_0	C_0	C_1	D_1	C_2	D_2
	$\sigma = 0.1$	$\sigma = 0.10$					$\sigma = 0.1$	$\sigma = 0.10$				
a) Experiment	0.1	0.03	0.20	-0.86	-0.33	0.15	-0.45	-0.54	0.25	0.09	0	-0.04
b) Martin	0	0	----	-0.86	-----	----	-0.44	-0.44	0.24	----	-	-----
c) Kelly and Thacker	0	0	0.38	-0.72	-----	----	-0.44	-0.44	0.20	0.10	-	-----
	$\sigma = 0.2$	$\sigma = 0.20$					$\sigma = 0.2$	$\sigma = 0.20$				
a) Experiment	0.5	0.50	1.00	-1.66	-0.90	-0.11	-1.00	-1.06	0.34	0.35	0.08	-0.01
b) Martin	0	0	----	-1.73	-----	-----	-0.88	-0.88	0.48	----	----	-----
c) Kelly and Thacker	0	0	1.54	-0.55	-----	-----	-0.88	-0.88	0.16	0.40	----	-----
	$\sigma = 0.4$	$\sigma = 0.41$					$\sigma = 0.4$	$\sigma = 0.41$				
a) Experiment	0.7	0.86	1.94	-0.78	-0.35	-0.44	-2.05	-2.04	0.27	0.60	0.09	0.06
b) Martin	0	0	----	-3.54	-----	-----	-1.75	-1.80	0.98	----	----	----
c) Kelly and Thacker	0	0	6.45	6.60	-----	-----	-1.75	-1.80	-1.79	1.66	----	----

Note: Experimental values for $\alpha = 0^o$ are based on data shown in figure 10.
Experimental values for $\alpha = 3^o$ are based on measurements at eight θ's, $R \doteq 9,000$ (Appendix D).
The σ's shown in table are average values.

for all spin rates.*

The results shown in figures 13, 14, and 15 are described in greater detail by the Fourier coefficients (for $\alpha = 3^{\circ}$) presented in Table II. The coefficients listed in Table II are defined by the Fourier series representations given in Part IV (eqns. 22, 23):

$$I = A_0 + A_1\cos\theta + B_1\sin\theta + A_2\cos 2\theta + B_2\sin 2\theta + \ldots$$

$$J = C_0 + C_1\cos\theta + D_1\sin\theta + C_2\cos 2\theta + D_2\sin 2\theta + \ldots$$

where

$$A_0 = A_0(\bar{x};\alpha,\sigma)$$
$$A_1 = A_1(\bar{x};\alpha,\sigma) \qquad \text{etc.}$$

Table II also includes values of the Fourier coefficients corresponding to the results shown in figure 10 for $\alpha = 0$. For that case ($\alpha = 0$) the boundary layer is axially symmetric, so the Fourier series reduce to:

$$I = A_0(\bar{x};0,\sigma) = [\bar{\delta}_1^*(\bar{x};0,\sigma) - \bar{\delta}_1^*(\bar{x};0,0)]\sqrt{R}$$

$$J = C_0(\bar{x};0,\sigma) = -\sigma[\bar{\delta}_3^*(\bar{x};0,\sigma)]\sqrt{R}$$

since $\bar{u}_e = 1$ and $\bar{w}_e = 0$.

For the case of the yawed body, A_0 and C_0 are equal to the respective average values of I and J around the body at a given axial station and a given spin rate. In contrast to the theoretical results, the experimental values of A_0 given in Table II are non-zero at the

----

*To assume that $\bar{x}$ changes with spin would require changing the method of computation for the theoretical values of I and J (eqns. 16a and 17a). The theoretical results (eqns. 18 through 21) would then contain additional terms involving differences such as

$$[\alpha\bar{x}^{-3/2}(@\ \sigma = 0) - \alpha\bar{x}^{3/2}\ (@\ \text{the given}\ \sigma)]$$

(see eqns. 5 and 7).

higher spin rates ($\sigma \doteq 0.2, 0.4$) for both $\alpha = 0$ and $\alpha = 3^{\circ}$. The experimental values of C_0 given in Table II are slightly lower (algebraically) than the theoretical values (except at $\alpha = 0$, $\sigma = 0.10$). In agreement with theory, however, the experimental values of C_0 are, in general, nearly proportional to spin rate.

From equations 14, 15, 16, and 17 it may be seen that, for any given value of α, $A_0/\overline{u}_e$ represents the change (due to spin) in the circumferential average of $\overline{\delta_1^*}\sqrt{R}$, and $-C_0/\sigma$ represents the change in the circumferential average of $\overline{\delta_3^*}\sqrt{R}$ * (since the circumferential average of $\overline{w}_e$ is zero). For each spin rate shown in Table II the experimental values of A_0 and C_0 at $\alpha = 3^{\circ}$ are roughly equal to their respective values at $\alpha = 0^{\circ}$. Since $\overline{u}_e$ is nearly unity at $\alpha = 3^{\circ}$, these results imply that the effect of spin on the circumferential-average values of δ_1^* and δ_3^* is independent of α, as would be expected from theoretical considerations (see eqns. 48, 49)

The experimental values of B_1 and C_1 show that, at the lower spin rates, the "sin θ" component of the azimuthal distribution of I and the "cos θ" component of the azimuthal distribution of J tend to agree with the theoretical predictions based on Martin's results (ref. 2). At the high spin rate ($\sigma = 0.41$) it appears that the theoretical approximations (which involve the product $\sigma\,\overline{x}$) are no longer valid (also see fig. 15). The values of A_1 and D_1

----

*It follows that $A_0/\overline{u}_e$ may, in fact, be regarded as the change in the circumferential average of $\overline{\Delta^*}\sqrt{R}$ (see eqn. 11a).

in Table II show that the experimental distributions also contain a "cos θ" component in I and a "sin θ" component in J, similar to those introduced by the higher-order terms in Kelly and Thacker's results (ref. 4). At the high spin rate ($\sigma = 0.41$), however, the higher-order theoretical approximation grossly exaggerates the trends displayed by the experimental data.

The experimental values of A_2 and B_2 imply that there are appreciable increments (due to spin) in the "cos 2θ" and "sin 2θ" components of the axial velocity profiles at $\alpha = 3^o$. Such terms do not appear in the theoretical approximations presently available. The experimental values of C_2 and D_2 indicate only small changes in the corresponding Fourier components of the transverse velocity profiles with spin at this angle of yaw. Since the data presented in figures 13, 14, and 15, were obtained at eight different values of θ, additional Fourier coefficients up to B_3, A_4, D_3, and C_4, could be evaluated (see eqns. 24) from those measurements. These higher coefficients, however, would be quite sensitive to data scatter.

5. Magnus Force and Normal Force Due to Spin

The theoretical analysis of the effect of the boundary layer on the outer flow (Part IV, sec. 5) shows that the displacement effect due to the Fourier coefficients B_1 and C_1 will result in a Magnus force, and the effect due to A_1 and D_1 will produce a normal force. Experimental values of B_1 and C_1 are plotted in figure 16, and experimental values of A_1 and D_1 in figure 17, in terms of parameters which provide a generalized comparison with the theoretical approximations (eqns. 25, 26) and permit the inclusion of data from both axial stations ($\ell/r_0 = 11.4$ and 10.2). The values used for

Experiment, $\alpha = 3^\circ$:	●	⊙	⊡	△
k	8	4	4	4
$\bar{x}$	6.5	6.5	6.5	5.3
R	9,000	9,000	18,000	9,000

Unflagged symbols: Laminar B.L.

Flagged symbols: Turbulent B.L.

Laminar B.L. Theory: - - - - Martin, Ref. 2; ——— Kelly & Thacker, Ref. 4.

Magnus Force Coefficient: $C_Y = \frac{2}{\sqrt{R}} \left(C_1 - \frac{\partial B_1}{\partial \bar{x}} \right)$ (39)

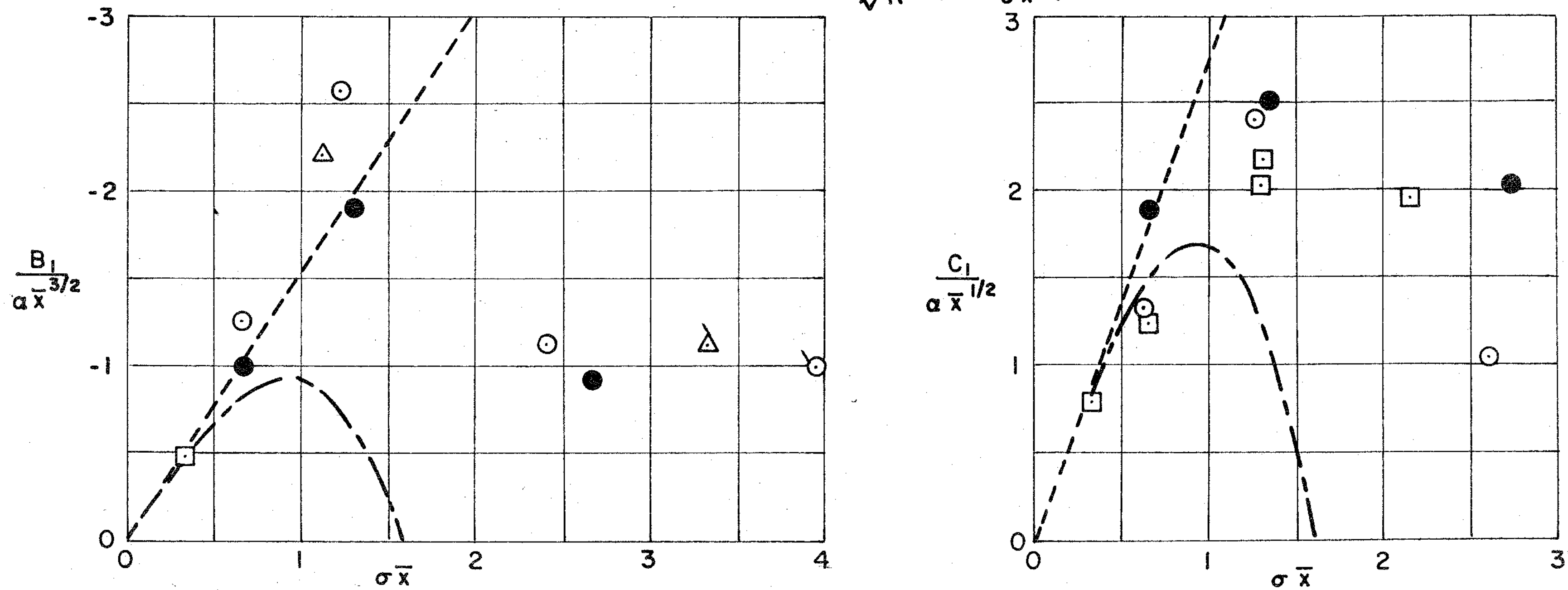

FIGURE 16

EFFECT OF SPIN ON THE FOURIER COEFFICIENTS WHICH GIVE MAGNUS FORCE

Experiment, $\alpha = 3^{\circ}$:	●	⊙	⊡	△
k	8	4	4	4
$\bar{x}$	6.5	6.5	6.5	5.3
R	9,000	9,000	18,000	9,000

Unflagged symbols: Laminar B.L.

Flagged symbols: Turbulent B. L.

Laminar B. L. Theory: — — — Kelly & Thacker, Ref. 4.

Incremental Normal Force Coefficient: $\Delta C_N = \frac{2}{\sqrt{R}} \left(\frac{\partial A_1}{\partial \bar{x}} + D_1 \right)$ (42)

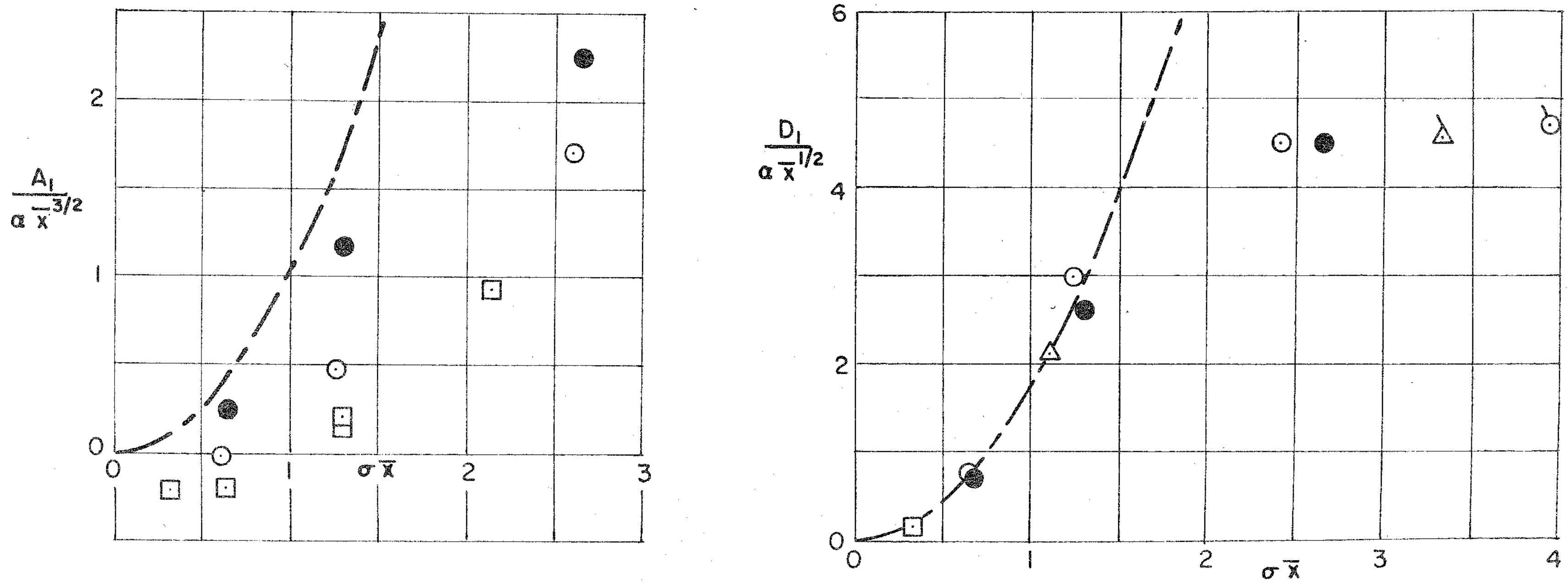

FIGURE 17

EFFECT OF SPIN ON THE FOURIER COEFFICIENTS WHICH GIVE NORMAL FORCE

$\overline{x}$ in these parameters are the values that were obtained by the profile fitting in the zero-spin, zero-yaw case discussed earlier. As before, it is assumed that $\overline{x}$ does not vary with spin.* The bold (solid) symbols (k = 8) in figures 16 and 17 correspond to the values of the Fourier coefficients given in Table II, which are based on boundary-layer velocity profiles obtained at eight azimuthal positions around the body at the axial station $\ell/r_0 = 11.4$ The open symbols (k = 4) represent values based on data obtained at only four azimuthal positions.

In the Fourier analysis explained in Part IV (eqns. 24) the measurements at $\theta = 0, \pi$ have no influence on the evaluation of the "sin θ" coefficients B_1 and D_1, and the measurements at $\theta = \pi/2$, $3\pi/2$ have no influence on the evaluation of the "cos θ" coefficients A_1 and C_1. Consequently, each open symbol (k = 4) in figures 16 and 17 is actually based on only two velocity profiles.† Each bold symbol (k = 8), on the other hand, is based on six velocity profiles. Values represented by the three bold symbols in each plot may, therefore, be regarded as more reliable than those represented by the open symbols.

The experimental values of B_1 and C_1 (fig. 16) at the lower spin rates ($\sigma\overline{x} < 1.5$ in the case of B_1; $\sigma\overline{x} < 0.8$ in the case of C_1) agree closely with the linear approximation based on Martin's

----

*See footnote, p. 57.

†Since there were some variations in spin rate from run to run at a given nominal spin rate (see Appendix E Run Schedule), the data points in figures 16 and 17 are plotted at the averages of the spin rates for the particular runs used in computing each point.

theoretical results (ref. 2), for the values of $\overline{x}$ used here. At higher spin rates the experimental values of B_1 and C_1 fall between the linear approximation and the higher-order approximation based on the theoretical results of Kelly and Thacker (ref. 4). It is apparent in each of the plots in figure 16 that a curve through the experimental data (for the laminar boundary layer) from $\sigma \overline{x} = 0$ to $\sigma \overline{x} = 3$ could have a geometric shape much like the shape of the theoretical curve based on reference 4. As explained in Part IV, the derivatives $\partial B_1 / \partial \overline{x}$ required for computing Magnus force (see eqn. 39), cannot be determined from the present measurements. It is reasonable to expect, however, that numerical values of $\partial B_1 / \partial \overline{x}$ will have the same sign as numerical values of B_1; therefore, we can conclude from figure 16 that the boundary-layer displacement effect measured in the present experiments will produce a Magnus force in the positive direction (see sketch p. 31) when the body is at a positive yaw angle of 3°.

For $\sigma \overline{x} < 1.5$ the experimental values of A_1 (fig. 17) for $k = 8$ are only slightly lower than the theoretical curve based on the results of Kelly and Thacker (ref. 4),* and the experimental values of D_1 agree very well with the theoretical approximation (for the values of $\overline{x}$ used here). At higher spin rates the experimental values of A_1 and D_1 apparently continue to increase with spin, but not as fast as the theoretical results would predict. From figure 17 we can conclude that the boundary-layer displacement effect observed on the spinning model at $\alpha = 3^{\circ}$ will give a

----

*Martin's approximation (ref. 2, linear in $\sigma \overline{x}$) does not include terms which would give a normal force increment due to spin.

positive normal force increment (see sketch p. 31), assuming that $\partial A_1 / \partial \bar{x}$ has the same sign as A_1 (see eqn. 42).

VI. CONCLUSIONS

Results of particular significance in this investigation of the three-dimensional, laminar, boundary-layer flow on a spinning slender body are summarized below.

a) Boundary-layer measurements, at zero incidence and also at an angle of incidence of 3 degrees, indicate that spinning of the model increased the average displacement thickness around the circumference at a given axial distance from the nose. This effect of spin is not predicted by any of the presently available theoretical analyses.

b) At low spin rates the experimental evaluations of the boundary-layer asymmetries which contribute to the Magnus force on the yawed body agree with Martin's theoretical approximation (ref. 2). This result implies that the "Magnus force due to displacement thickness" is positive in direction and increases linearly with spin rate, when the product of spin rate times body length is small.

c) At higher spin rates, the asymmetries mentioned in (b), above, exhibit experimentally the same type of non-linearity with spin as do the higher-order theoretical approximations of Kelly and Thacker (ref. 4). In contrast to those theoretical results, however, the spin rate is reasonably high at which this non-linearity becomes significant.

d) Experimental values of boundary-layer asymmetries which contribute to the normal force on the yawed, spinning model at low spin rates agree with theoretical approximations based on the results of reference 4. At high spin rates the experimental values increase less rapidly than the theoretical values.

REFERENCES

1. Mager, A.,

   (a) Laminar Boundary Layer Problems Associated with Flow Through Turbomachines, Doctoral Thesis, California Institute of Technology (1953).

   (b) Three-Dimensional Laminar Boundary Layer with Small Cross-Flow, Journal of the Aeronautical Sciences, Vol. 21, No. 12, pp. 835-845, (December 1954).

   (c) Incompressible Non-Meridional Boundary Layer Flow on Bodies of Revolution, NAVORD Report 3366, NOTS 942 (September 1954).

2. Martin, J. C.,

   On Magnus Effects Caused by the Boundary Layer Displacement Thickness on Bodies of Revolution at Small Angles of Attack,

   (a) BRL Report 870 (Revised), Aberdeen Proving Ground, Md., (June 1955).

   (b) Journal of the Aeronautical Sciences, Vol. 24, No. 6, pp. 421-429 (June 1957).

3. Kelly, H. R., An Analytical Method for Predicting the Magnus Forces and Moments on Spinning Projectiles, NOTS TM 1634, USNOTS, China Lake, Calif. (June 1954).

   Note: Tables of numerical values for the boundary layer velocity profile functions derived by Kelly are contained in the following report:

   Gates, Arms, and Gleissner, The Numerical Integration of a Set of Equations from Magnus Force Theory, NPG Report 1457, USNPG, Dahlgren, Va. (May 1956).

4. Kelly, H. R., and Thacker, G. R., The Effect of High Spin on the Magnus Force on a Cylinder at Small Angles of Attack,* NAVORD Report 5036, NOTS 1381 (February 1956).

5. Private correspondence from Mr. Nathan Gerber, Ballistic Research Laboratories, Aberdeen Proving Ground, Md. (February and March 1957).

6. Sedney, R., Laminar Boundary Layer on a Spinning Cone at Small Angles of Attack,

   (a) BRL Report 991, Aberdeen Proving Ground, Md. (September 1956).

   (b) Journal of the Aeronautical Sciences, Vol. 24, No. 6, pp. 430-455 (June 1957).

7. Fiebig, M., Laminar Boundary Layer on a Spinning Cone at a Small Angle of Attack,

   Part I, AF OSR TN56-532 (June 1956).

   Part II, AF OSR TN 57-68 (February 1957).

   Cornell University, Ithaca, N. Y.

8. Rott, N., and Smith, W. E., Some Examples of Laminar Boundary Layer Flow on Rotating Blades, Journal of the Aeronautical Sciences, Vol. 23, No. 11, pp. 991-997 (November 1956).

----

*See note following this List of References.

9. Squire, L. C., The Three Dimensional Boundary Layer Equations and Some Power Series Solutions, British ARC, R and M 3006 (October 1955).

10. Buford, W.E., Magnus Effect in the Case of Rotating Cylinders and Shell, BRL MR 821, Aberdeen Proving Ground, Md. (July 1954).

11. Van Aken, R. W., and Kelly, H. R., The Magnus Force on Spinning Cylinders, Institute of the Aeronautical Sciences, Preprint 712 (January 1957).

12. Larsen, H. C., Design of a Model for the Measurement of the Pressure Distribution on an Axially-Symmetric Rotating Body, A.E. Thesis, California Institute of Technology (1955).

13. Fehrman, A. L., Effect of Spin and Yaw on Boundary Layer Transition Along a Body of Revolution, A. E. Thesis, California Institute of Technology (1955).

14. Taylor, G. I., Stability of a Viscous Liquid Contained Between Two Rotating Cylinders, Philosophic Transactions of the Royal Society of London, Series A, Vol. 223, pp. 289-343 (1923). Abstracted in Proceedings, Series A, Vol. 102, No. 718, pp. 541-542 (February 1923).

15. Lewis, J. W., An Experimental Study of the Motion of a Viscous Liquid Contained Between Two Coaxial Cylinders, Proceedings of the Royal Society of London, Series A, Vol. 117, No. 777, pp. 388-407 (January 1928).

16. Moore, F. K., Displacement Effect of a Three Dimensional Boundary Layer, NACA Report 1124 (1953); also TN 2722 (1952).

17. Dunn, E. L., and Kelly, H. R., The Displacement Effect of a Three Dimensional Boundary Layer of Moderate Thickness, NOTS TM 1615, USNOTS, China Lake, Calif. (June 1954).

----

*Note concerning reference 4:
In the course of the present research it was found that the numerical values listed in NAVORD 5036 for the profile functions q_o and t_o (corresponding to f_3 and f_4 in the present report) are in error. Mr. Kelly has indicated that he intends to issue a correction notice to the distribution of that NAVORD. The numerical values (for the corresponding functions) listed in BRL 870-Revised (ref. 2) and also in NPG Report 1457 (ref. 3) are the correct values.

APPENDIX A

HOT WIRE SYSTEM

1. Early Studies

In the process of developing a suitable hot wire anemometer for these three-dimensional boundary-layer flow measurements, two methods for using a pivoting probe with a simple, straight hot wire were investigated before the V-shaped hot wire (see Part II) was adopted. In one of the schemes tested, the hot wire was operated at constant resistance and the flow direction was to be determined by orienting the straight wire to the minimum-current position (corresponding to flow parallel to the wire). The primary disadvantage of that system was the inconvenience involved in the detection of minimum required current, since the value of the current depends on the unknown flow speed as well as on the direction of the wire. The current readings, furthermore, indicated false minima due, presumably, to the wake from the leading support needle. The other method for using the straight hot wire was equivalent to using an x type wire on a fixed probe except that a single wire was used and readings of that wire were required for two orientations differing by a given angle (60° was used for the tests conducted). Such a system was found to be unsatisfactory because of the excessive amount of calibration data needed to accommodate the wide range of flow directions involved. The drawbacks of both straight-wire techniques were overcome by using a V-shaped wire on the pivoting probe as described in Part II.

2. V-shaped Hot Wire Operating Procedure

The V-shaped hot wire was connected into a dual Wheatstone bridge circuit as shown in figure A1. Using this bridge arrangement and operating the hot wire at constant resistance provided a procedure in which both air speed and direction could be determined by null-seeking methods, as follows:

1) The hot wire was operated at a constant resistance R_w corresponding to constant wire temperature (T_w) of approximately 75 degrees centigrade. To maintain a constant value of R_w the decade box was set to the proper resistance and the heating current was regulated to obtain a null reading on galvanometer G_2.

2) The V-shaped hot wire was oriented into the flow direction by pivoting the probe to a position at which the resistances R_1 and R_2 of the two sides of the V were balanced against each other as indicated by a null reading on galvanometer G_1.

3) With G_1 and G_2 both at null, the flow direction was determined from the counter reading on the probe actuator and the flow speed was determined from hot wire current and tunnel air temperature by use of a calibration chart.

The current was measured by using a precision potentiometer to measure the voltage drop across a 1 ohm resistor in series with the hot wire. Tunnel air temperature was measured by a mercury thermometer inserted through the tunnel wall.

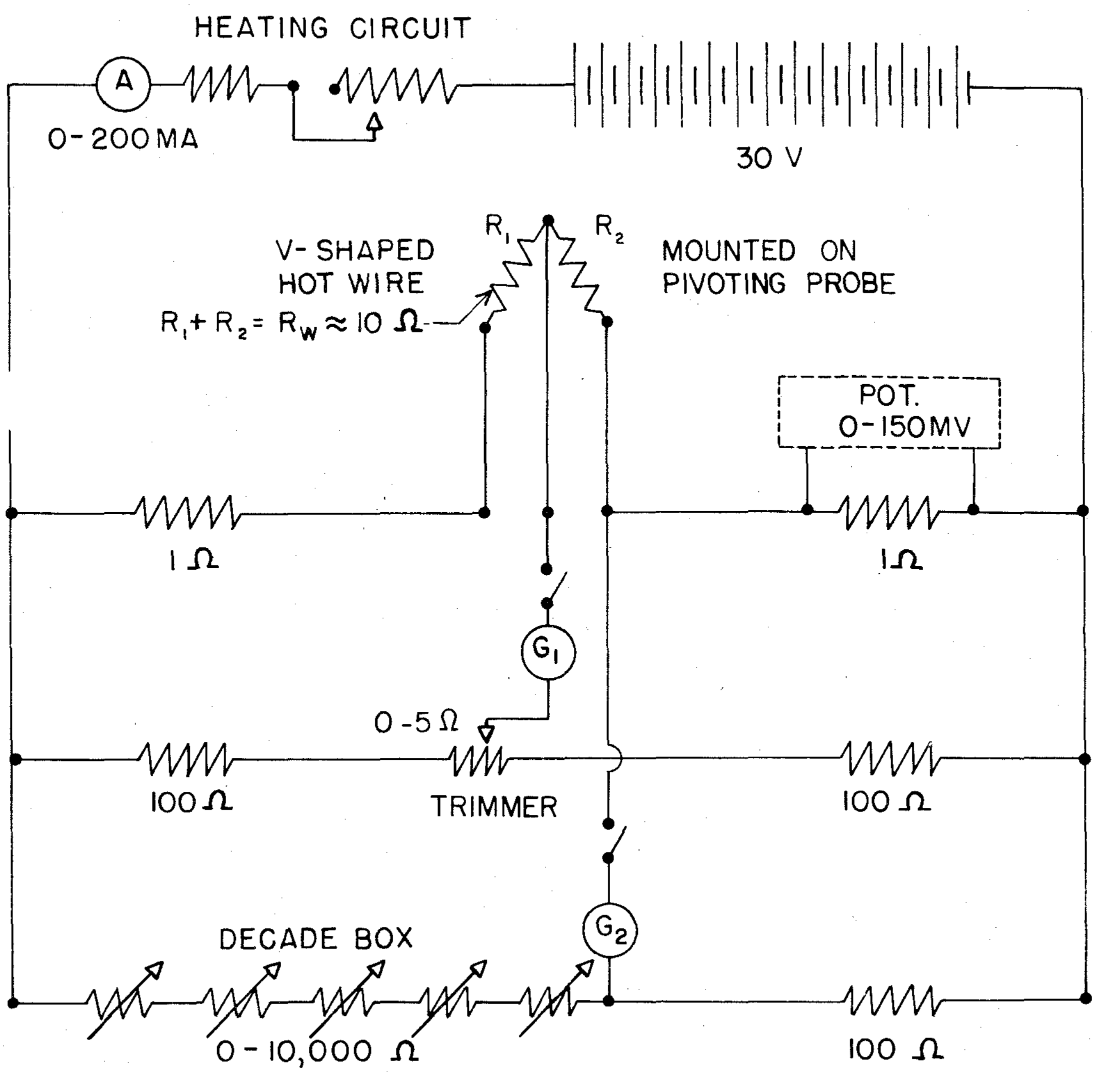

FIGURE A1
WHEATSTONE BRIDGE CIRCUIT FOR DIRECTIONALLY-SENSITIVE HOT WIRE ANEMOMETER.

In the procedure outlined above, the following two equations are satisfied simultaneously:

$$R_1 + R_2 + K_1 = \text{constant} \tag{A1}$$

$$\frac{R_1 + K_1}{R_2 + K_2} = 1 + \varepsilon \quad = \text{constant} \tag{A2}$$

The constants K_1 and K_2 represent the 1 ohm resistors (fig. A1) plus about 0.05 ohms due to lead resistance, on either side of the hot wire. The resistance at which the hot wire was operated for the present measurements was such that R_1 and R_2 were approximately six times as large as K_1 and K_2. The factor ε accounts for a slight difference in the electrical lengths of the two legs R_1 and R_2 of the hot wire and also for a small difference between K_1 and K_2.

The ratio of resistances (eqn. A2) was found to be extremely sensitive (within $\pm \frac{1}{2}$ degree) to flow direction, while the overall resistance (eqn. A1) was relatively insensitive to direction. Consequently, the iteration involving current regulation and probe orientation converged rapidly.

3. V-shaped Hot Wire Calibration Procedures

Prior to calibration and operation of a given hot wire, the bridge ratio of the direction sensing portion of the bridge circuit was adjusted to the proper value, as follows:

a) A glass test tube was placed over the probe so that there was no air flow over the hot wire.

b) Sufficient current was passed through the hot wire to heat it to the chosen operating temperature.

c) The trimming resistor in the direction bridge (see fig. A1) was then adjusted to give a null reading on G_1. To obtain the required sensitivity of adjustment, the trimmer, which is shown schematically as a single variable resistor, was constructed of a ten turn, 0-25 ohm Helipot shunted by a 10 ohm resistor on either side of the center tap.

To calibrate the hot wire for air speed measurement the model was removed from the sting, and a 1/4 inch diameter standard pitot-static pressure probe was installed in the tunnel approximately 2 inches from the hot wire. Although the hot wire was operated at constant temperature (T_w) for the velocity measurements, it was necessary to perform the calibration at several hot-wire temperatures (T_w) in order to correct for variations in the temperature-loading factor $(T_w - T_a)/T_a$ due to day-to-day variations in tunnel air temperature (T_a). Results of a typical calibration test are shown in figs. A3 and A4. The hot wire was positioned to "null orientation" for each calibration measurement.

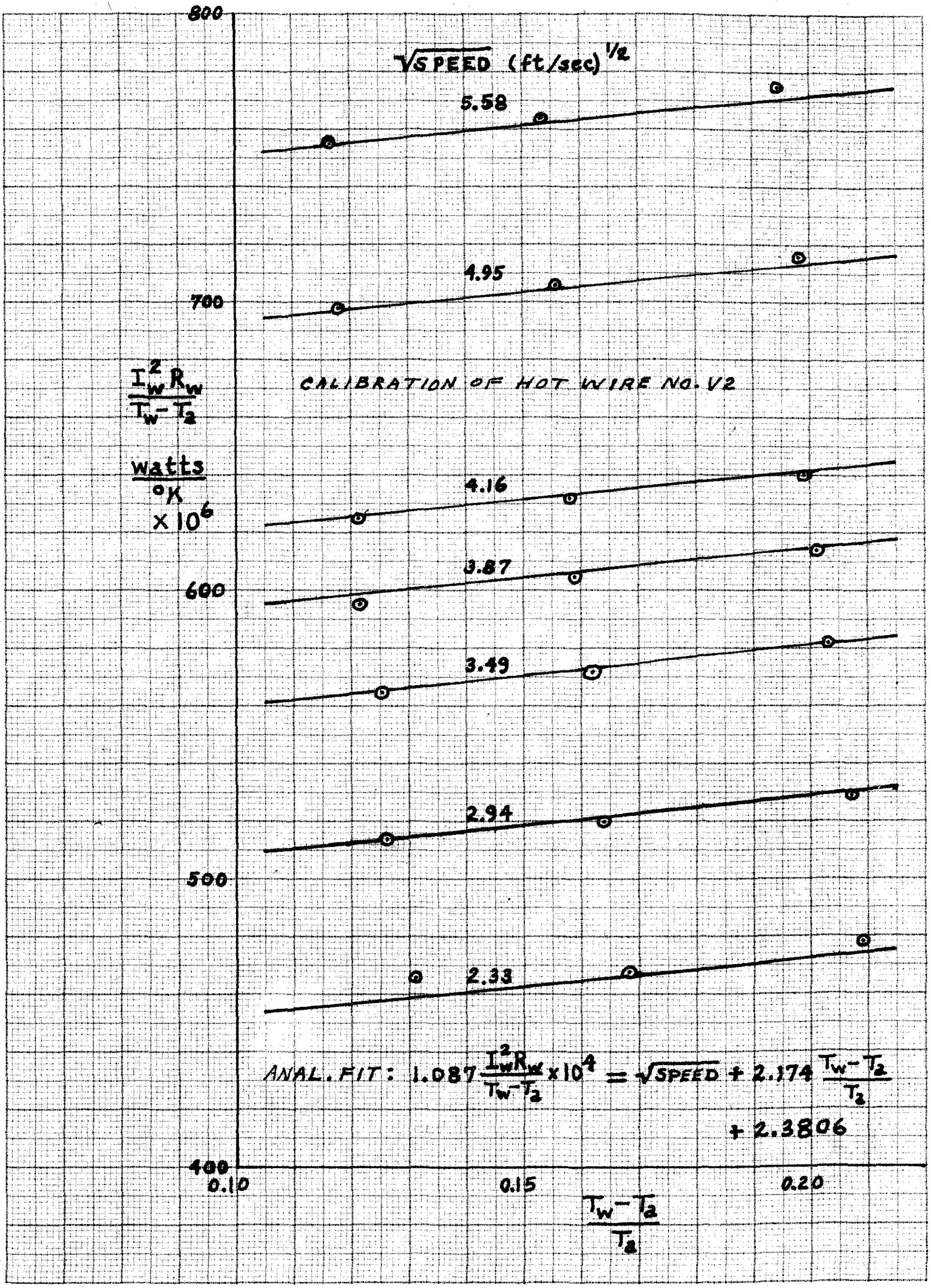

FIGURE A2
TEMPERATURE LOADING EFFECT ON HOT WIRE
AIR SPEED CALIBRATION

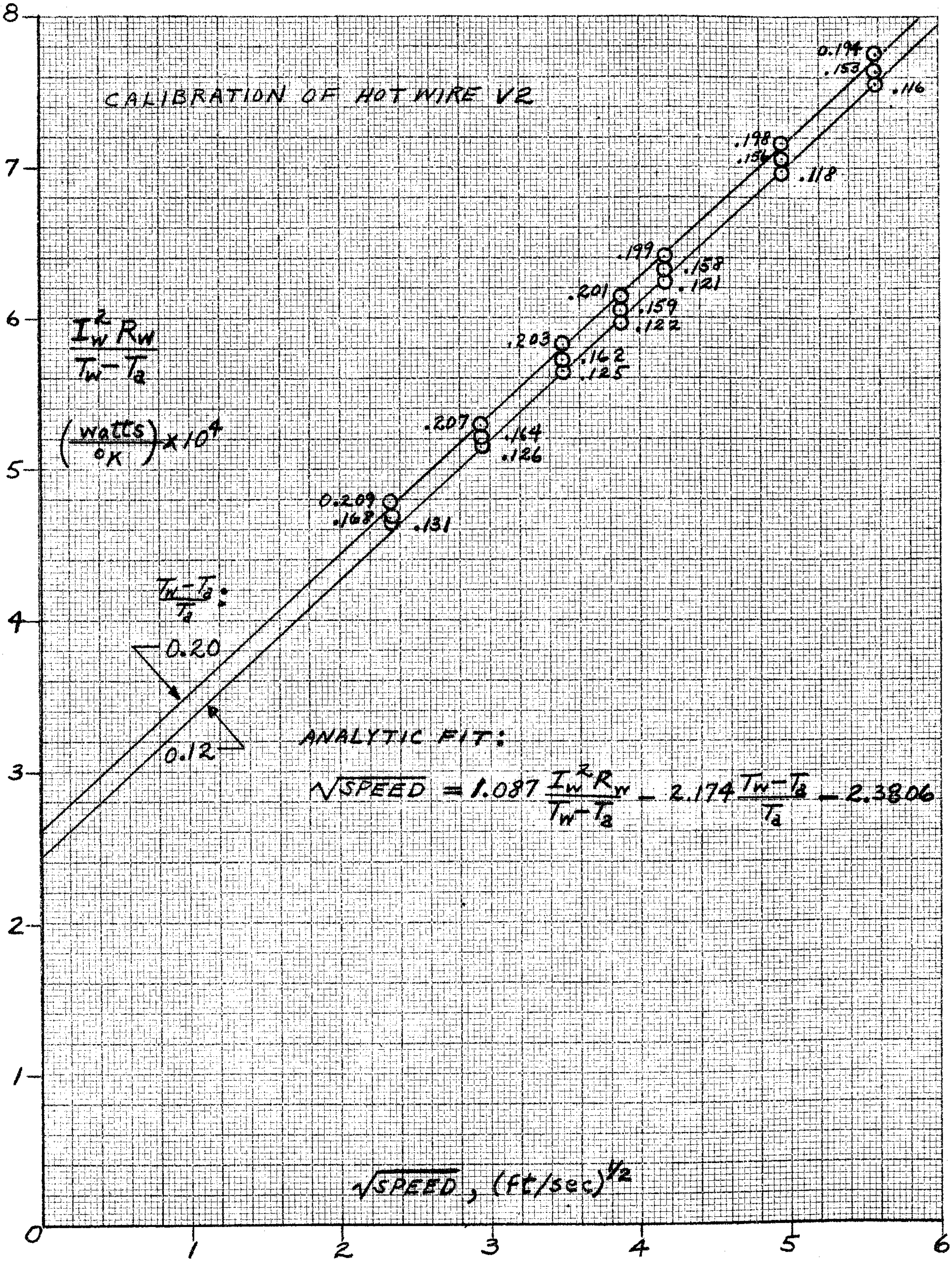

FIGURE A3
HOT WIRE AIR SPEED CALIBRATION CHART

APPENDIX B

COMPARISON OF HOT-WIRE DATA WITH PERPENDICULAR AND SWEPT-BACK PROBES

2 figures

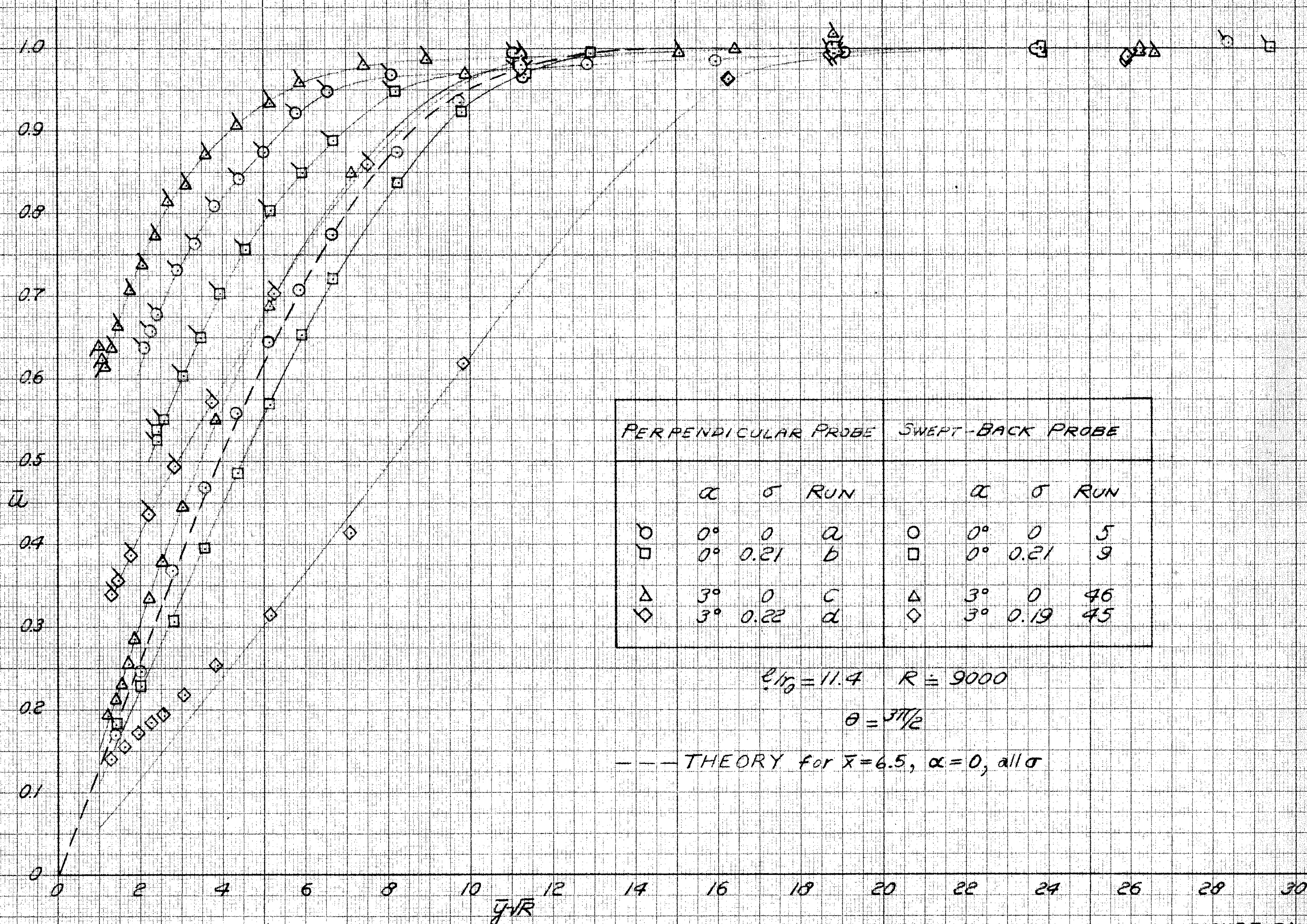

FIGURE B1

FIGURE B1

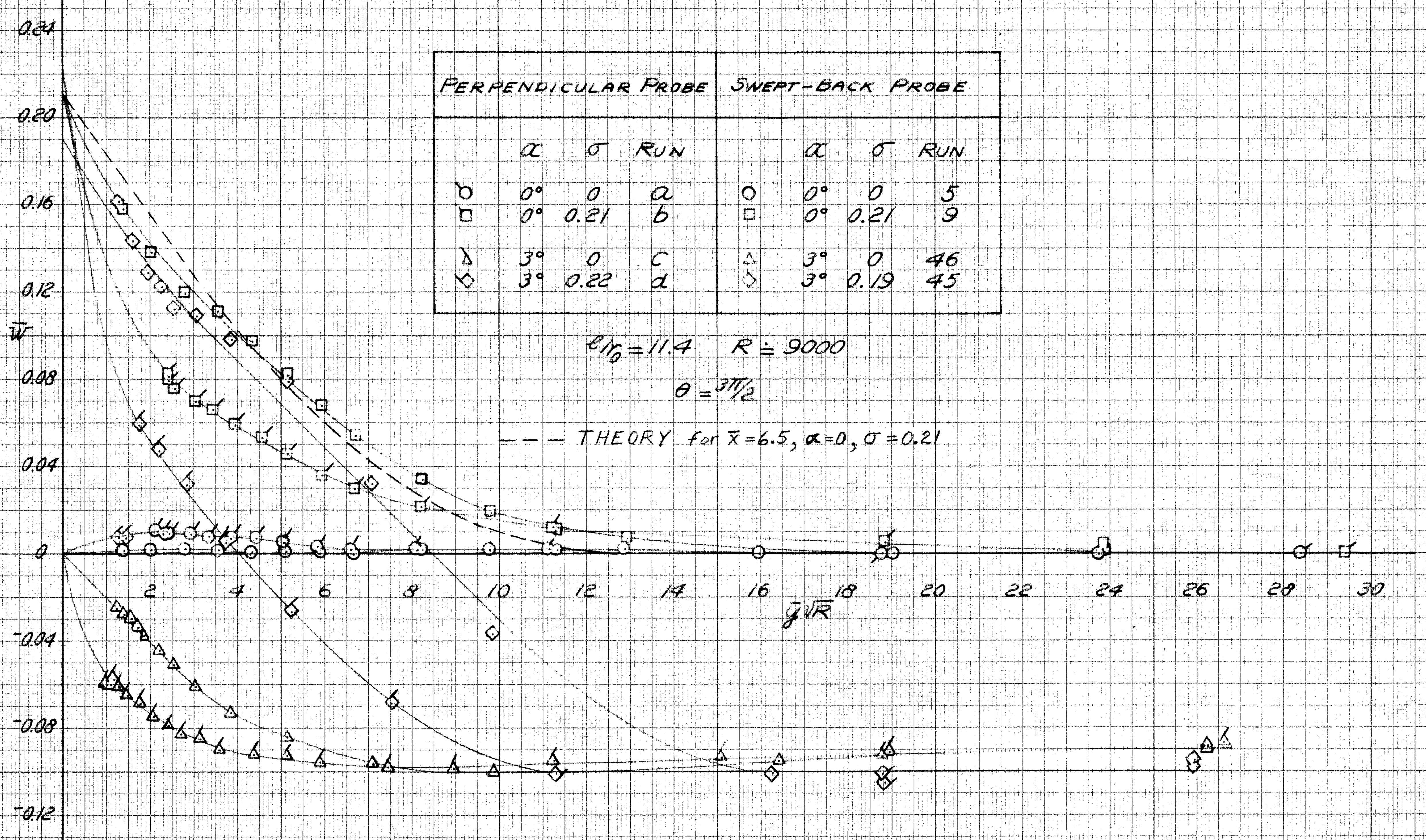

FIGURE B2

FIGURE B2

APPENDIX C

VELOCITY PROFILES AT ZERO YAW

10 figures

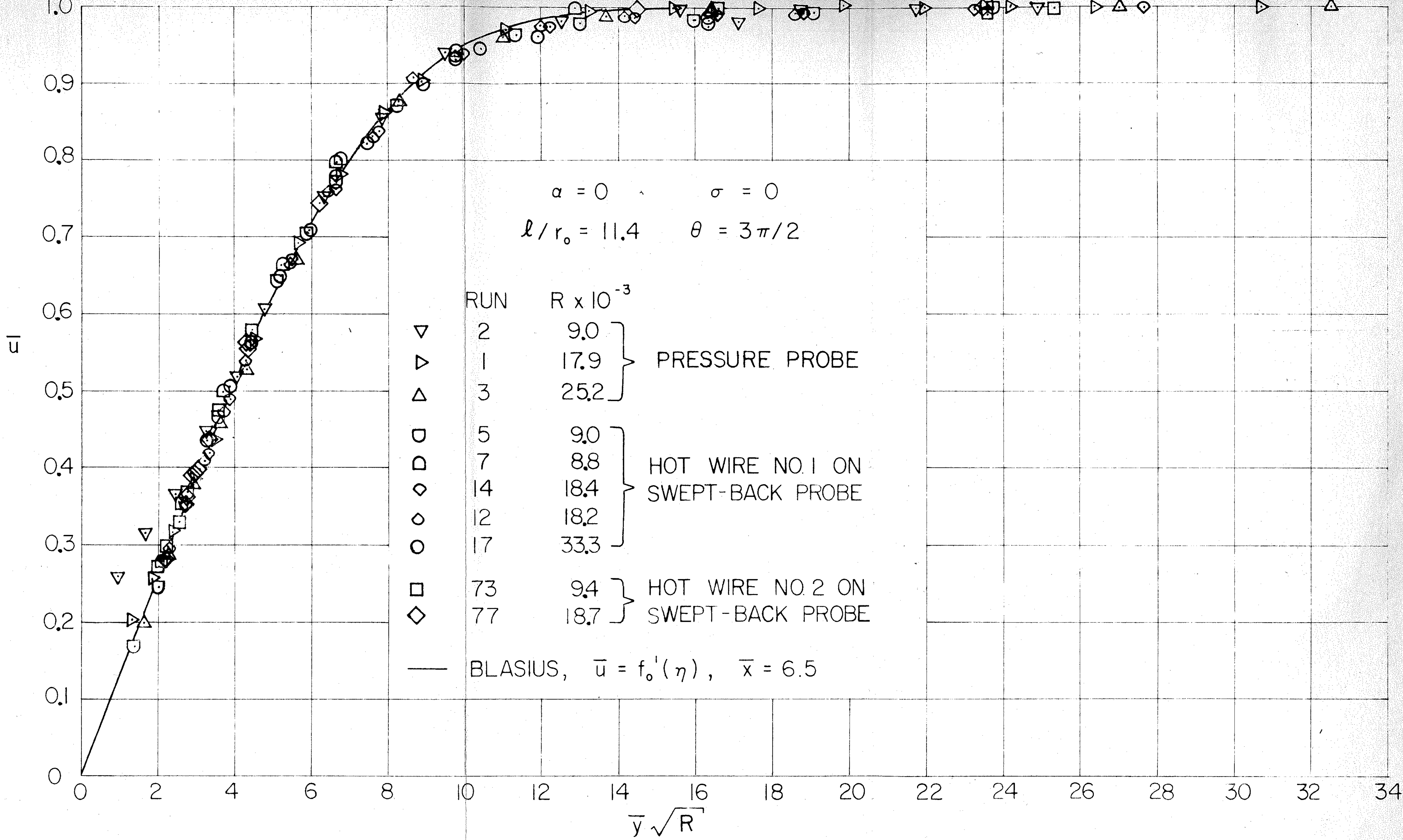

FIGURE C1

FIGURE C1

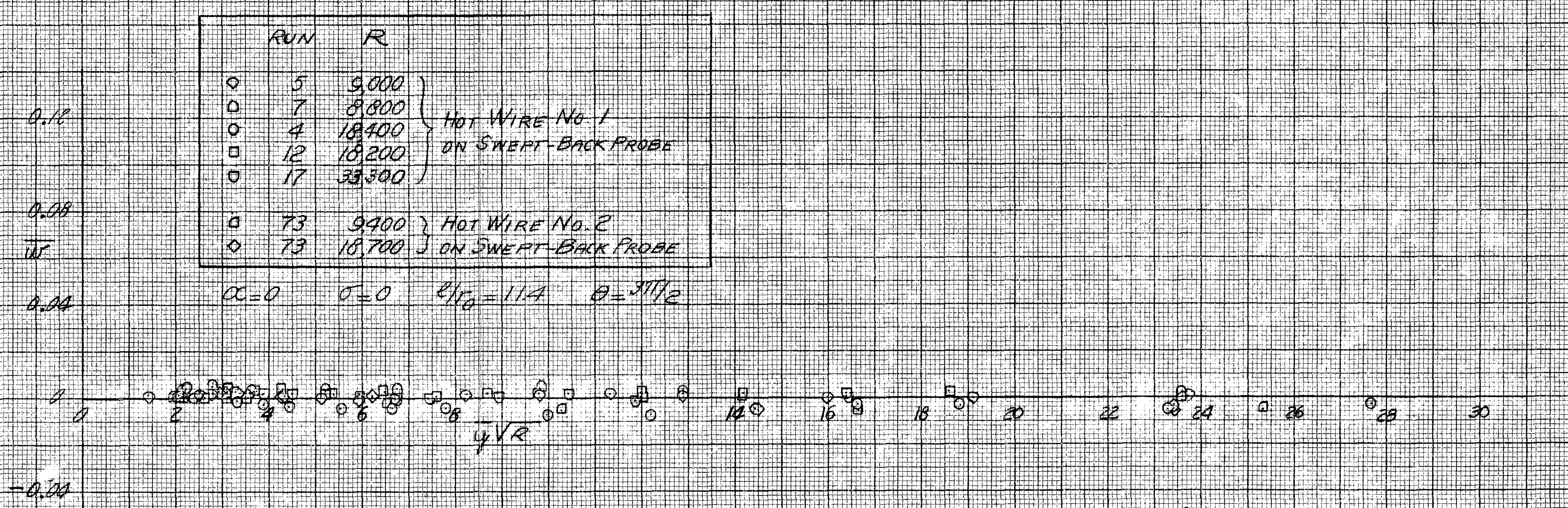

FIGURE C2

FIGURE C2

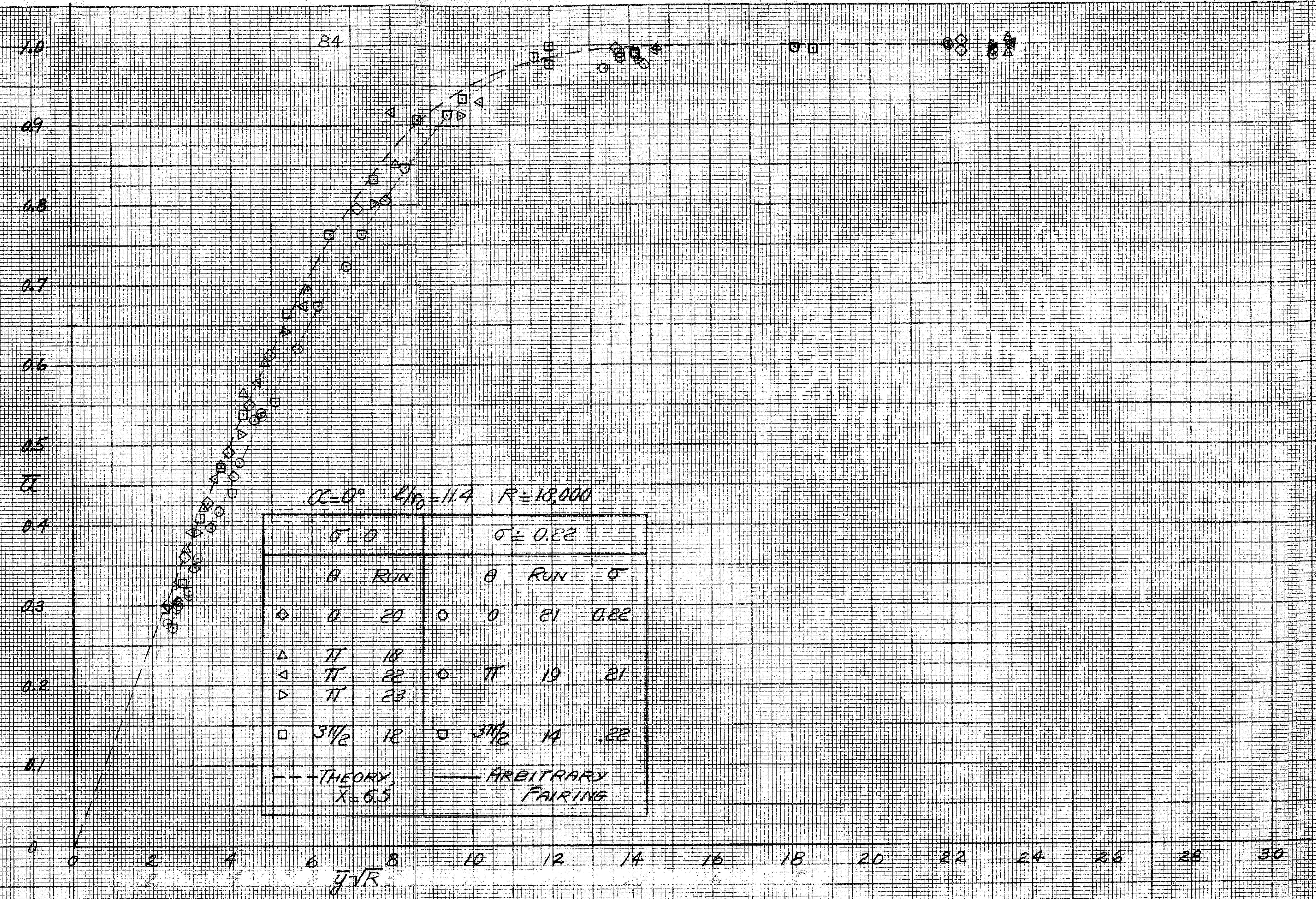

FIGURE C3

FIGURE C3

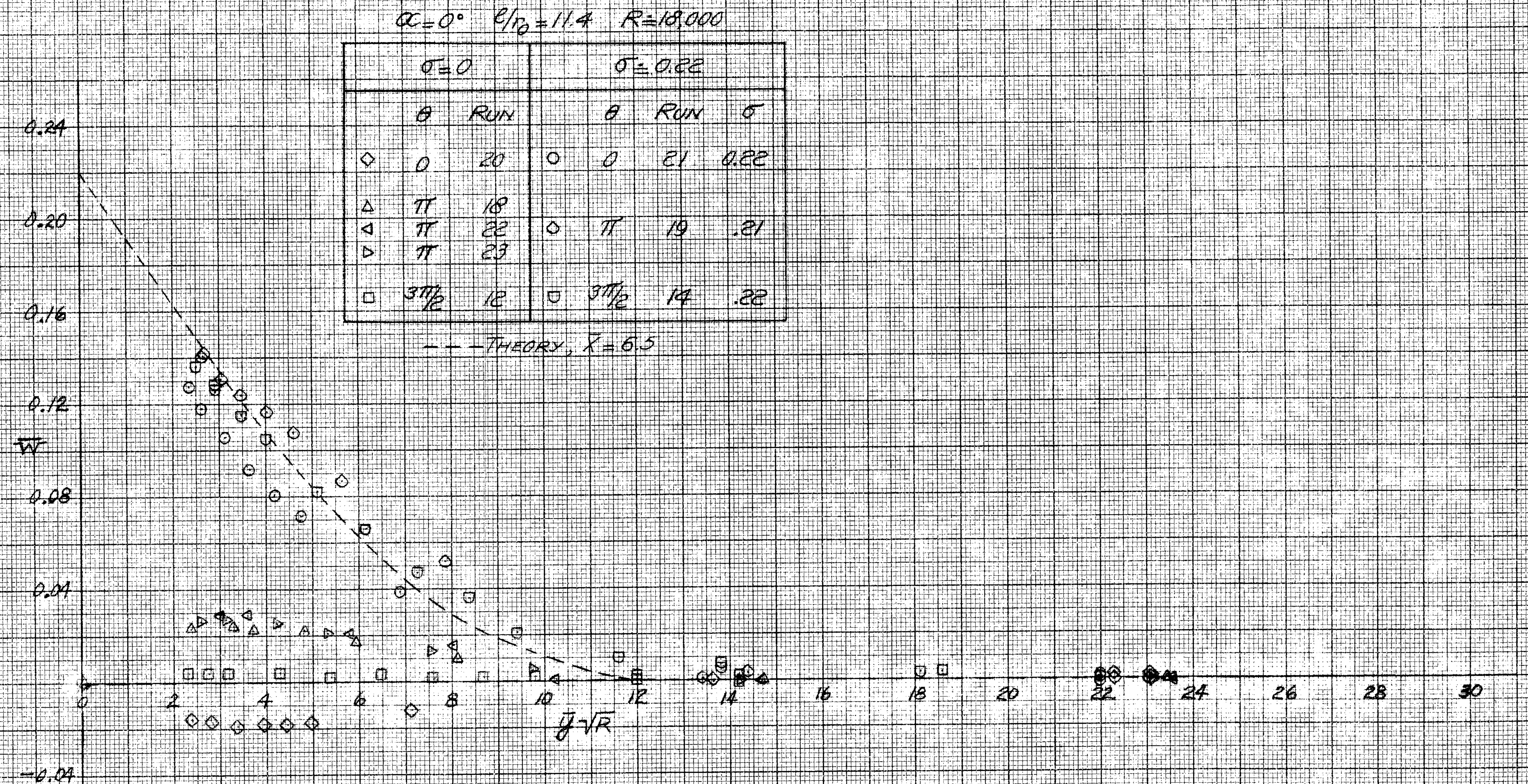

FIGURE C4

FIGURE C4

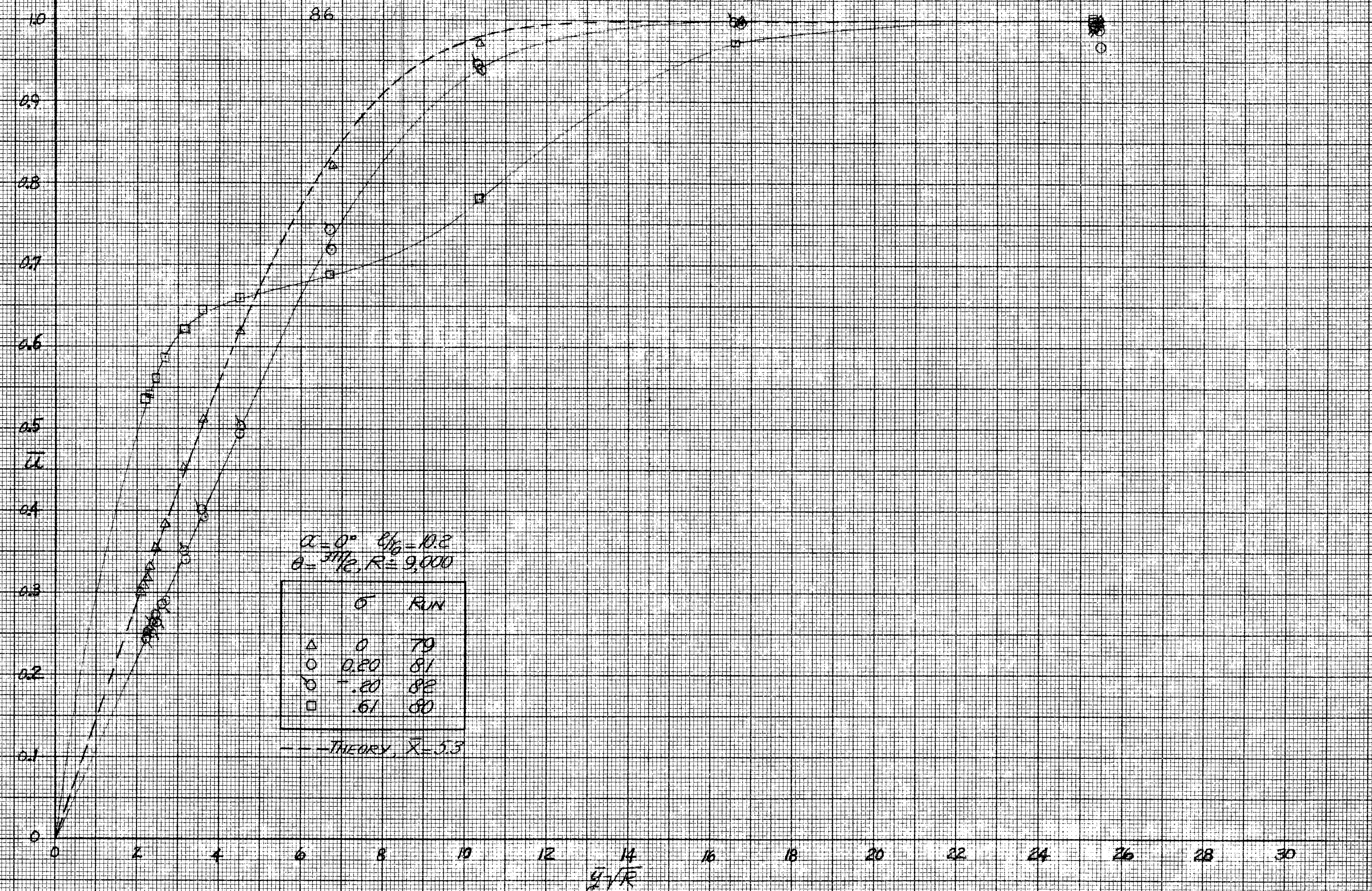

FIGURE C5

FIGURE C5

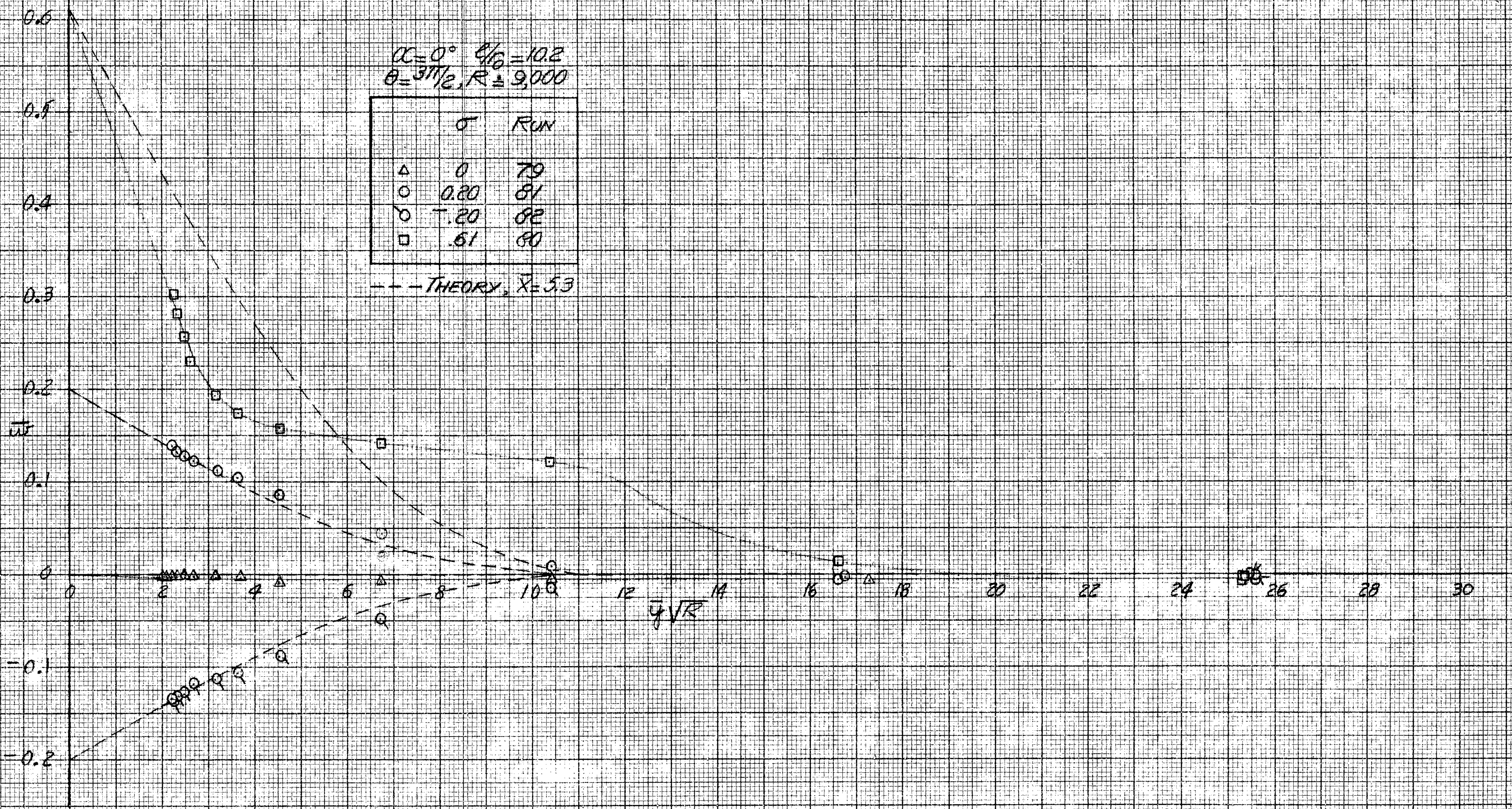

FIGURE C6

FIGURE C6

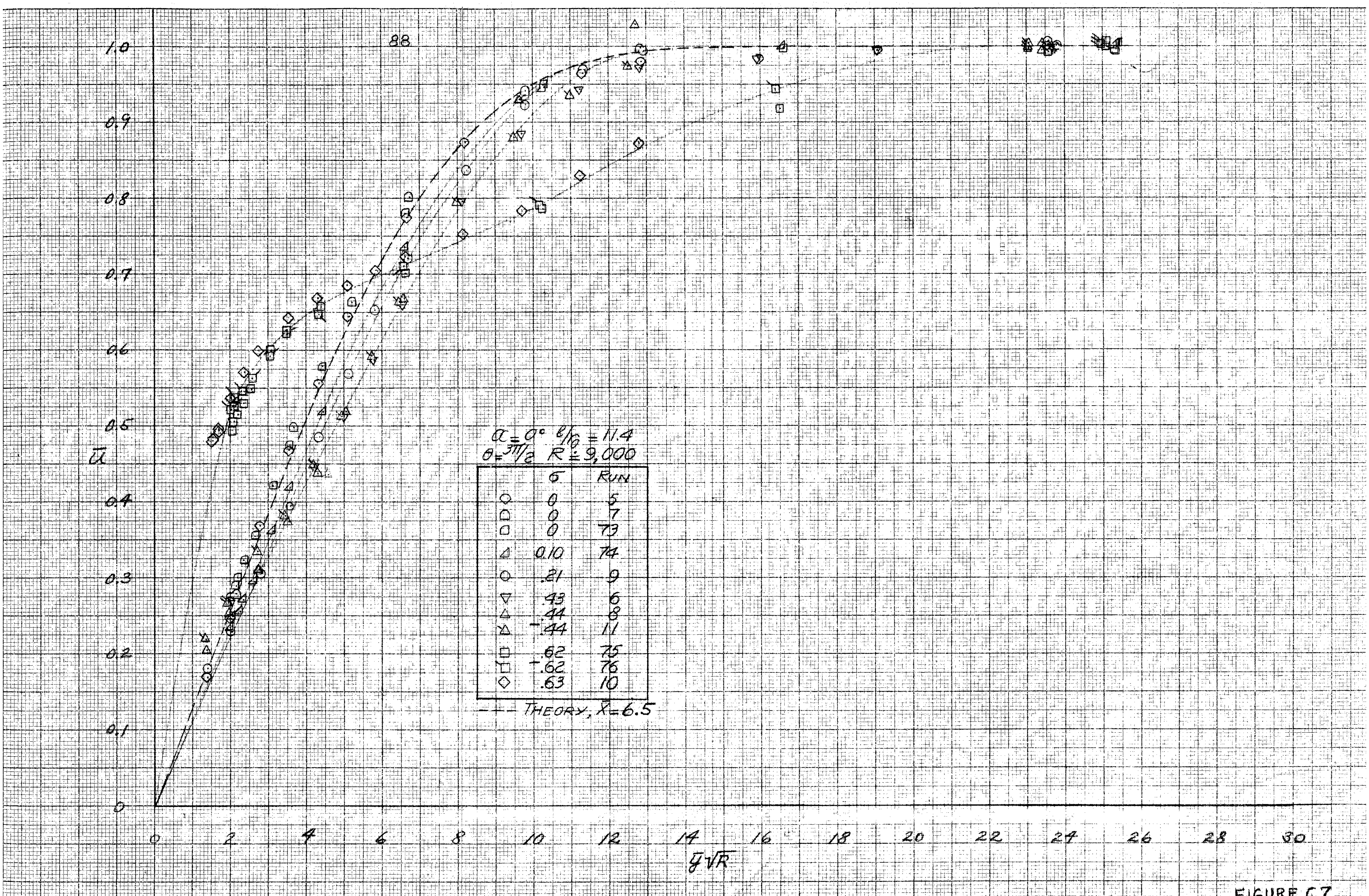

FIGURE C7

FIGURE C7

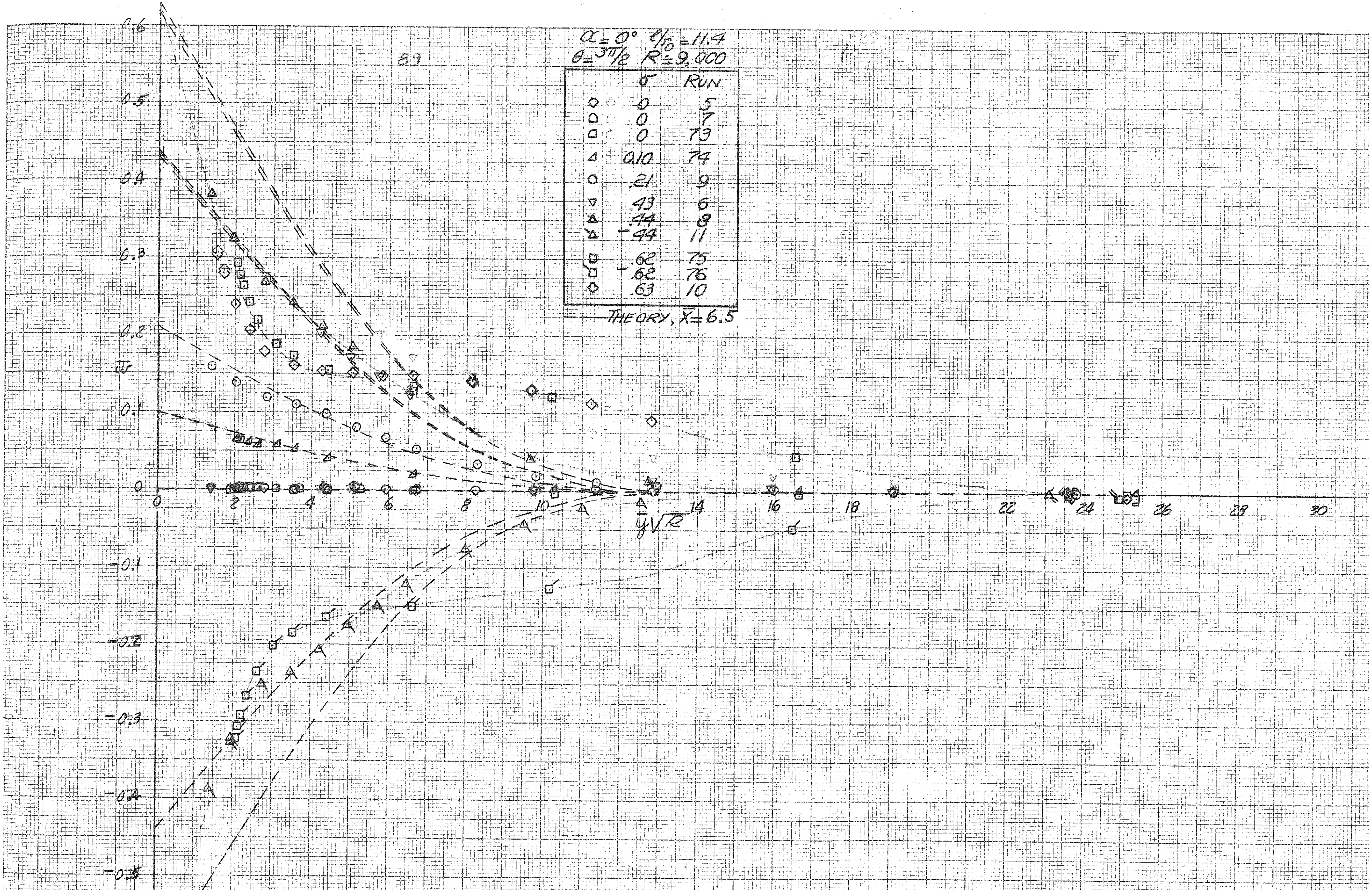

FIGURE C8

FIGURE C8

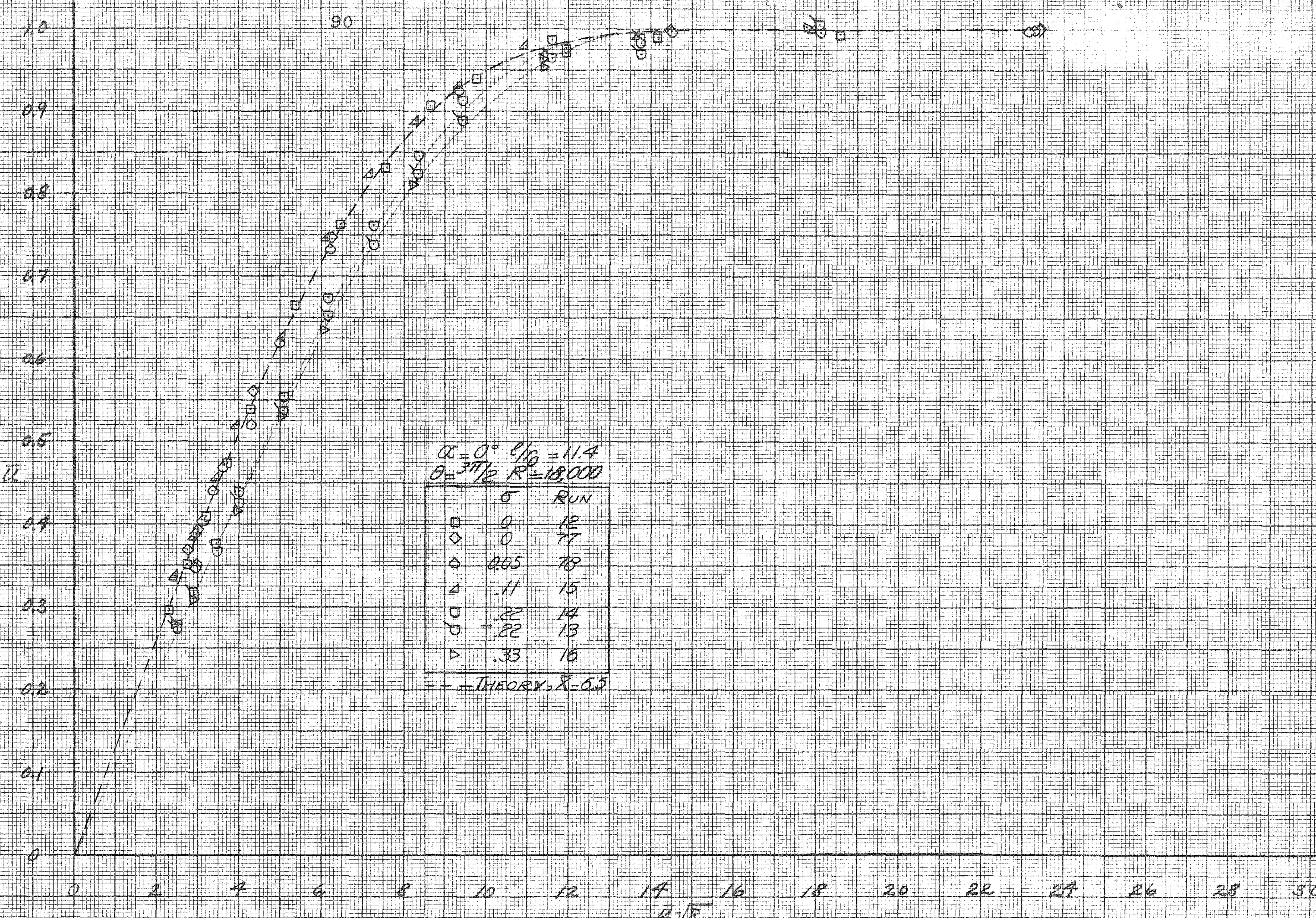

FIGURE C9

FIGURE C9

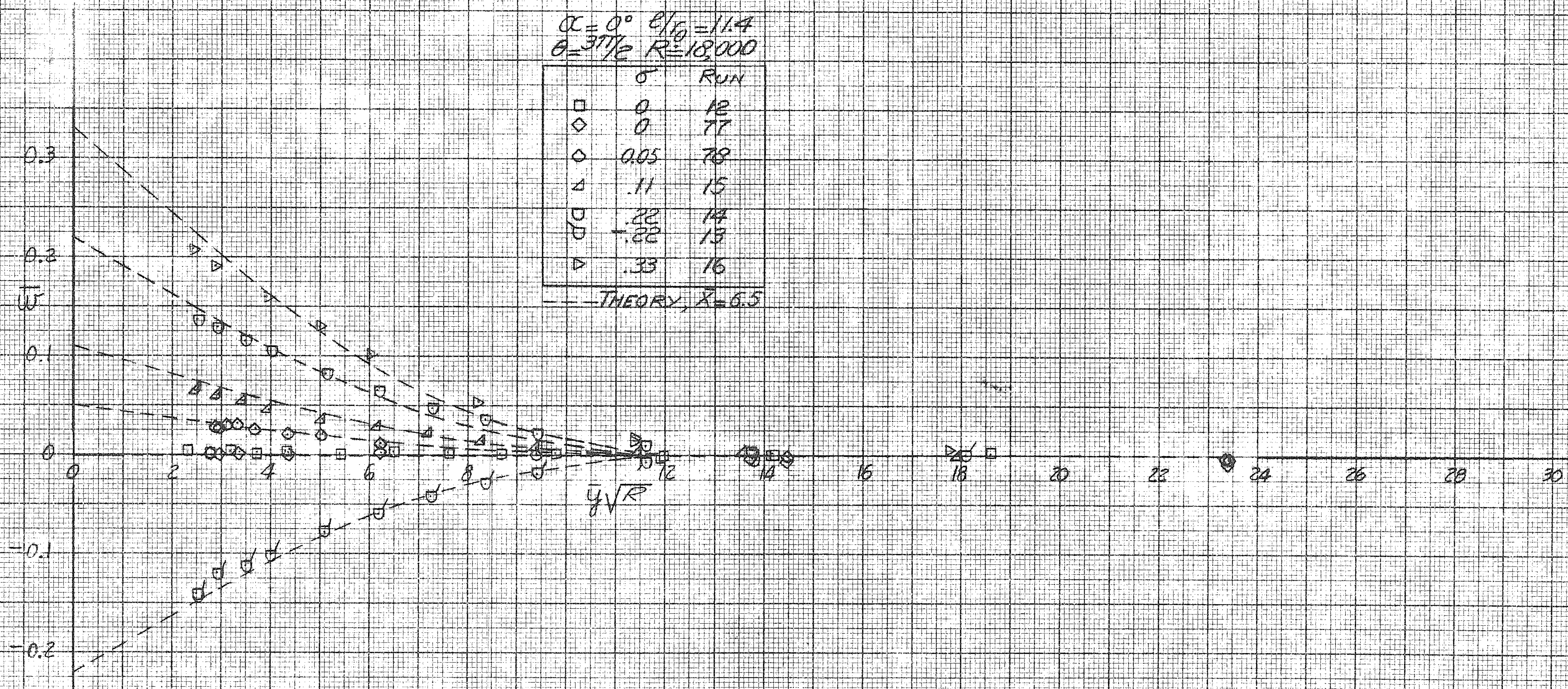

FIGURE C10

FIGURE C10

APPENDIX D

VELOCITY PROFILES

AT A YAW ANGLE OF 3 DEGREES

28 figures

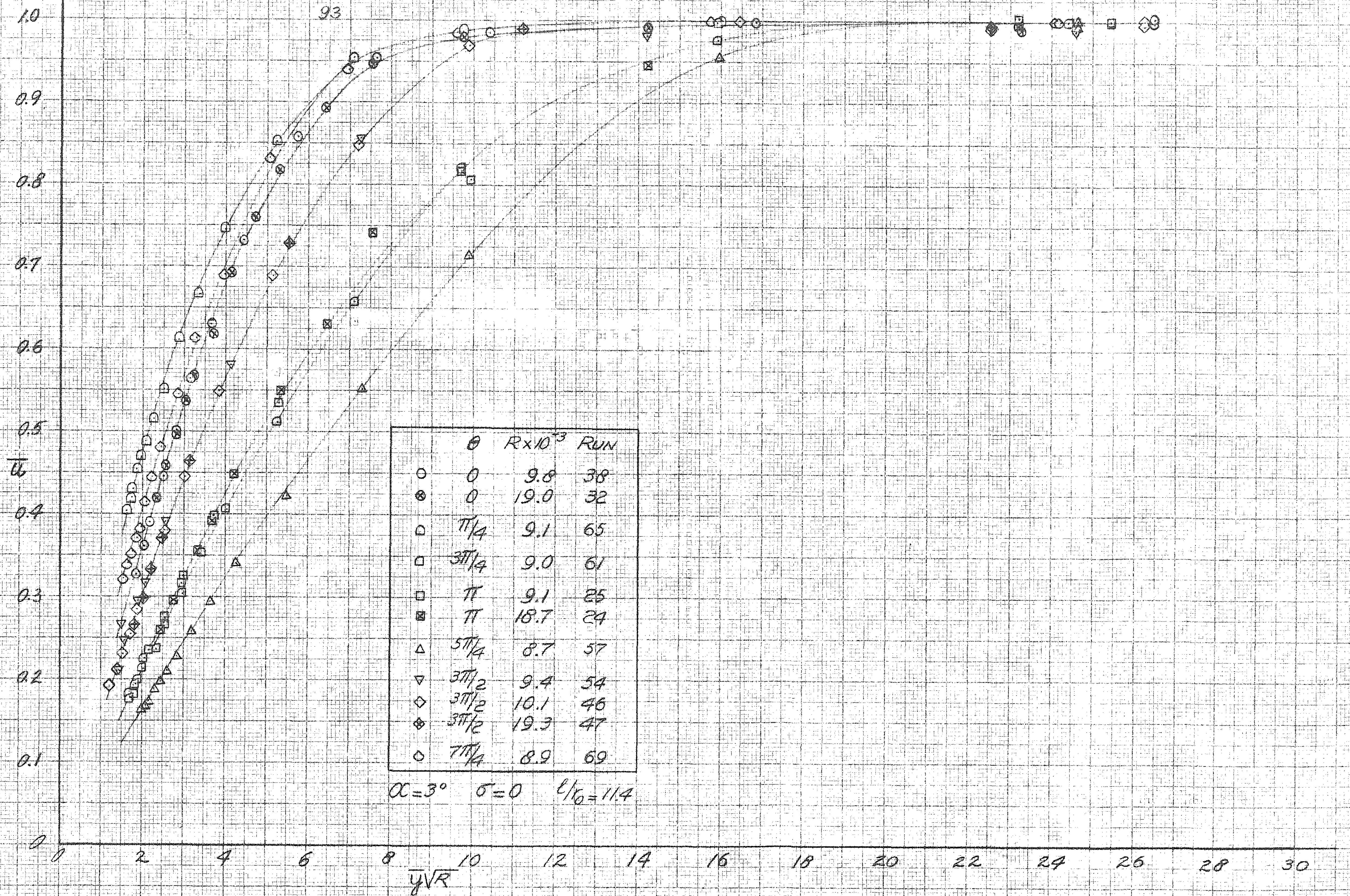

FIGURE D1

FIGURE D1

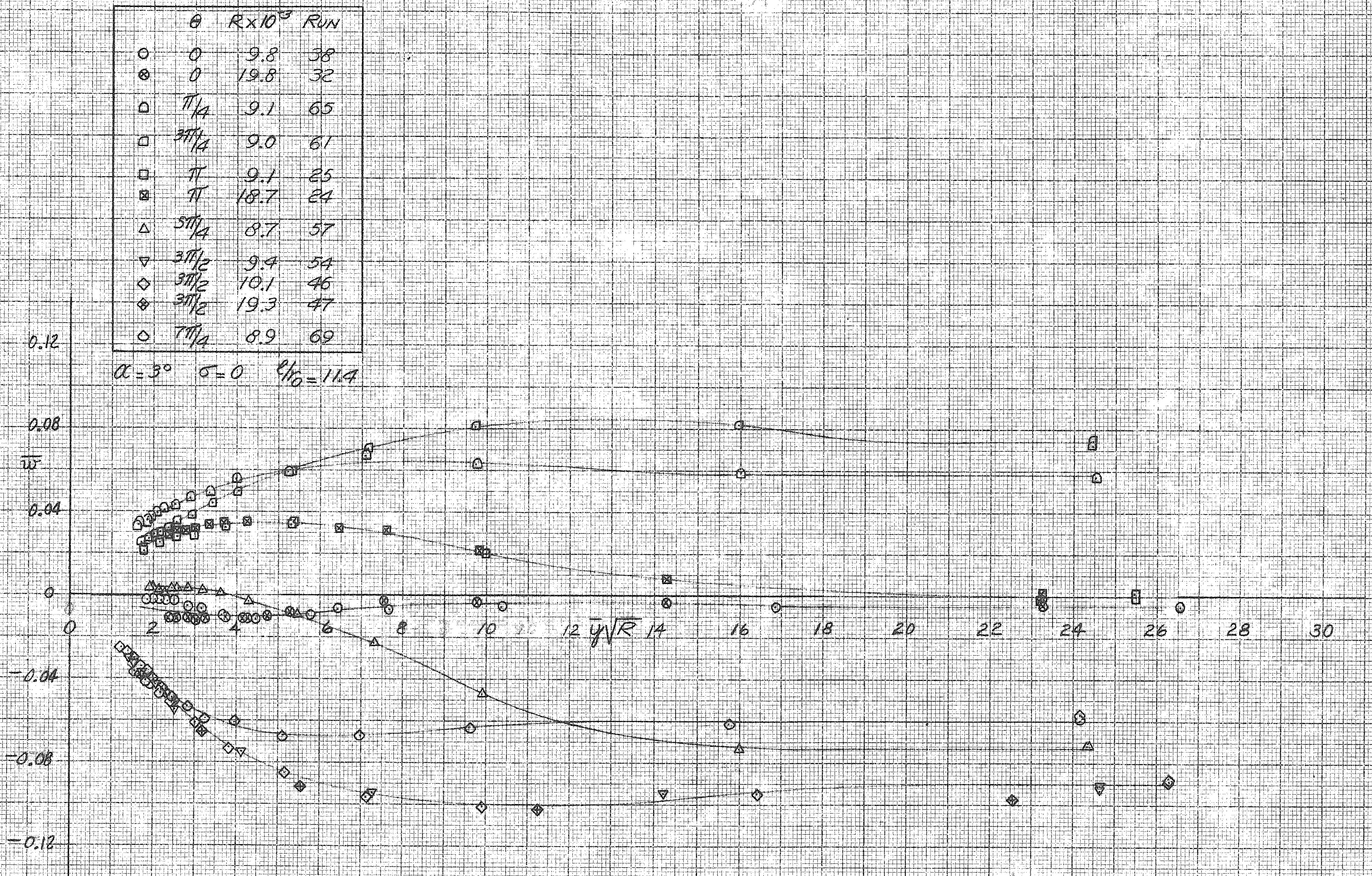

FIGURE D2

FIGURE D2

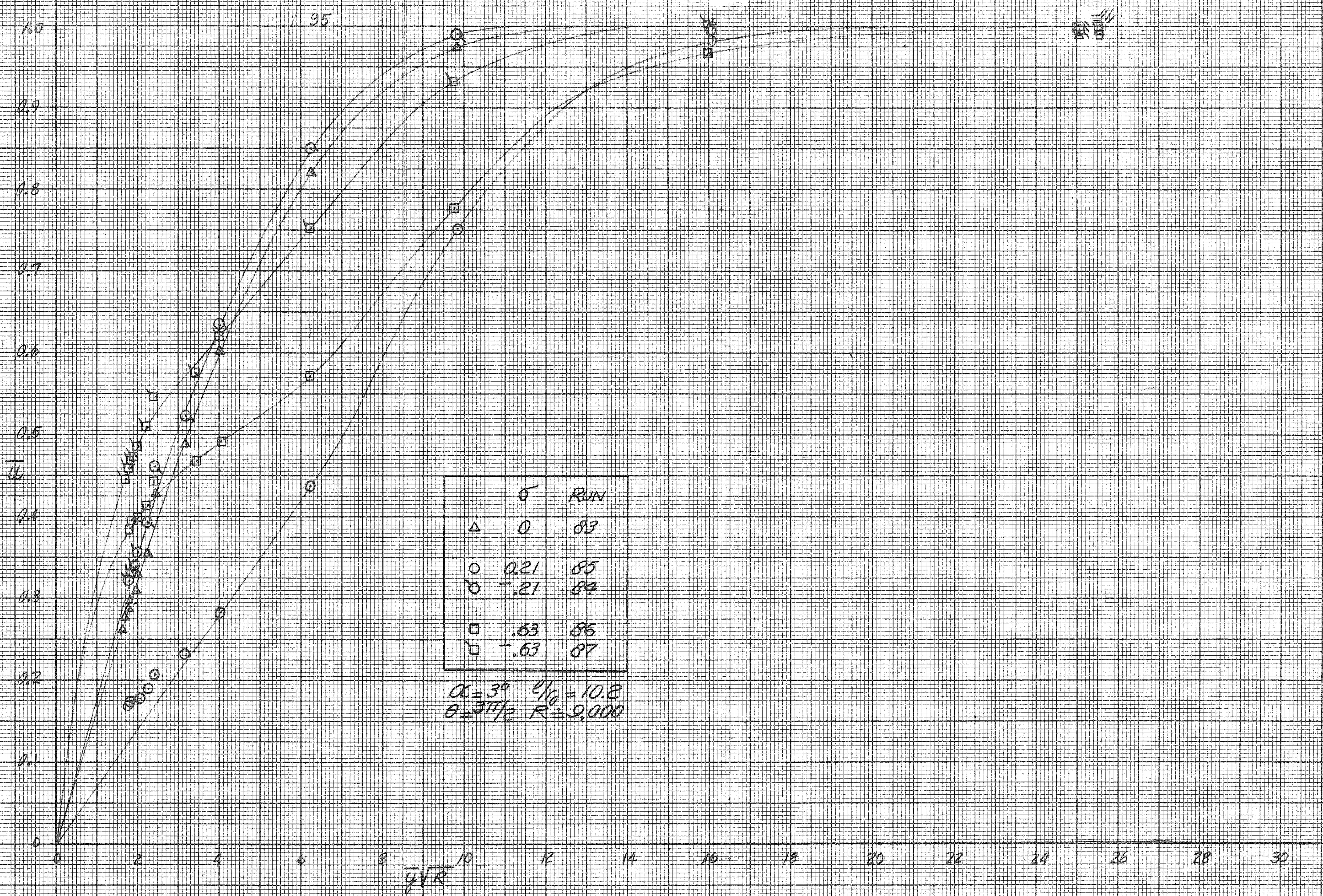

FIGURE D3

FIGURE D3

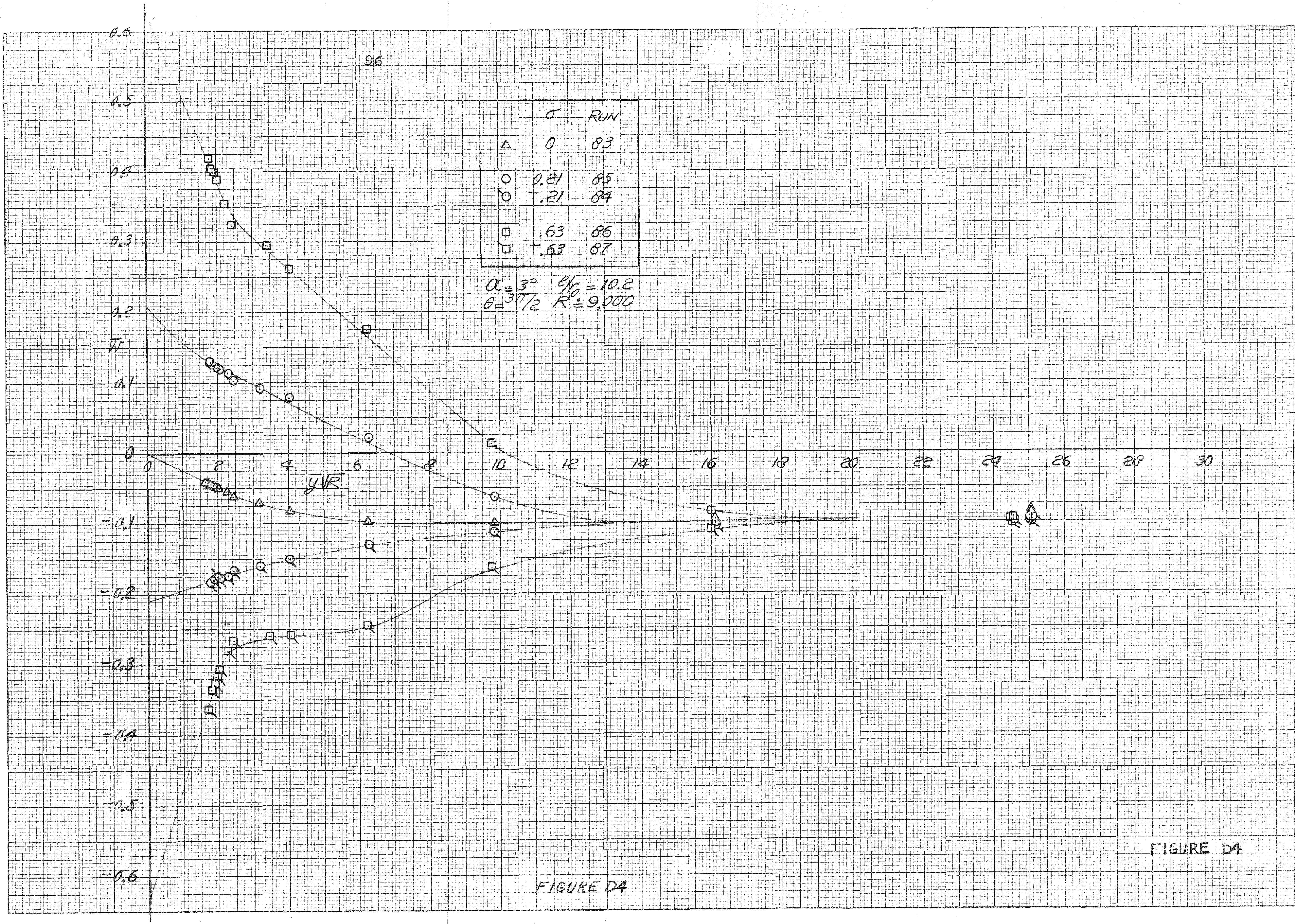

FIGURE D4

FIGURE D4

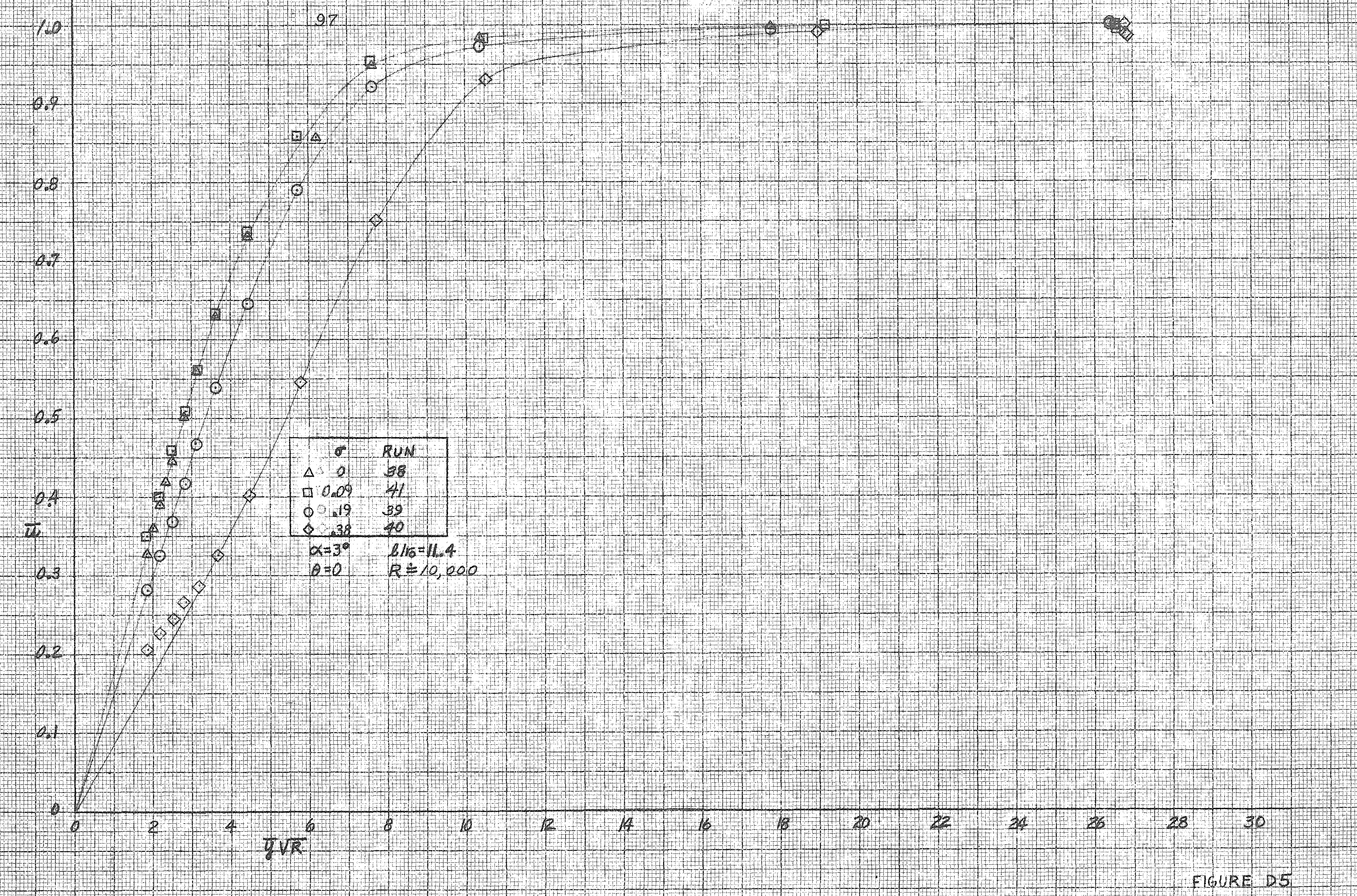
1.0
0.9
0.8
0.7
0.6
0.5
0.4
0.3
0.2
0.1
0
u
0
2
4
6
8
10
12
14
16
18
20
22
24
26
28
30
U/ν √R
σ RUN
△ 0 38
□ 0.09 41
○ .19 39
◇ .38 40
α=3° ℓ/b=11.4
θ=0 R≐10,000
FIGURE D5

FIGURE D5

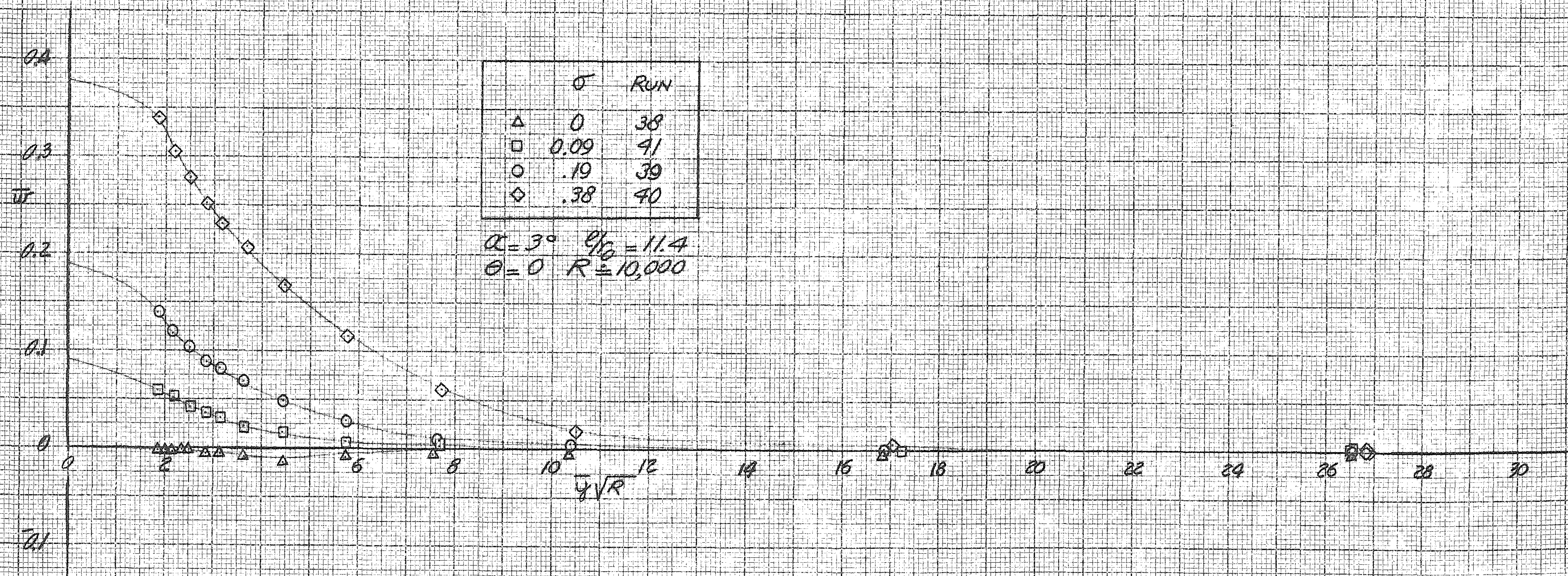

FIGURE D6

FIGURE D6

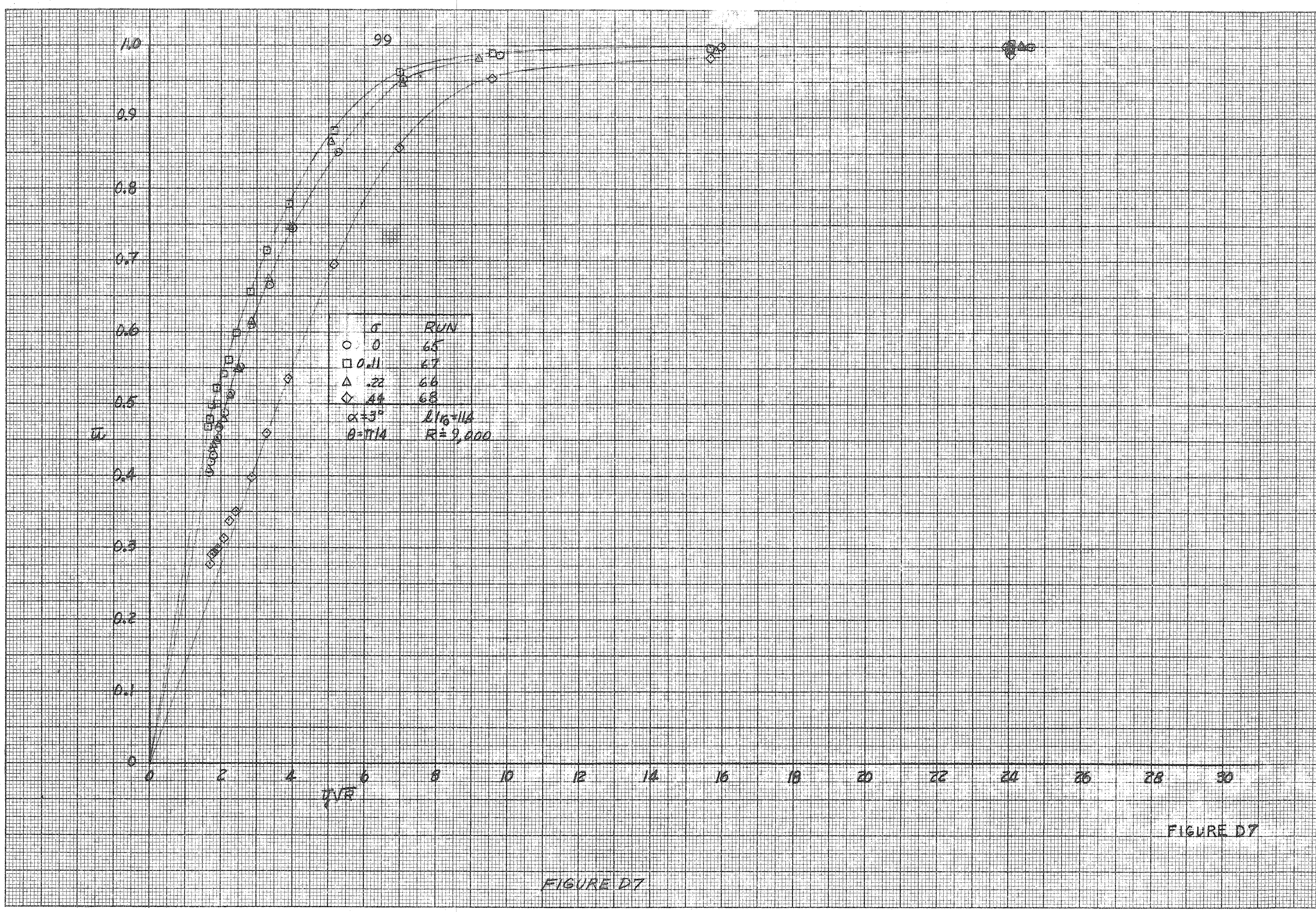

1.0
0.9
0.8
0.7
0.6
0.5
0.4
0.3
0.2
0.1
0
$\bar{u}$
0 2 4 6 8 10 12 14 16 18 20 22 24 26 28 30
$\frac{t}{l}\sqrt{R}$
σ RUN
○ 0 65
□ 0.11 67
△ .22 66
◇ .44 68
α = 3°
θ = π/4
$l/r_0 = 114$
$R \doteq 9{,}000$
FIGURE D7

FIGURE D7

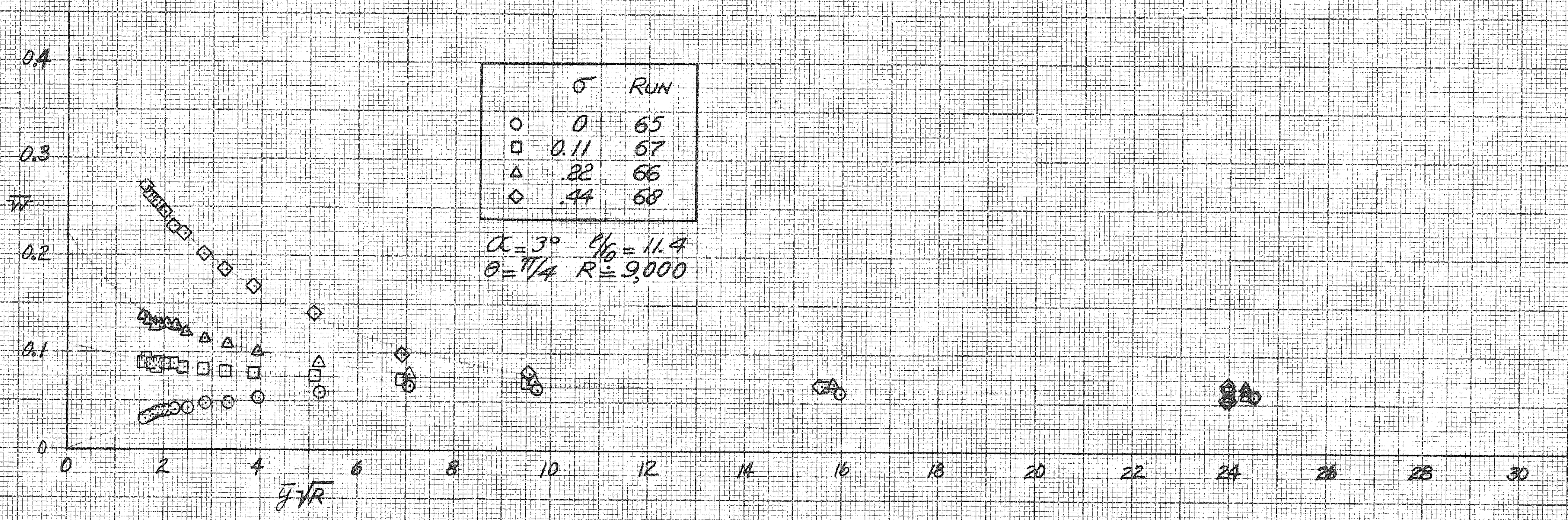

0.4
0.3
$\overline{W}$
0.2
0.1
0
0
2
4
6
8
10
12
14
16
18
20
22
24
26
28
30
$\bar{y}\sqrt{R}$
σ
RUN
0
65
0.11
67
.22
66
.44
68
α = 3°
e/b = 11.4
θ = π/4
R ≐ 9,000
FIGURE D8

FIGURE D8

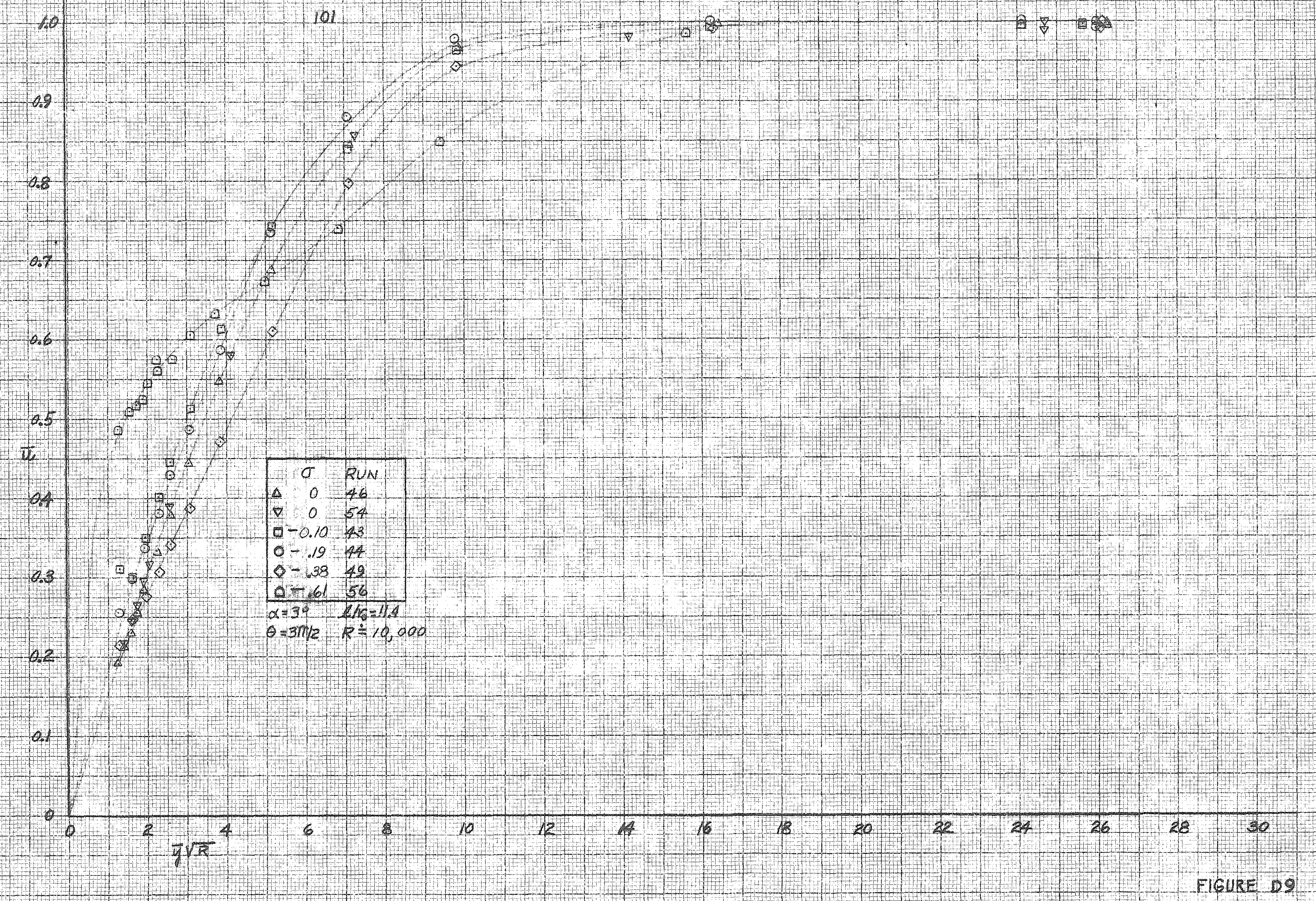

1.0
0.9
0.8
0.7
0.6
0.5
u
0.4
0.3
0.2
0.1
0
0 2 4 6 8 10 12 14 16 18 20 22 24 26 28 30
y√R
σ RUN
△ 0 46
▽ 0 54
□ −0.10 43
○ −.19 44
◇ −.38 49
⌂ −.61 56
α = 3° ℓ/r₀ = 11.4
θ = 3π/2 R ≐ 10,000
FIGURE D9

FIGURE D9

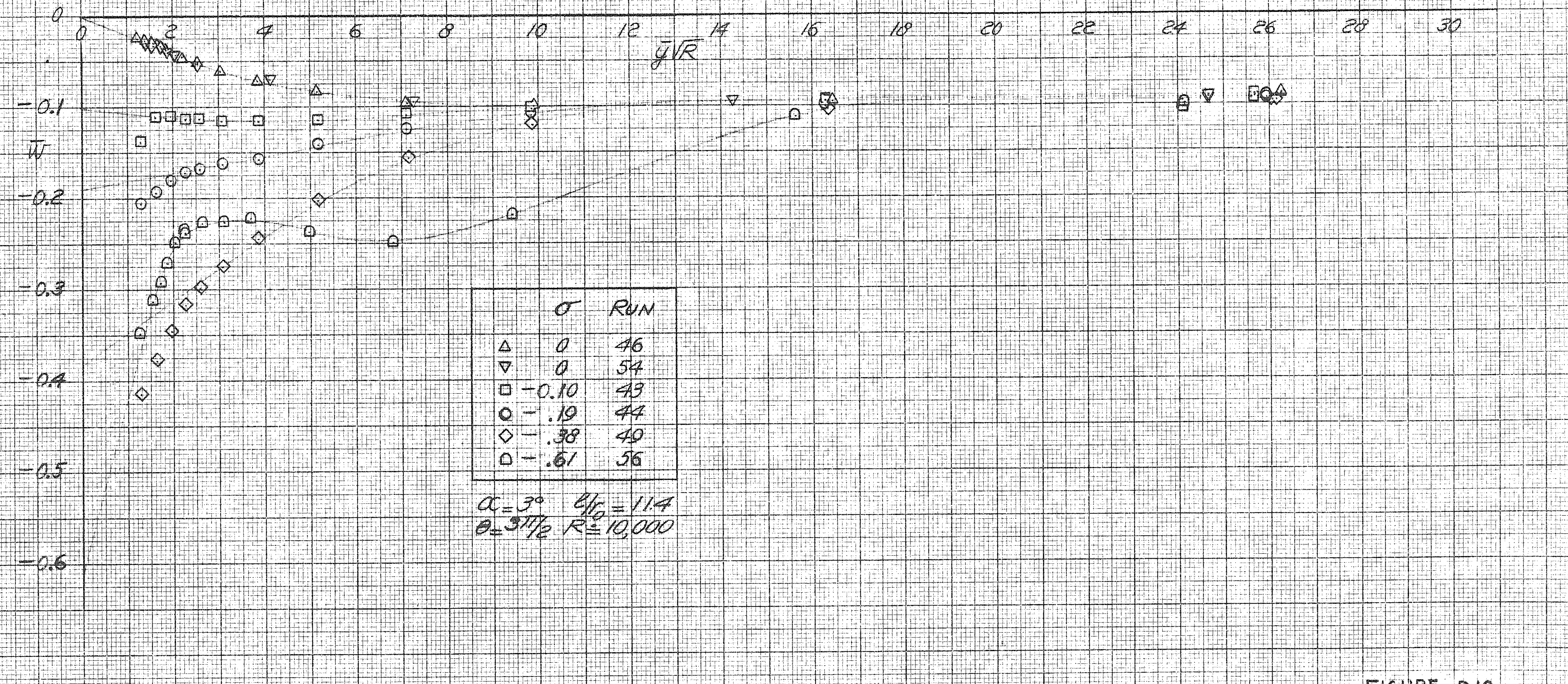
0
0
2
4
6
8
10
12
14
16
18
20
22
24
26
28
30
$\bar{y}\sqrt{R}$
-0.1
$\bar{W}$
-0.2
-0.3
-0.4
-0.5
-0.6
σ RUN
△ 0 46
▽ 0 54
□ -0.10 43
○ - .19 44
◇ - .38 49
⌂ - .61 56
α = 3° ℓ/r₀ = 114
θ = 3π/2 R ≐ 10,000
FIGURE D10

FIGURE D10

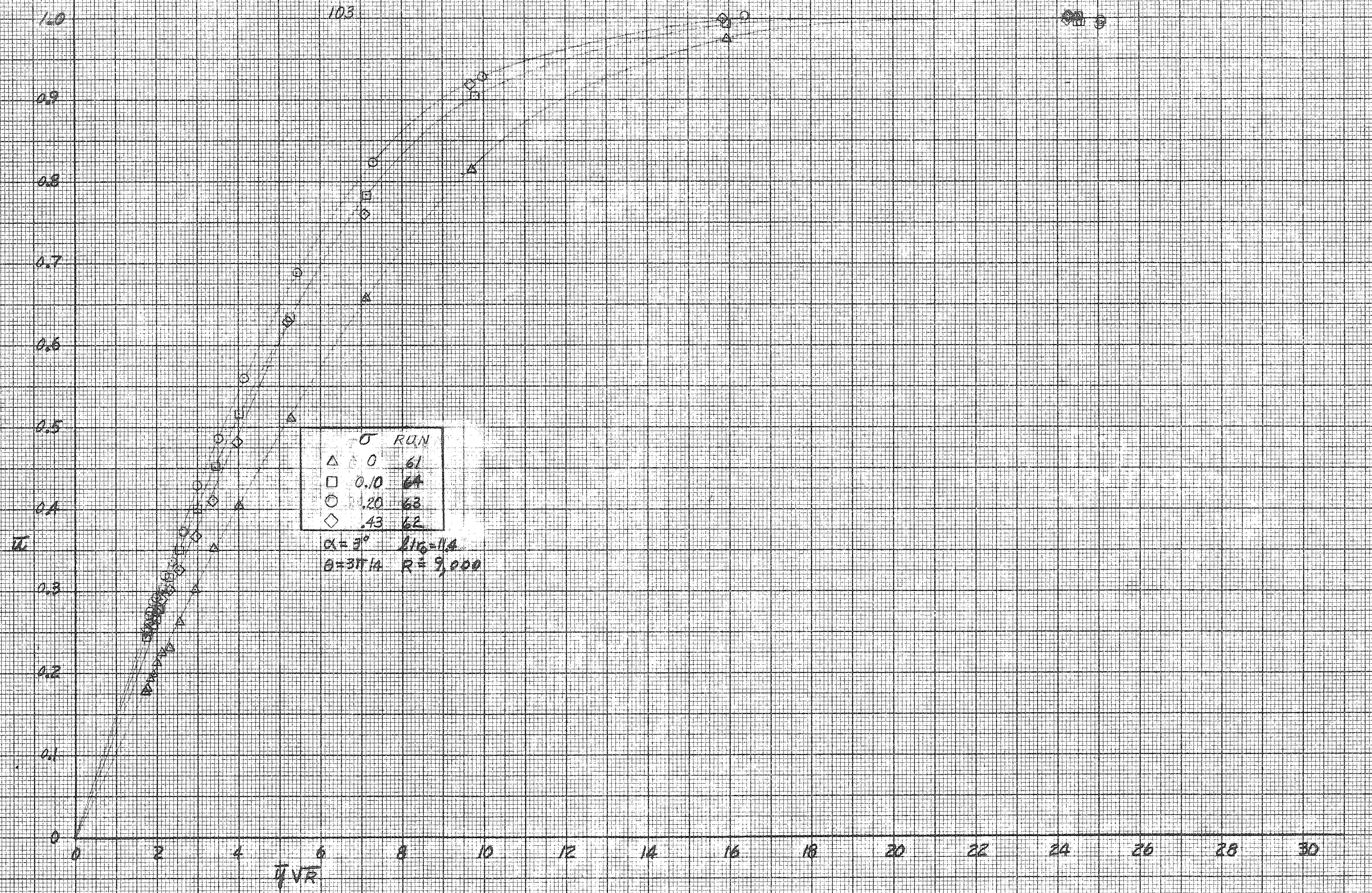
1.0
0.9
0.8
0.7
0.6
0.5
0.4
0.3
0.2
0.1
0
$\bar{u}$
0
2
4
6
8
10
12
14
16
18
20
22
24
26
28
30
$\frac{\bar{y}}{l}\sqrt{R}$
σ RUN
△ 0 61
□ 0.10 64
○ .20 63
◇ .43 62
α = 3°
l/r₀ = 11.4
θ = 3π/4
R = 9,000
FIGURE D11

FIGURE D11

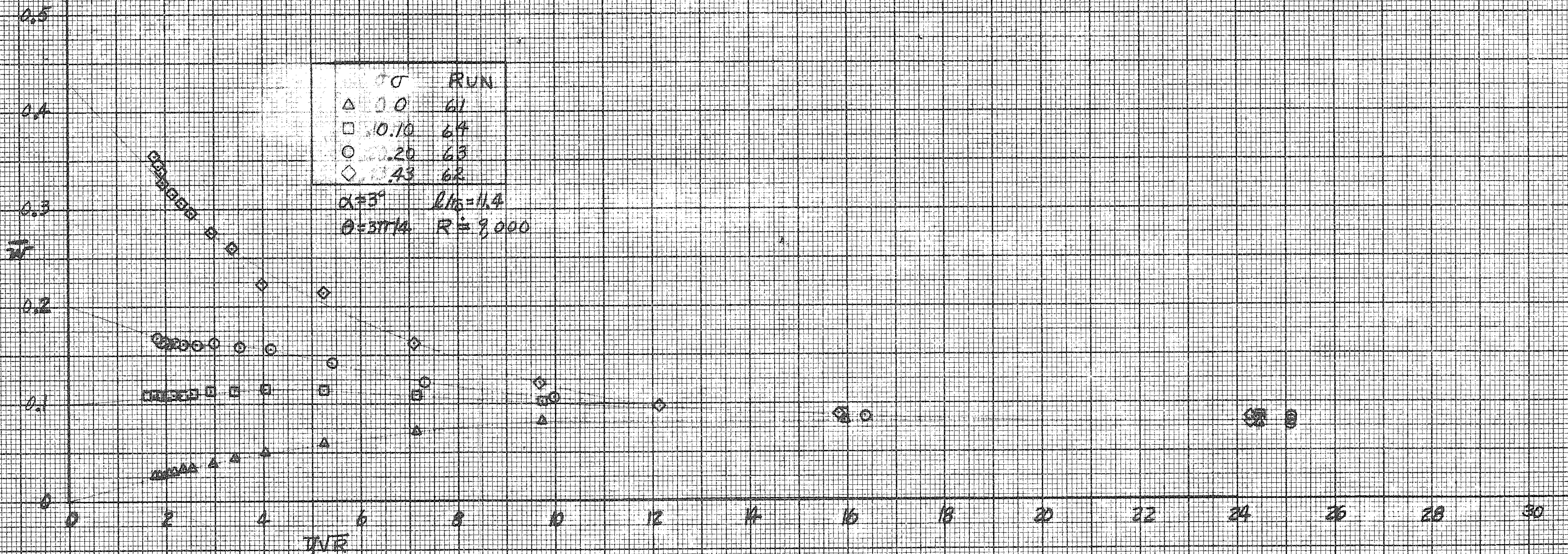

FIGURE D12

FIGURE D12

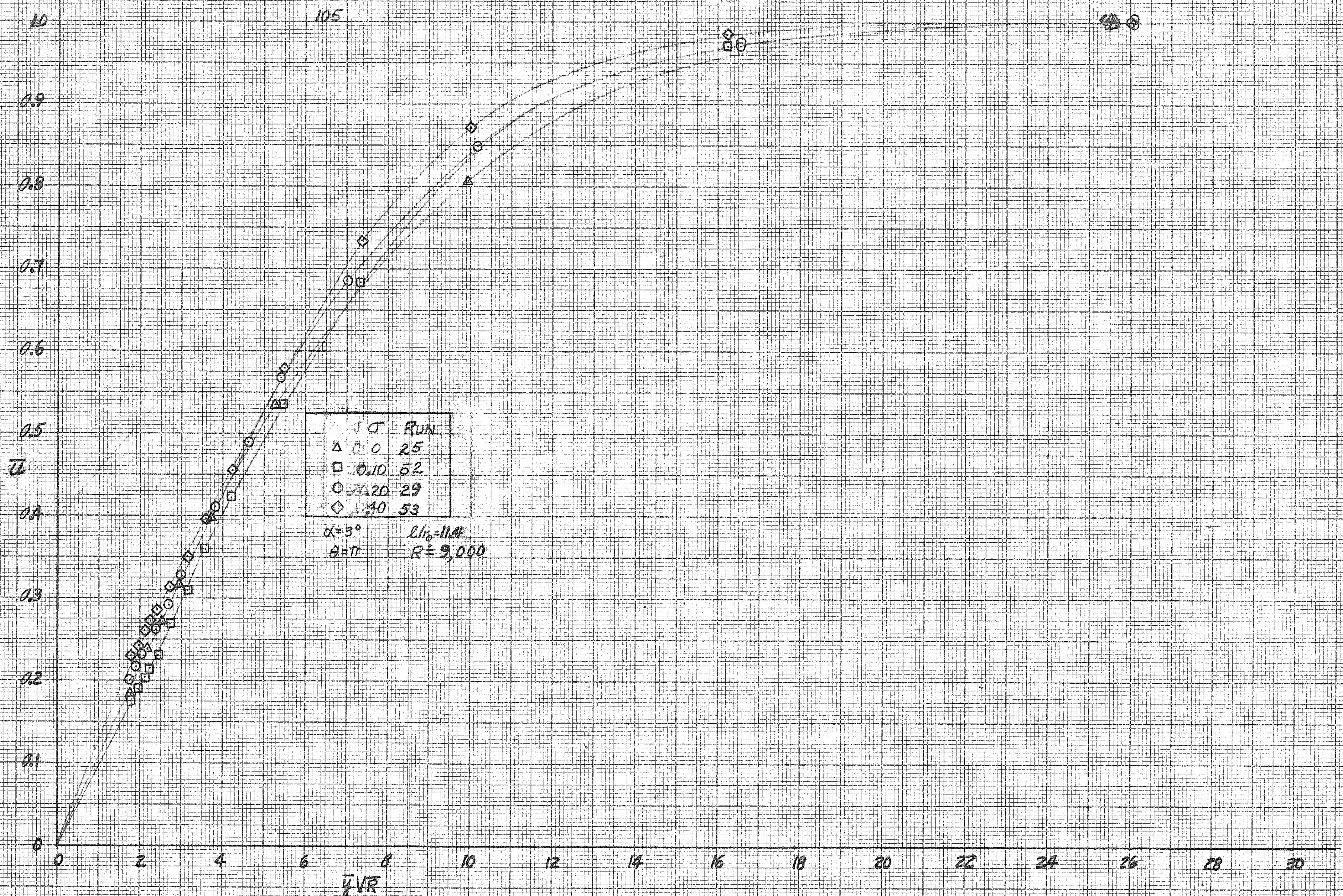

FIGURE D13

FIGURE D13

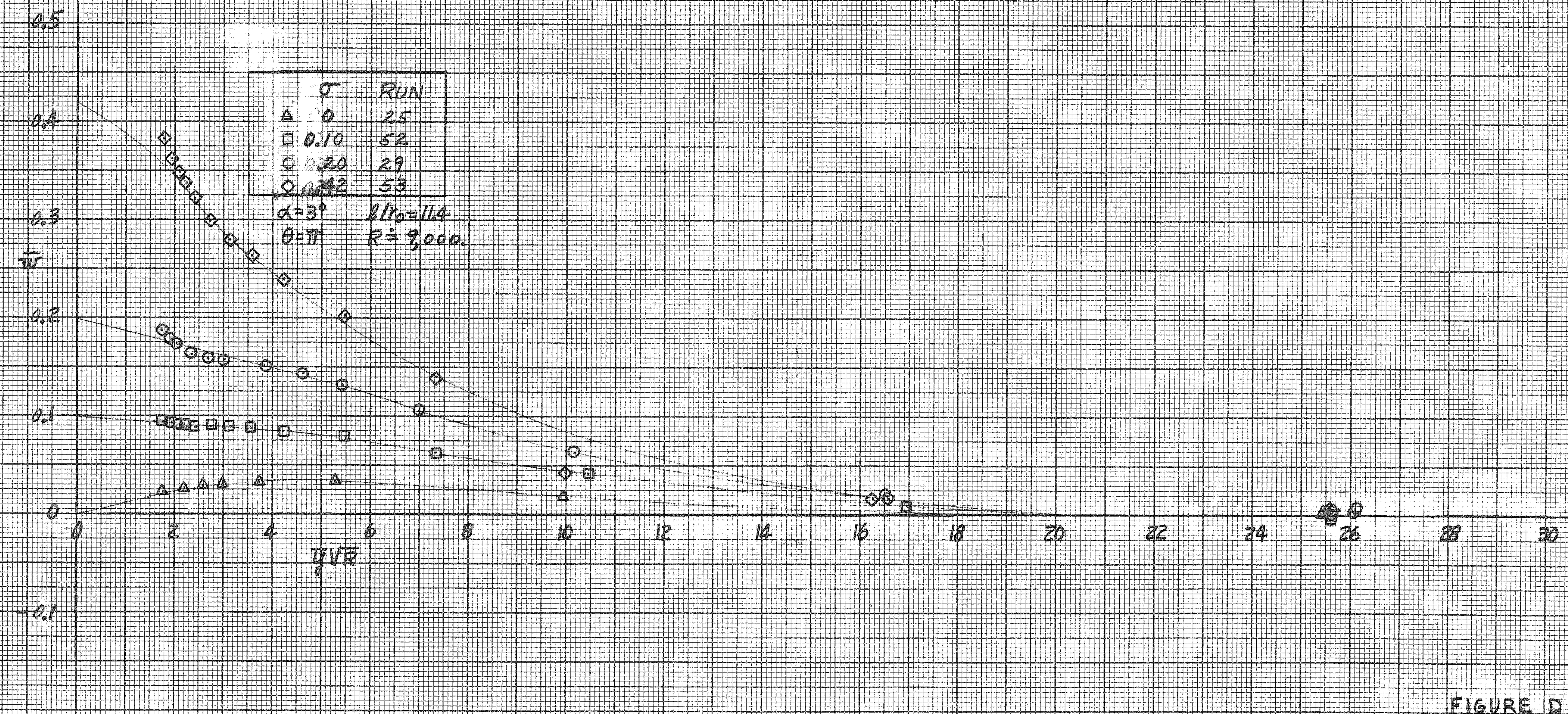
σ RUN
△ 0 25
□ 0.10 52
○ 0.20 29
◇ 0.42 53
α = 3° ℓ/r₀ = 11.4
θ = π R ≐ 9,000.
w̄
0.5
0.4
0.3
0.2
0.1
0
-0.1
0 2 4 6 8 10 12 14 16 18 20 22 24 26 28 30
ū√R
FIGURE D14

FIGURE D14

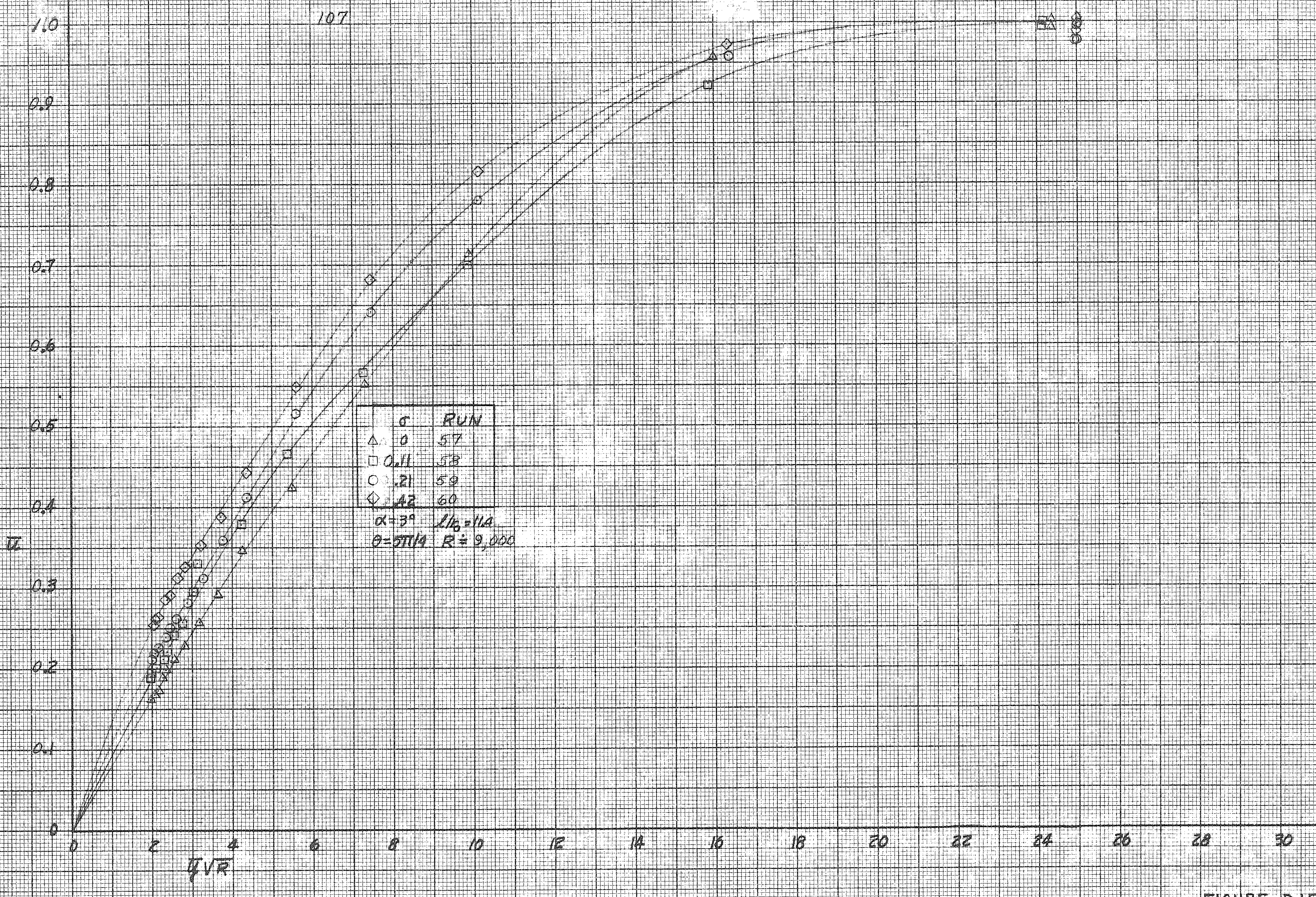

1.0
0.9
0.8
0.7
0.6
0.5
0.4
0.3
0.2
0.1
0
$\bar{u}$
0
2
4
6
8
10
12
14
16
18
20
22
24
26
28
30
$\bar{y}\sqrt{R}$
σ RUN
△ 0 57
□ 0.11 58
○ .21 59
◇ .42 60
α=3° l/l_0=11.4
θ=5π/4 R ≐ 9,000
FIGURE D15

FIGURE D15

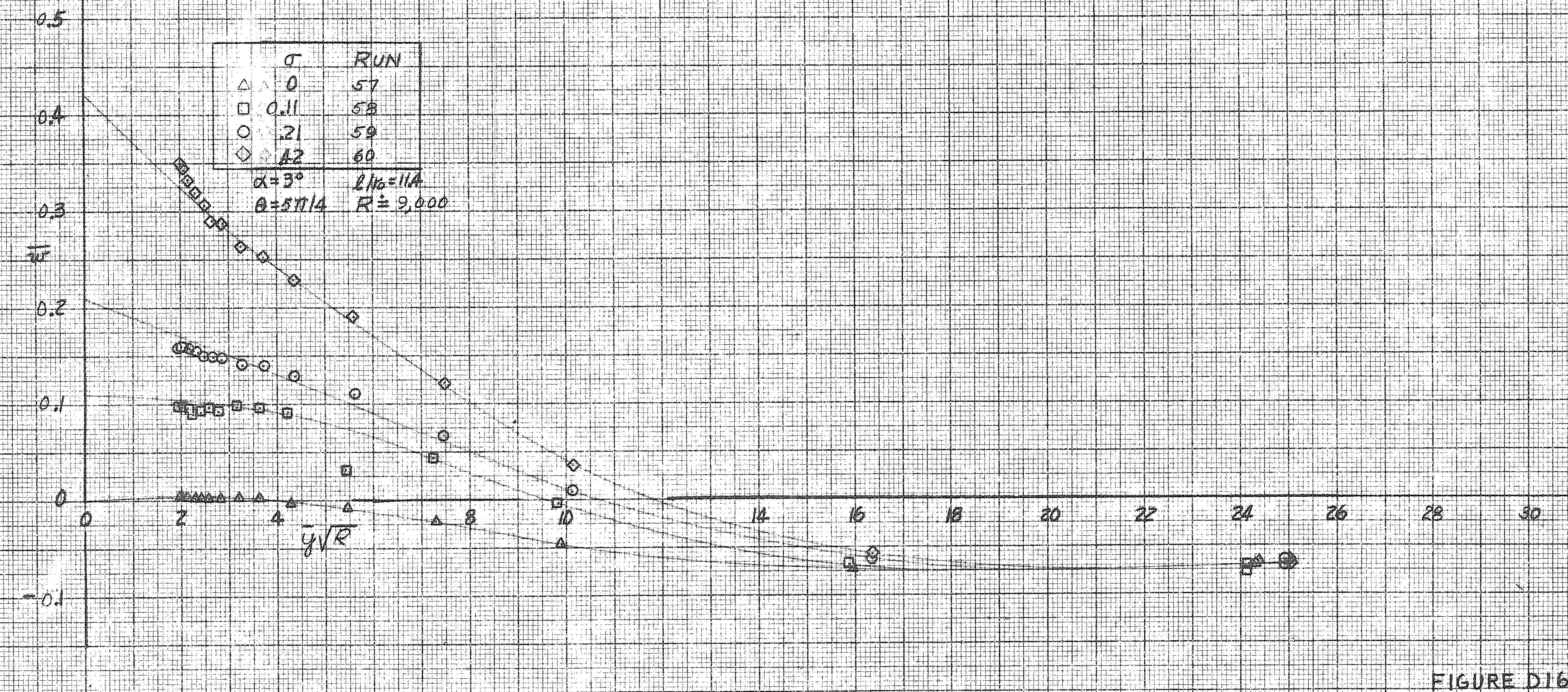
σ
RUN
0
57
0.11
58
.21
59
.42
60
α = 3°
l/lo = 11.4
θ = 5π/4
R ≐ 9,000
0.5
0.4
0.3
0.2
0.1
0
-0.1
w̄
0
2
4
8
10
14
16
18
20
22
24
26
28
30
ȳ√R
FIGURE D16

FIGURE D16

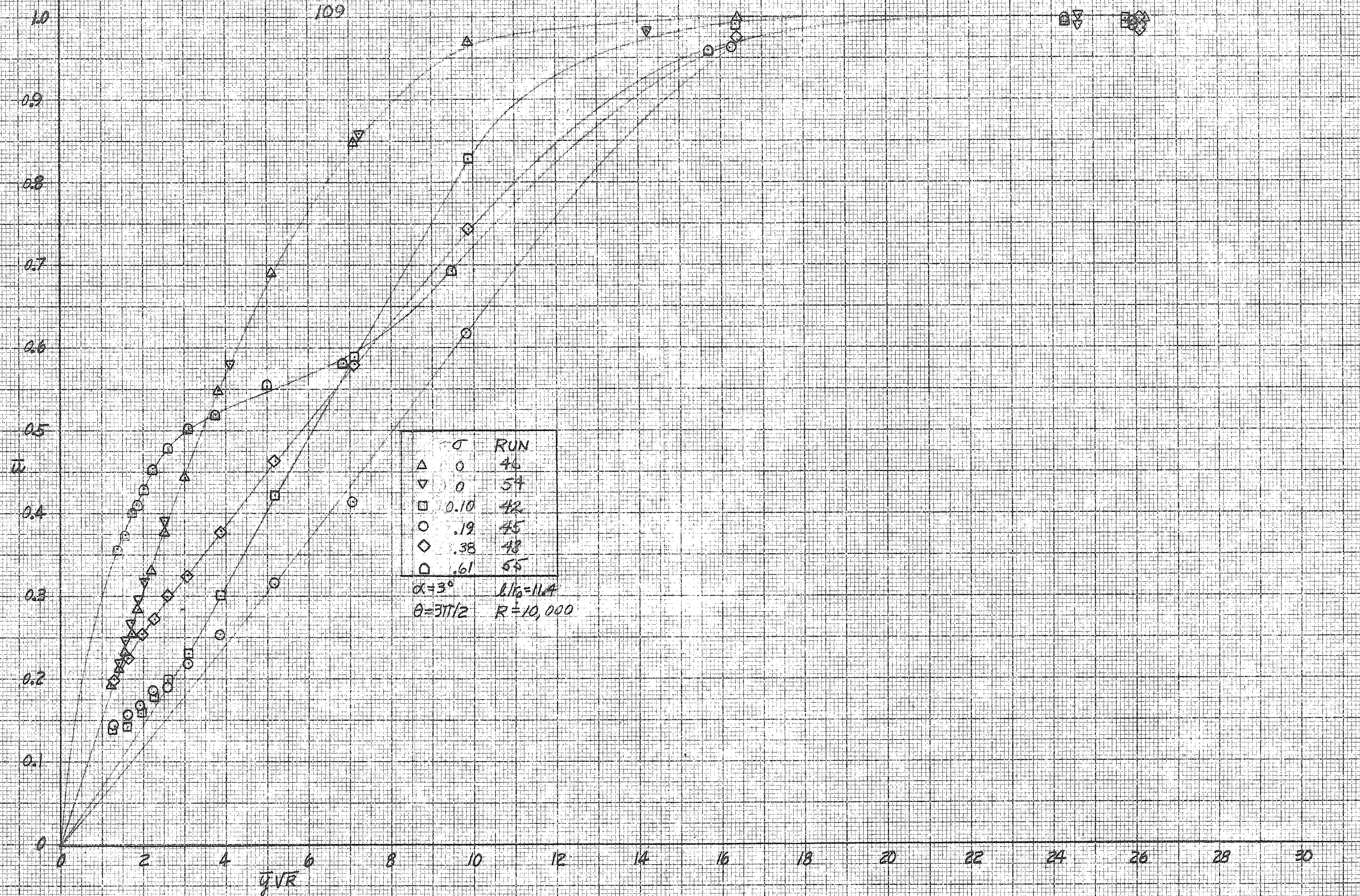

1.0
0.9
0.8
0.7
0.6
0.5
0.4
0.3
0.2
0.1
0
$\bar{u}$
0
2
4
6
8
10
12
14
16
18
20
22
24
26
28
30
$\bar{y}\sqrt{R}$
σ RUN
0 46
0 54
0.10 42
.19 45
.38 48
.61 65
α=3° l/r_0=11.4
θ=3π/2 R=10,000
FIGURE D17

FIGURE D17

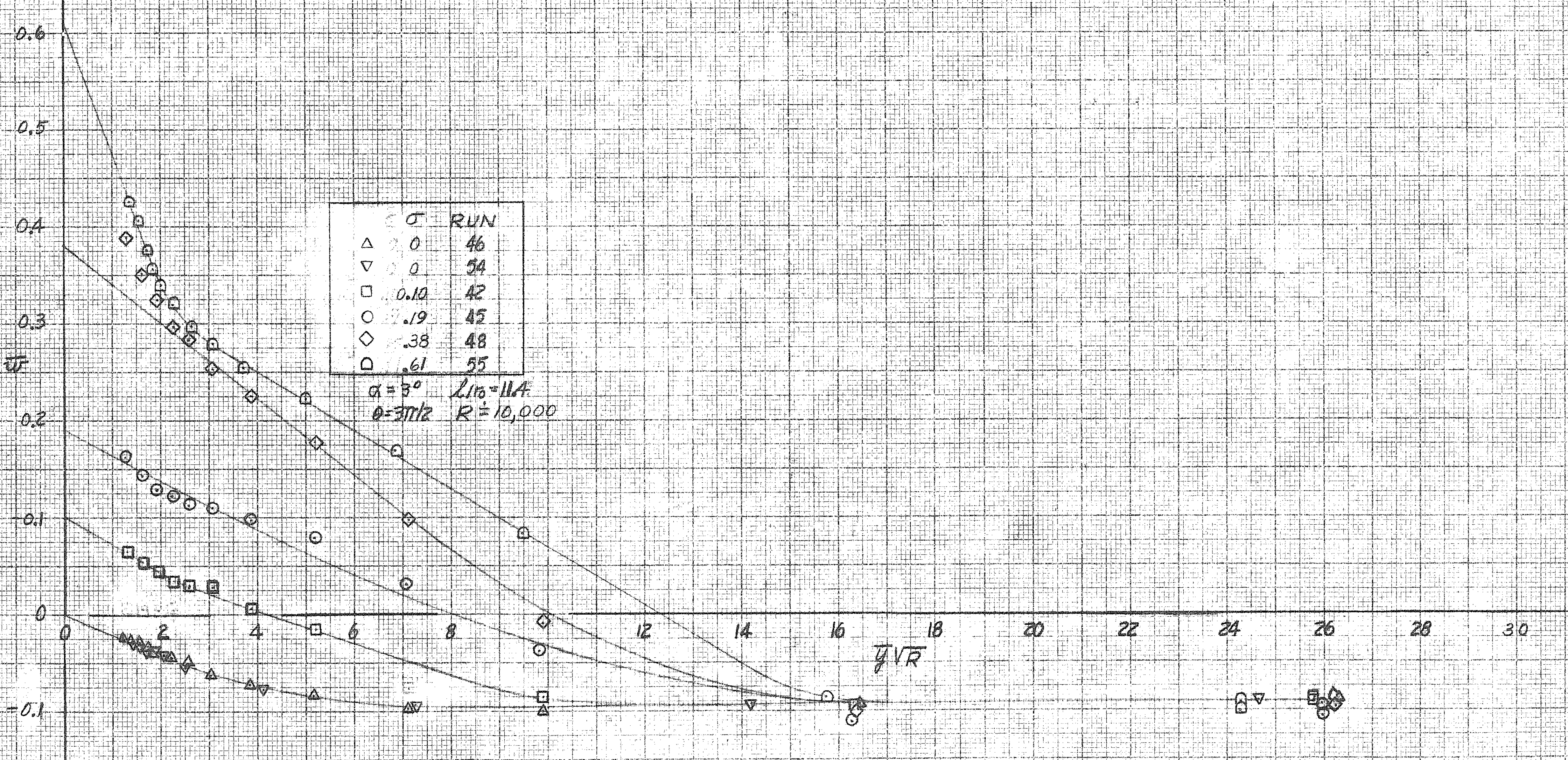

FIGURE D18

FIGURE D18

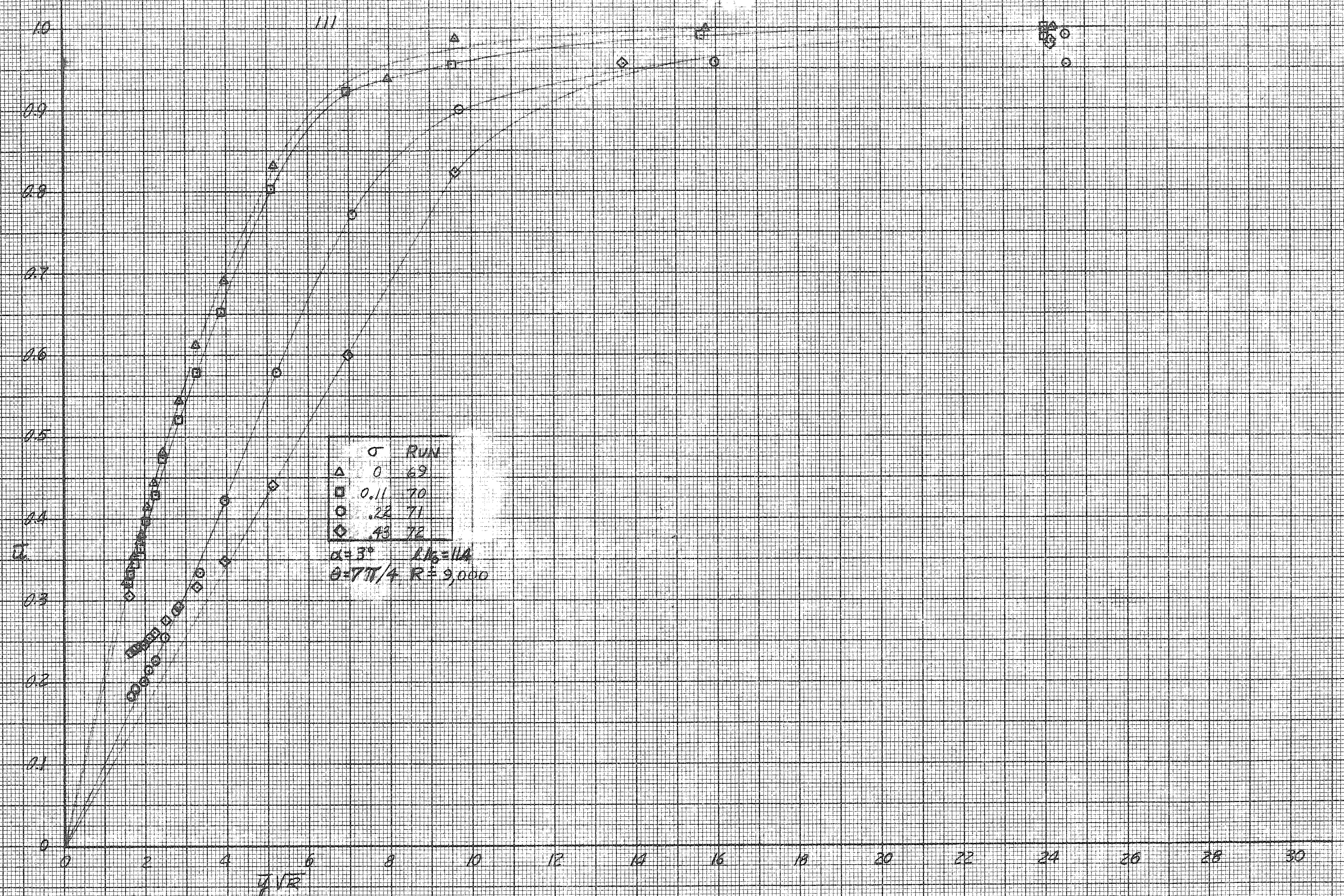
111
1.0
0.9
0.8
0.7
0.6
0.5
0.4
0.3
0.2
0.1
0
2
4
6
8
10
12
14
16
18
20
22
24
26
28
30
$\bar{u}$
$\bar{y}\sqrt{R}$
σ RUN
0 69
0.11 70
.22 71
.43 72
α = 3°
l/l₀ = 114
θ = 7π/4
R = 9,000
FIGURE D19

FIGURE D19

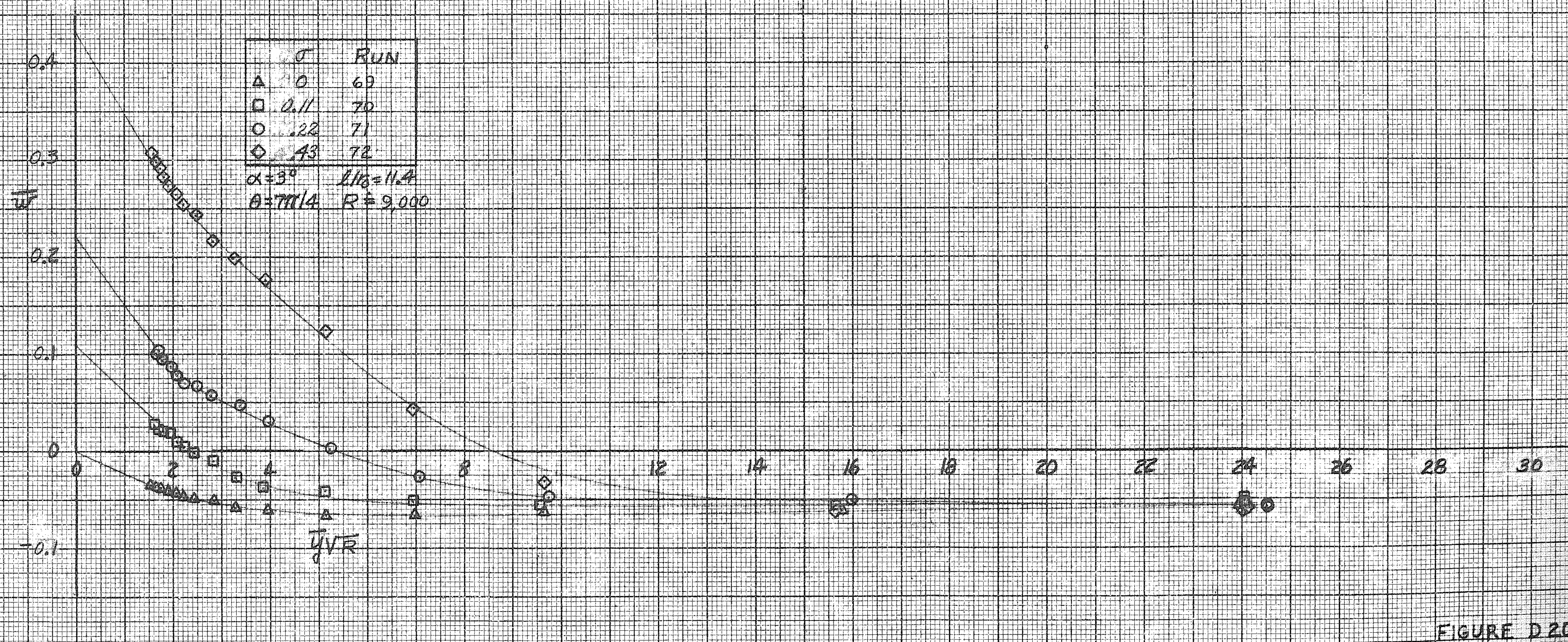
σ RUN
△ 0 69
□ 0.11 70
○ .22 71
◇ .43 72
α=3°
l/δ=11.4
θ=7π/4
R=9,000
0.4
0.3
0.2
0.1
0
-0.1
$\overline{w}$
0
2
4
8
12
14
16
18
20
22
24
26
28
30
$\frac{y}{d}\sqrt{R}$
FIGURE D20

FIGURE D20

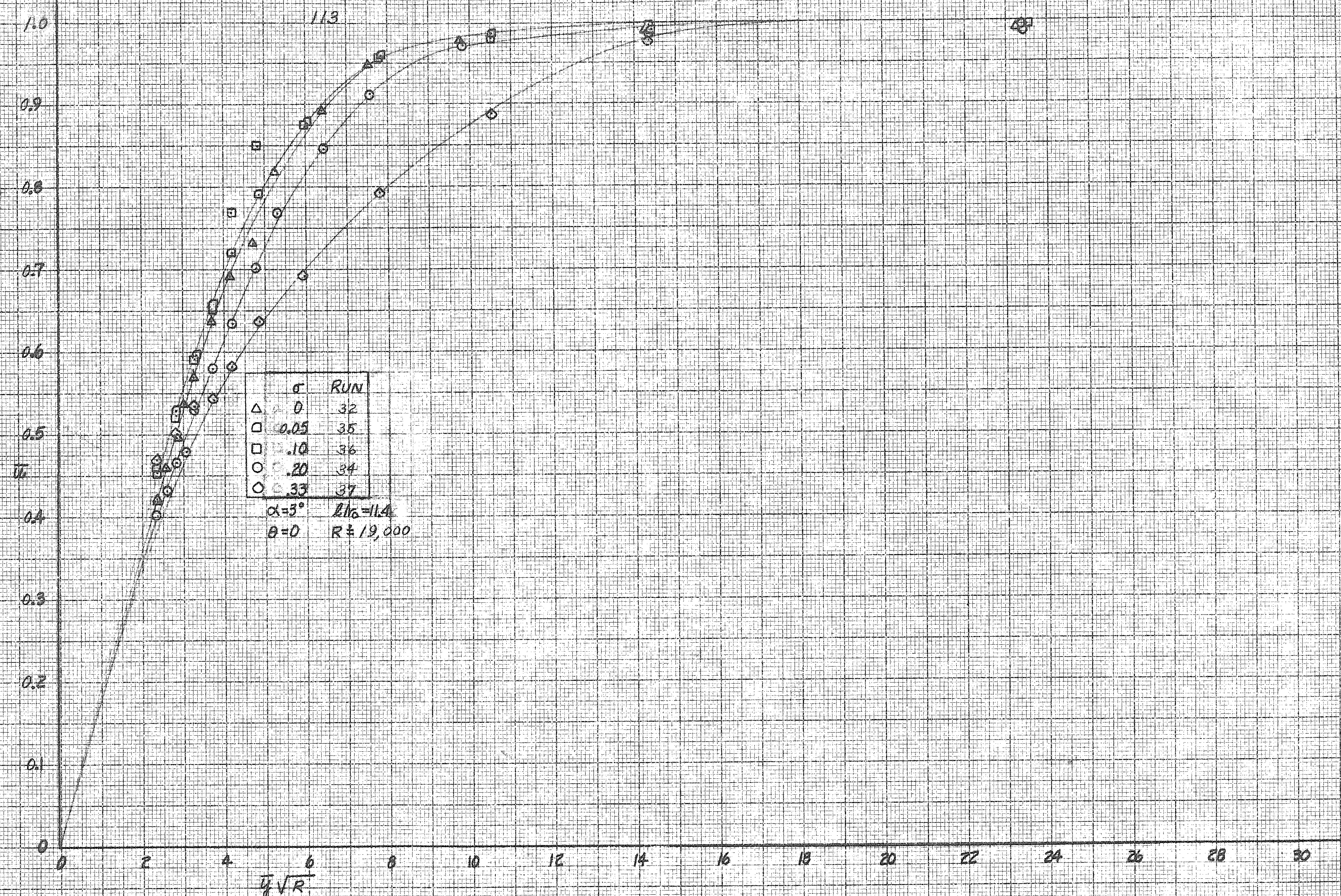
113
1.0
0.9
0.8
0.7
0.6
0.5
u/U
0.4
0.3
0.2
0.1
0
σ RUN
0 32
0.05 35
.10 36
.20 34
.33 37
α=3° l/r₀=11.4
θ=0 R ≐ 19,000
0 2 4 6 8 10 12 14 16 18 20 22 24 26 28 30
y√R
FIGURE D21
FIGURE D21

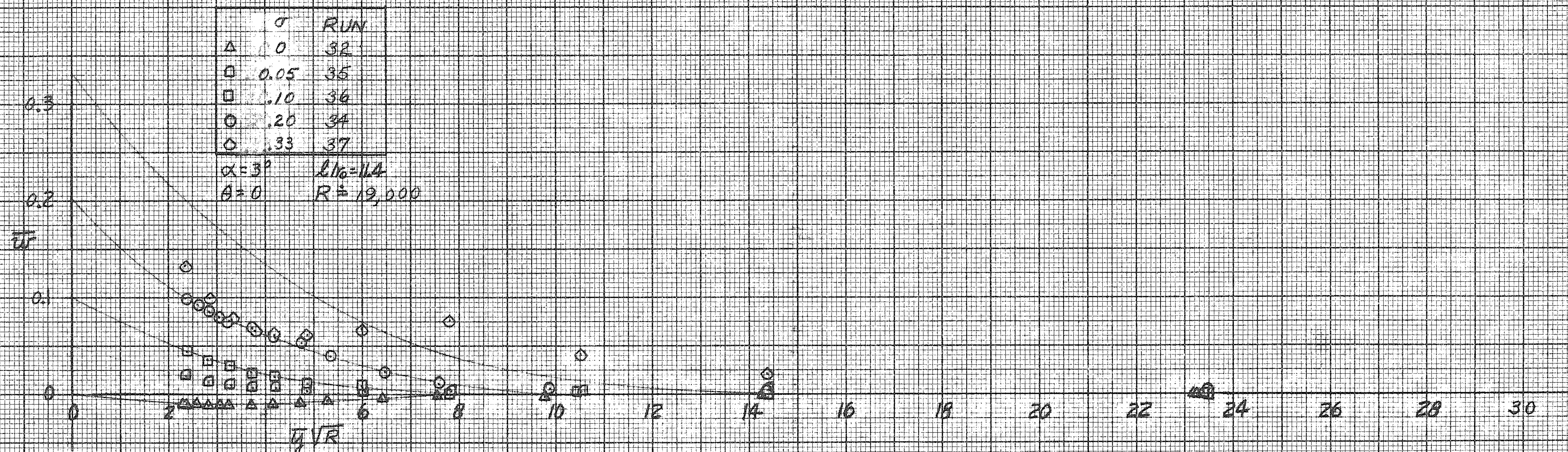

FIGURE D22

FIGURE D22

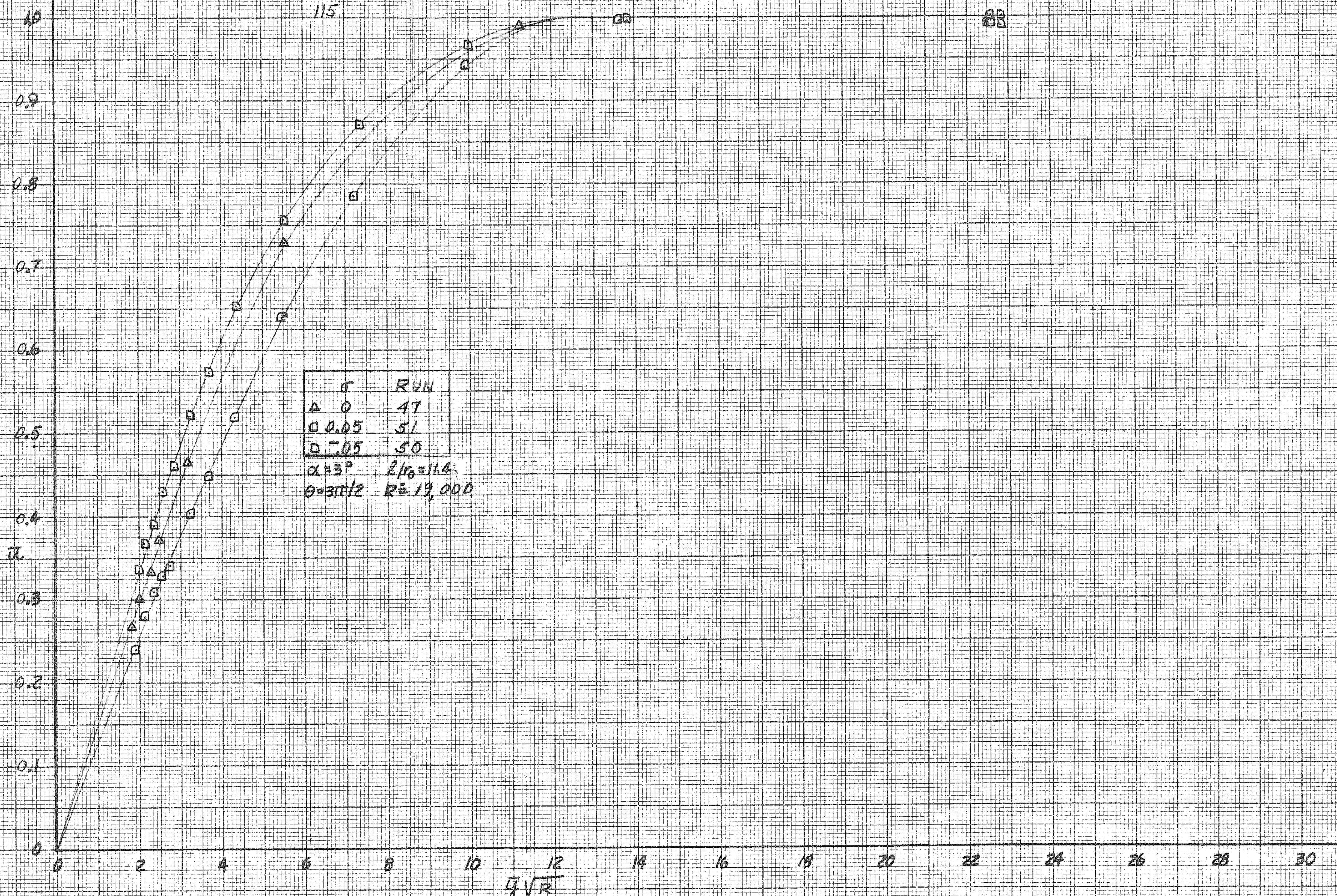

1.0
0.9
0.8
0.7
0.6
0.5
0.4
0.3
0.2
0.1
0
$\bar{u}$
0 2 4 6 8 10 12 14 16 18 20 22 24 26 28 30
$\bar{y}\sqrt{R}$
σ RUN
△ 0 47
□ 0.05 51
□ -.05 50
α=3° ℓ/r₀=11.4
θ=3π/2 R≅19,000
FIGURE D23

FIGURE D23

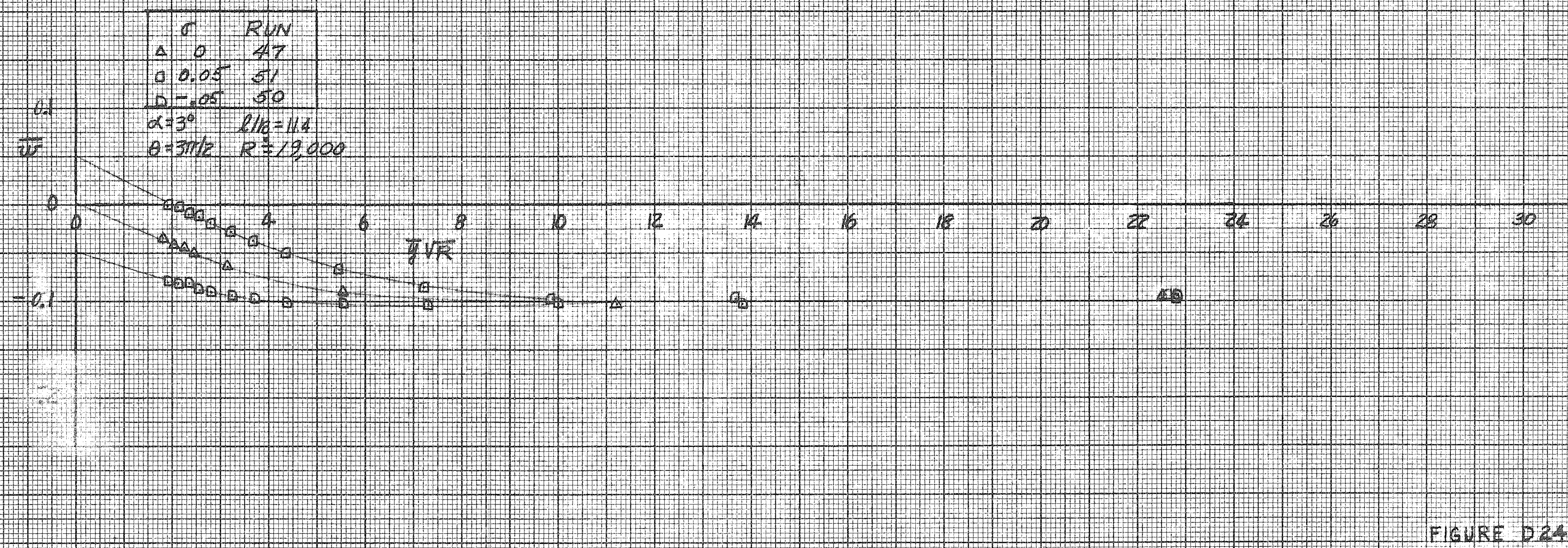

σ RUN
△ 0 47
□ 0.05 51
D -.05 50
α=3°
l/b=11.4
θ=3π/2
R=19,000
0.1
$\overline{w}$
0
-0.1
0
2
4
6
8
10
12
14
16
18
20
22
24
26
28
30
$\frac{\eta}{x}\sqrt{R}$
FIGURE D24

FIGURE D24

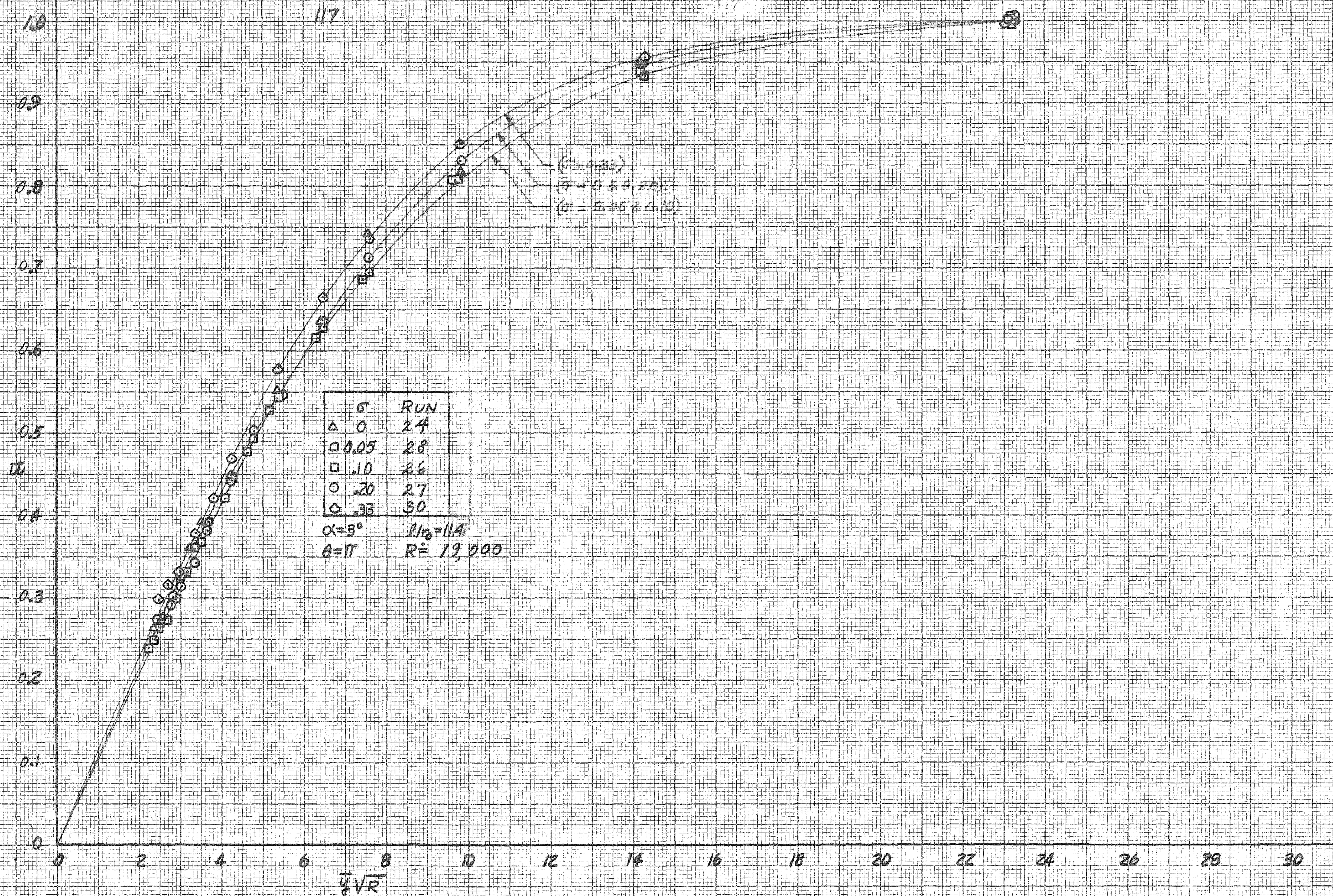

FIGURE D25

FIGURE D25

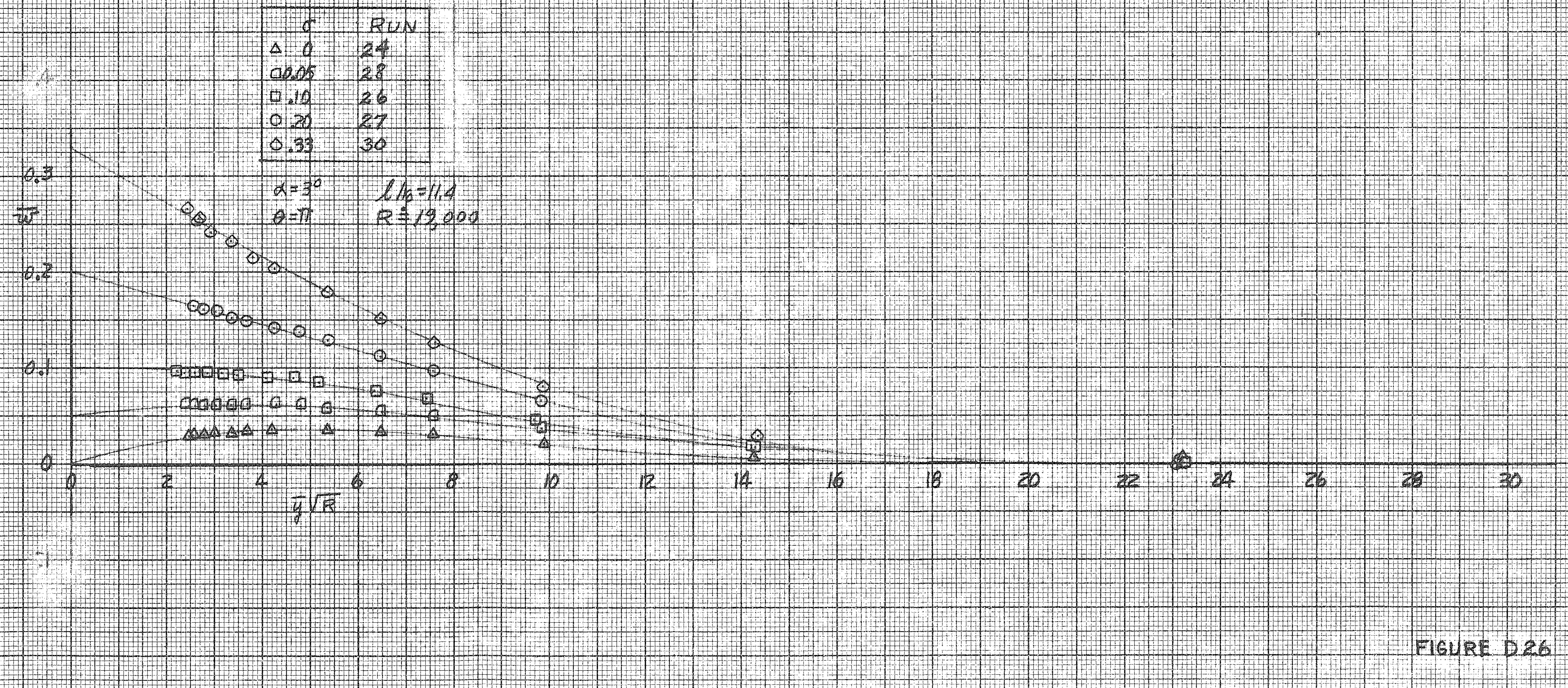
c RUN
△ 0 24
0.05 28
□ .10 26
○ .20 27
.33 30
α = 3°
θ = π
l/b = 11.4
R ≐ 19,000
0.3
0.2
0.1
0
0 2 4 6 8 10 12 14 16 18 20 22 24 26 28 30
FIGURE D26

FIGURE D26

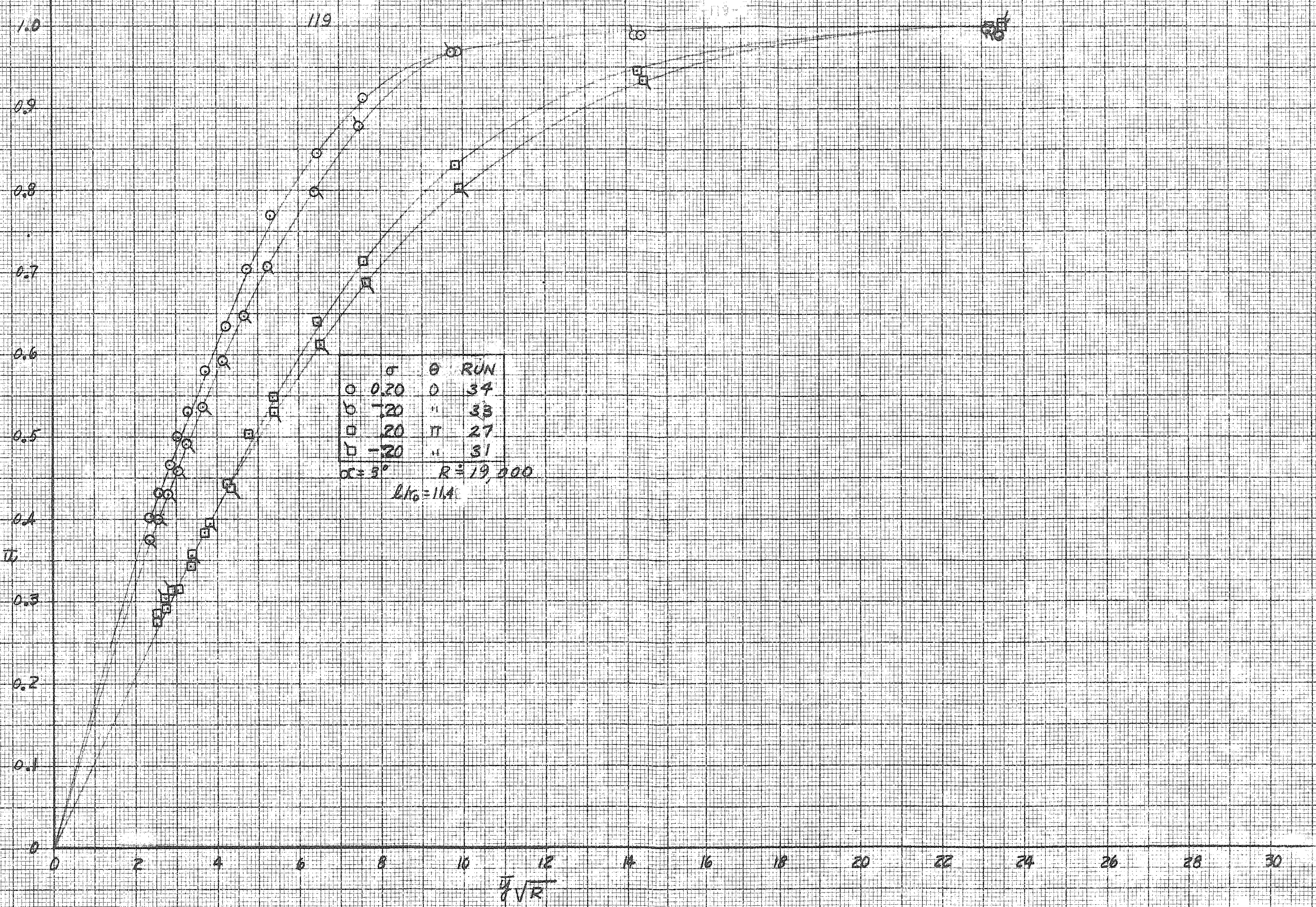

FIGURE D27

FIGURE D27

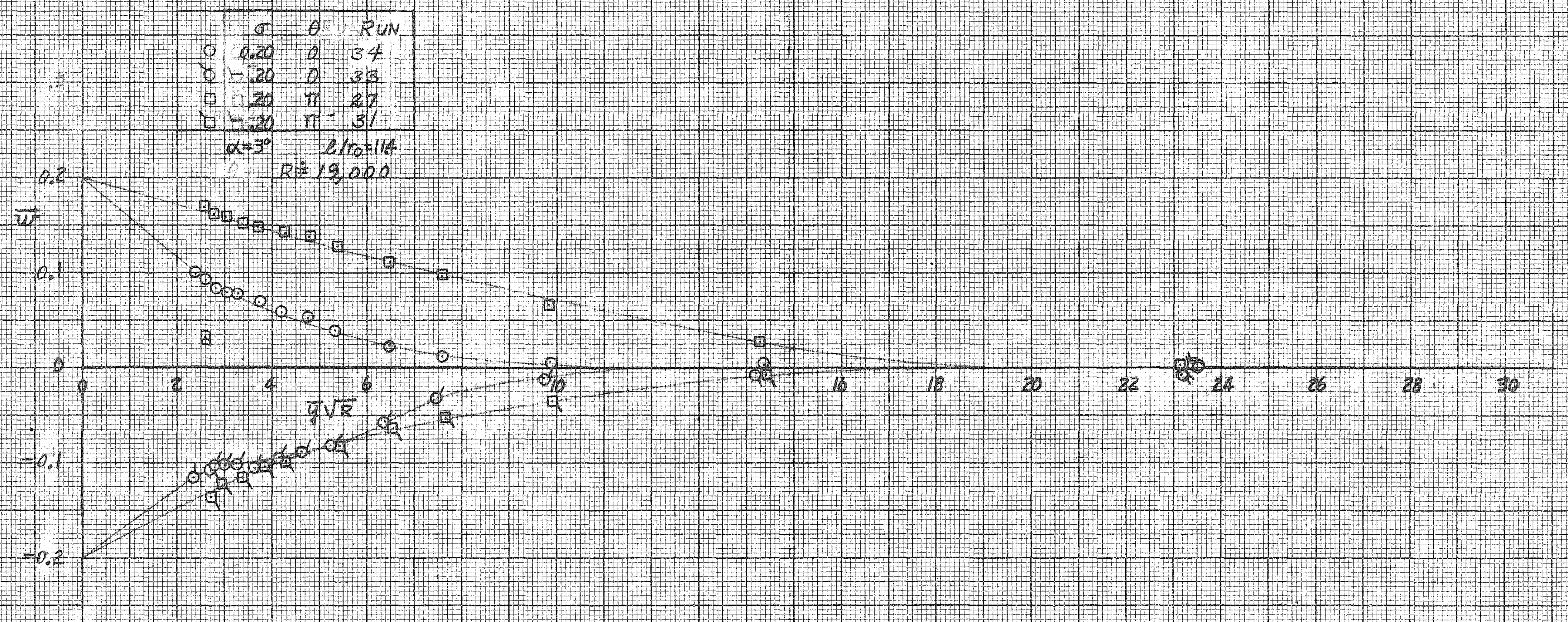
σ θ RUN
○ 0.20 0 34
.20 0 33
□ .20 π 27
.20 π 31
α=3° ℓ/r₀=114
R≑19,000
0.2
w̄
0.1
0
-0.1
-0.2
0
2
4
6
10
16
18
20
22
24
26
28
30
ȳ√R
FIGURE D28

FIGURE D28

APPENDIX E

SCHEDULE OF RUNS

Run	Date	α	ℓ/r_o	θ	σ	R
Hot Wire Measurements with Perpendicular Probe:						
a	3 Aug. 1955	0	11.4	$3\pi/2$	0	8,800
b	3 Aug. 1955	0	11.4	$3\pi/2$	0.21	8,700
c	5 Oct. 1955	3^o	11.4	$3\pi/2$	0	8,800
d	6 Oct. 1955	3^o	11.4	$3\pi/2$	0.22	8,600
Pressure Probe Measurements:						
1	28 Mar. 1956	0	11.4	$3\pi/2$	0	17,900
2	29 Mar. 1956	0	11.4	$3\pi/2$	0	9,030
3	29 Mar. 1956	0	11.4	$3\pi/2$	0	25,200
Hot Wire Measurements with Swept Back Probe:						
4	25 Apr. 1956	0	11.4	$3\pi/2$	0	18,450
5	3 May 1956	0	11.4	$3\pi/2$	0	9,050
6	3 May 1956	0	11.4	$3\pi/2$	.43	9,220
7	14 May 1956	0	11.4	$3\pi/2$	0	8,820
8	15 May 1956	0	11.4	$3\pi/2$	.44	8,830
9	15 May 1956	0	11.4	$3\pi/2$	.21	9,130
10	15 May 1956	0	11.4	$3\pi/2$	.63	8,930
11	15 May 1956	0	11.4	$3\pi/2$	-.44	8,540
12	16 May 1956	0	11.4	$3\pi/2$	0	18,160
13	16 May 1956	0	11.4	$3\pi/2$	-.22	17,640
14	16 May 1956	0	11.4	$3\pi/2$	.22	17,660
15	16 May 1956	0	11.4	$3\pi/2$	.11	17,390
16	16 May 1956	0	11.4	$3\pi/2$	.33	17,040
17	16 May 1956	0	11.4	$3\pi/2$	0	33,260
18	17 May 1956	0	11.4	π	0	18,070
19	17 May 1956	0	11.4	π	.21	17,810

APPENDIX E

SCHEDULE OF RUNS (Cont'd)

Run	Date	α	ℓ/r_o	θ	σ	R
20	17 May 1956	0	11.4	0	0	17,630
21	17 May 1956	0	11.4	0	.22	17,400
22	10 July 1956	0	11.4	π	0	18,570
23	10 July 1956	0	11.4	π	0	18,480
24	10 July 1956	3^o	11.4	π	0	18,700
25	10 July 1956	3^o	11.4	π	0	9,060
26	10 July 1956	3^o	11.4	π	.10	19,120
27	17 July 1956	3^o	11.4	π	.20	18,720
28	17 July 1956	3^o	11.4	π	.05	18,770
29	18 July 1956	3^o	11.4	π	.20	9,500
30	18 July 1956	3^o	11.4	π	.33	18,800
31	19 July 1956	3^o	11.4	π	-.20	19,080
32	19 July 1956	3^o	11.4	0	0	18,970
33	19 July 1956	3^o	11.4	0	-.20	18,800
34	21 July 1956	3^o	11.4	0	.20	19,280
35	23 July 1956	3^o	11.4	0	.05	19,360
36	23 July 1956	3^o	11.4	0	.10	19,120
37	23 July 1956	3^o	11.4	0	.33	19,200
38	23 July 1956	3^o	11.4	0	0	9,760
39	23 July 1956	3^o	11.4	0	.19	9,760
40	25 July 1956	3^o	11.4	0	.38	9,995
41	25 July 1956	3^o	11.4	0	.09	9,810
42	26 July 1956	3^o	11.4	$3\pi/2$	.10	9,890
43	26 July 1956	3^o	11.4	$3\pi/2$	-.10	9,790
44	26 July 1956	3^o	11.4	$3\pi/2$	-.19	9,760
45	26 July 1956	3^o	11.4	$3\pi/2$	.19	9,760
46	27 July 1956	3^o	11.4	$3\pi/2$	0	10,060
47	27 July 1956	3^o	11.4	$3\pi/2$	0	19,280
48	27 July 1956	3^o	11.4	$3\pi/2$	.38	9,900

APPENDIX E

SCHEDULE OF RUNS (Cont'd)

Run	Date	α	ℓ/r_o	θ	σ	R
49	27 July 1956	3^o	11.4	$3\pi/2$	-.38	9,850
50	27 July 1956	3^o	11.4	$3\pi/2$	-.05	19,000
51	27 July 1956	3^o	11.4	$3\pi/2$	.05	19,000
52	17 Aug. 1956	3^o	11.4	π	.10	9,170
53	17 Aug. 1956	3^o	11.4	π	.42	9,170

*See note at bottom of page.

Run	Date	α	ℓ/r_o	θ	σ	R
54	23 Aug. 1956	3^o	11.4	$3\pi/2$	0	9,400
55	23 Aug. 1956	3^o	11.4	$3\pi/2$	.61	9,100
56	23 Aug. 1956	3^o	11.4	$3\pi/2$	-.61	8,990
57	24 Aug. 1956	3^o	11.4	$5\pi/4$	0	8,690
58	24 Aug. 1956	3^o	11.4	$5\pi/4$	.11	8,580
59	24 Aug. 1956	3^o	11.4	$5\pi/4$	.21	9,100
60	26 Aug. 1956	3^o	11.4	$5\pi/4$	.42	9,100
61	27 Aug. 1956	3^o	11.4	$3\pi/4$	0	8,990
62	27 Aug. 1956	3^o	11.4	$3\pi/4$	.43	8,890
63	27 Aug. 1956	3^o	11.4	$3\pi/4$	.20	9,500
64	27 Aug. 1956	3^o	11.4	$3\pi/4$	.10	8,990
65	28 Aug. 1956	3^o	11.4	$\pi/4$	0	9,100
66	28 Aug. 1956	3^o	11.4	$\pi/4$	.22	8,990
67	28 Aug. 1956	3^o	11.4	$\pi/4$	.11	8,790
68	28 Aug. 1956	3^o	11.4	$\pi/4$	.44	8,790
69	29 Aug. 1956	3^o	11.4	$7\pi/4$	0	8,890
70	29 Aug. 1956	3^o	11.4	$7\pi/4$	.11	8,790
71	29 Aug. 1956	3^o	11.4	$7\pi/4$	.22	9,100
72	29 Aug. 1956	3^o	11.4	$7\pi/4$	.43	8,890

*Note: First hot wire on swept-back probe was used for runs 4 through 53. Second hot wire on swept-back probe was used for runs 54 through 87.

APPENDIX E

SCHEDULE OF RUNS (Cont'd)

Run	Date	α	ℓ/r_o	θ	σ	R
73	30 Aug. 1956	0	11.4	$3\pi/2$	0	9,400
74	30 Aug. 1956	0	11.4	$3\pi/2$	.10	9,400
75	30 Aug. 1956	0	11.4	$3\pi/2$	.62	9,300
76	30 Aug. 1956	0	11.4	$3\pi/2$	-.62	9,200
77	30 Aug. 1956	0	11.4	$3\pi/2$	0	18,700
78	30 Aug. 1956	0	11.4	$3\pi/2$	.05	18,500
79	31 Aug. 1956	0	10.2	$3\pi/2$	0	9,500
80	31 Aug. 1956	0	10.2	$3\pi/2$	.61	9,400
81	31 Aug. 1956	0	10.2	$3\pi/2$	.20	9,500
82	31 Aug. 1956	0	10.2	$3\pi/2$	-.20	9,400
83	3 Sept. 1956	3^o	10.2	$3\pi/2$	0	9,200
84	4 Sept. 1956	3^o	10.2	$3\pi/2$	-.21	9,200
85	4 Sept. 1956	3^o	10.2	$3\pi/2$	.21	9,200
86	4 Sept. 1956	3^o	10.2	$3\pi/2$	.63	9,100
87	4 Sept. 1956	3^o	10.2	$3\pi/2$	-.63	9,100

Note: During each run (for a given spin rate) the rotation of the model was held constant within ± 0.1 rev./sec.